Computational Design and Evaluation of New Materials for Energy and Environmental Applications

by

Abhishek Bagusetty

Master of Science in Chemical Engineering, University of Utah,
2015
Bachelors of Technology in Chemical Engineering, Shanmugha
Arts, Science, Technology and Research Academy, 2012

Submitted to the Graduate Faculty of
the Swanson School of Engineering in partial fulfillment
of the requirements for the degree of

Doctor of Philosophy

University of Pittsburgh

2019

UNIVERSITY OF PITTSBURGH

SWANSON SCHOOL OF ENGINEERING

This dissertation was presented

by

Abhishek Bagusetty

It was defended on

November 18, 2019

and approved by

J. Karl Johnson, Ph.D., William Kepler Whiteford Professor, Department of Chemical and Petroleum Engineering

Kenneth D. Jordan, Ph.D., Richard King Mellon Professor and Distinguished Professor of Computational Chemistry, Department of Chemistry

Giannis Mpourmpakis, Ph.D., Associate Professor, Department of Chemical and Petroleum Engineering

Sachin Velankar, Ph.D., Associate Professor, Department of Chemical and Petroleum Engineering

Dissertation Director: J. Karl Johnson, Ph.D., William Kepler Whiteford Professor, Department of Chemical and Petroleum Engineering

Computational Design and Evaluation of New Materials for Energy and Environmental Applications

Abhishek Bagusetty, PhD

University of Pittsburgh, 2019

With a constant demand for efficient energy devices, significant efforts were invested into the development of proton exchange membrane (PEM) fuel cells. Yet, water management and hydration in these PEM fuel cells are a well-known limiting factors for proton transport. The first-principles density functional theory (DFT) study helped to develop two novel 2-D materials that can potentially alleviate the need for aqueous conditions to propagate proton conduction within fuel cells. Anhydrous proton conduction can be achieved when graphane is functionalized with hydroxyl and amine groups as graphamine and graphanol, respectively. Ab-initio molecular dynamics simulations indicated that the proton transport is facile with a relatively low reaction barrier due to the presence of a self-assembling network of hydrogen bonds established over the surface of these materials. Moreover, proton self-diffusivity increases with temperature and thermodynamic stability calculations indicate that these materials are appropriate for intermediate-temperature fuel cells.

Given the environmental concerns of tritiated water (HTO), this work is an attempt to understand the fundamental nature of differential hydrogen bonding offered by the hydrogen isotopes. When two phases (liquid and vapor) of water are in equilibrium, there can be slight difference in the relative abundance of water isotopes for each phase. The treatment of nuclei under classical mechanics is not appropriate for the study of lighter atoms like hydrogen and its isotopes. By employing path-integral-based molecular simulations one can account for quantum motion of the nuclei to determine isotopic fractionation ratios for water isotopologues in phase equilibrium and cocrystallization of water isotopologues with poly-oxacyclobutane. Due to the inherent computationally intensive nature of these calculations, a combination of reduced-cost and accelerated techniques such as high-order splitting and thermostating procedures were used to achieve convergence of quantum mechanical properties.

Table of Contents

List of Tables

List of Figures

1.0 Introduction

This dissertation encompasses two main research thrusts, each directed towards designing new materials for energy and environmental applications from a computational and theoretical approach. The first thrust is towards the design of materials that conduct protons along an interface with very high efficiency in the complete absence of water for an intermediate temperature fuel cells. The second thrust focuses on exploring nuclear quantum effects associated with liquid-vapour fractionation ratio for water isotopologues namely, deuterated water (HDO) and tritiated water (HTO).

1.1 Anhydrous Proton Transport on a Functionalized Surface

Proton exchange membranes are one of the most critical components of PEM fuel cells.[1, 2, 3, 4] Nafion, a perfluorinated sulfonic acid ionomer, is considered to be a reference standard for proton conducting membrane materials because of its favorable chemical, mechanical, and thermal stability, together with its high proton conductivity when sufficiently hydrated.[5] However, Nafion has several disadvantages, including high cost and low upper operating temperature (<80°C). Increasing the operating temperature of PEM fuel cells would have several benefits, including increased electrochemical reaction rates, the availability of higher quality waste heat, and decreased carbon monoxide poisoning of the anode.[6, 7] Hence, there is a critical need for development of anhydrous proton transport membranes in order to increase the operating temperature of fuel cells. The overarching hypothesis of this work is that a facile anhydrous proton transport will occur on a surface that has a continuous network of hydrogen bonded functional groups. Furthermore, we hypothesize that functionalization of graphane with hydroxyl and amine groups are prime examples of materials that can conduct protons at high rates in the complete absence of water. First principles density functional theory (DFT) calculations on few model systems were conducted as a proof-of-concept test of our hypothesis and to obtain insights.

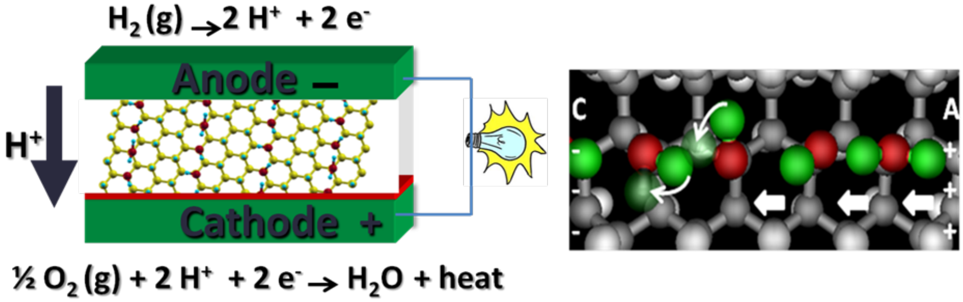

Figure 1: A schematic of an idealized OH-functionalized graphane proton exchange membrane (left) and a schematic representation of how proton transport takes place (right). In practice, the membrane would consist of many stacks or layers of functionalized graphane to achieve high proton flux.

The practical engineering motivation for this work is to improve performance and reduce costs of hydrogen fuel cells through developing insights that can be applied to designing the next generation of proton exchange membrane materials. Fuel cells offer the promise of providing energy under a variety of conditions at very high efficiency. Hydrogen fuel cells directly convert the free energy from the chemical reaction between H_2 and O_2 into electricity, producing only water and heat as the byproducts. A proton exchange membrane (PEM) fuel cell uses H_2 at the anode to produce protons (H^+) and electrons. The protons traverse a PEM to arrive at the cathode, where they combine with oxygen and the electrons, which flow through an external electrical circuit, to form H_2O. This work is driven by two overarching hypotheses: (1) surfaces having a contiguous network of hydrogen bonded functional groups will be able to conduct protons in the complete absence of water and (2) computational modeling can be used to design, test and optimize new materials that have facile proton transport (PT) under anhydrous conditions.

We predict that graphane functionalized with hydroxyl groups, hydroxygraphane, can conduct protons in the complete absence of water, as shown from density functional theory calculations. Hydroxygraphane's proton conductivity results from the self-assembling two-dimensional network of hydrogen bonds on its surface. We show that the proton conduction occurs through a Grotthuss-like mechanism, as protons hop between neighboring hydroxyl groups, aided by their rotation. We also report that graphane functionalized with amine groups (graphamine) can conduct protons in the complete absence of water. Our calculations show that graphamine is an electronic insulator having a direct band gap of 3.08 eV. The following chapters discusses the transport, electronic, and structural properties required for a viable anhydrous proton conduction membrane material.

1.2 Isotope Fractionation Ratio

This dissertation also covers an extensive study of understanding nuclear quantum effects associated with the water isotopologues in Chapter.5. These effects were known to lower the melting point of H_2O by atleast 8 K in comparison to water studied with classical description. In this work, the fundamental quantum nature of isotope effects in water isotopologues were discussed to determine the liquid vapor isotope fractionation ratio and also employing similar principles towards a technologically driven application leading to the separation of diluted heavier water isotopologue - tritiated water (HTO) from light water (H_2O) and molecular isotopes of oxygen. Tritium with a half-life of 12.36 years is characterized by beta decay with an 18.6 keV maximum energy. This has been considered one of the most innocuous of fission produced radionuclides. The low energy and penetration power of the tritium isotope particle associated with its decay does not pose a significant external radiation hazard. However, tritiated water and its vapor posses a potential health hazard for humans from skin and other modes of penetration. The retention of tritium in the body is dependent on the chemical form it enters the body. Traditionally the HTO is either stored in drums for 10 times its half life (120 years) or it is dispersed into the local environment, hopefully in small enough quantities to create a minimum impact on the local ecology. However, it is believed by many that any amount of tritiated water is detrimental to living organisms. Several technologies such as membrane separation, electrolysis, freezing, ion-exchange methods have earlier been reported in the literature but these methods are expensive and inefficient. A membrane method exists for separating HTO from light water where the mixture is placed under pressured and forced through a polyphosphazene polymer based membrane.[8] This method has the disadvantage of being expensive and complicated (and therefore slow). The purpose of this work is to identify an inexpensive polymeric material that can facilitate a separation of HTO from regular water under the conditions of membrane separation. We have carried out path integral molecular dynamics simulations on a given polymeric material as a proof-of-concept to test and verify our approaches and assumptions. This work also illustrates the nuclear quantum effects of hydrogen bonds established by water isotopologues (HTO, H_2O) with a given candidate polymeric material to bind the heavy isotopologue HTO strongly over the light H_2O water. A separation can be feasible if these heavier water isotopologues are selectively incorporated as water of hydration within a crystalline polymeric material.(Chapter.6) Owing to the differences in the strength of hydrogen bonding, a seperation could be feasible. By employing these nuclear quantum effects, we have also investigated the separation of heavier molecular oxygen isotope ($^{18}O_2$) from naturally abundant $^{16}O_2$ using single walled carbon nanotubes.

2.0 Facile Anhydrous Proton Transport on Hydroxyl Functionalized Graphane

This work was published as: Bagusetty, A., Choudhury, P., Saidi, W. A., Derksen, B., Gatto, E., & Johnson, J. K. (2017). Facile anhydrous proton transport on hydroxyl functionalized graphane. *Phys. Rev. Lett., 118(18), 186101.*

2.1 Introduction

Transport of protons through membranes is of vital importance across a broad range of processes, ranging from biological systems to industrially-important technologies. We here report the first principles design of a novel material capable of facile conduction of protons in the complete absence of water, which addresses a critical challenge related to proton exchange membrane (PEM) fuel cells.[4] The most widely used PEM materials are polyelectrolyte polymers, such as Nafion.[9] These polymers conduct protons at appreciable rates only when hydrated. As a result, the upper limit for the operating temperature of PEM fuel cells is typically about 80°C because higher temperatures result in dehydration of the polyelectrolyte polymer [10], which causes a dramatic decrease in the rate of proton conduction. We show that functionalized graphane can conduct protons anhydrously at elevated temperatures, making it a potential material for intermediate temperature PEM fuel cells. There are several advantages to operating PEM fuel cells at intermediate temperatures (100–200°C), including increased electrochemical reaction rates, the availability of higher quality waste heat, and decreased CO poisoning of the anode.[7] Hence, there is a practical need for anhydrous proton transport (PT) membrane materials that has motivated research in this area.[6]

A key requirement for a material to exhibit fast PT is optimal donor-acceptor spacing. Thus, facile anhydrous PT should occur on a surface having a fixed contiguous network of hydrogen bonded hydroxyl (OH) groups. Accordingly, we have used density functional theory (DFT) calculations to show that graphane (fully hydrogenated graphene) functionalized with hydroxyl groups has inherent near-optimal spacing for forming a surface network of hydrogen bonds capable of facilitating fast anhydrous PT. We show that this novel material offers both the opportunity for fundamental studies of anhydrous PT and the potential for creating new practical PEM membrane materials. The mechanism of PT in aqueous systems has been extensively studied and is well understood. In contrast, the PT mechanisms under anhydrous conditions appear to depend on the material and are a matter of debate.[6, 11, 12, 13] This work provides atomic-level insight into how PT takes place on OH-functionalized graphane and why the barriers to PT on this material are so low.

2.1.1 Why Graphane?

There are at least two advantages for use of graphane instead of graphene as the platform for constructing PT membranes: (1) proton exchange membranes must be electronic insulators and graphene is a semimetal, whereas hydroxylated graphane is an insulator with a direct band gap of 3.22 eV [14]; (2) graphane has sp^3 structure, whereas functionalized graphene has both sp^2 and local sp^3 structures, resulting in more strain compared with functionalized graphane. In addition, hydroxylated graphane is predicted to be stable.[14] Our model system is shown in Fig. 2 and consists of a periodic supercell of graphane having a one-dimensional (1-D) chain of OH groups spanning the cell. This system contains 4 OH groups and a single proton; the system has a +1e total charge. The hydroxyl groups can rotate about the C–O bonds and our relaxed structures show that these OH groups spontaneously orient to form a 1-D chain of hydrogen bonds as a result of the inherent structure of graphane, i.e., the natural distance of OH groups on graphane is nearly ideal for hydrogen bonding, with O–O distances of about 2.3 to 2.4 Å.

2.2 Calculation Method

We carried out DFT calculations using the Vienna *Ab-initio* Simulation Package (VASP) [15] and an in-house modified version of Quantum Espresso (QE) [16]. An energy cutoff of

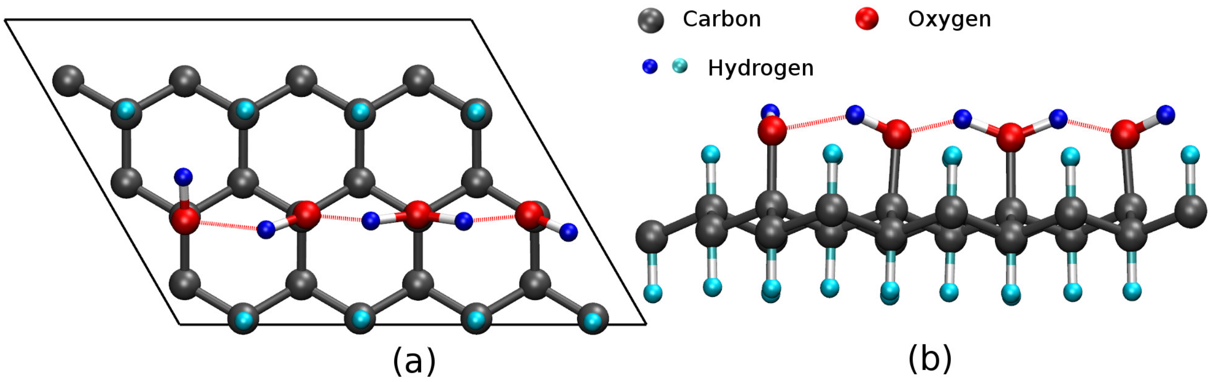

Figure 2: (a) Top view, Hydroxylated graphane supercell containing 24 carbons and 4 hydroxyl groups with one excess proton (carbons in gray, oxygens in red, hydrogens bound to oxygens in dark blue, hydrogens bound to carbon in light blue, red lines indicate hydrogen bonding). (b) Side-on view for the configuration in (a). Supercell lattice parameters are given in Table 2 of the Appendix A.4. Solid lines show the cell boundaries in the a and b directions.

520 eV was used with the Perdew-Burke-Ernzerhof form of the generalized gradient approximation [17]. We checked the convergence of the k-point grid and vacuum spacing to validate our computational setup. The minimum energy pathway (MEP) for PT was obtained using the climbing image nudged elastic band (cNEB) method.[18] The size of the supercell in the direction perpendicular to the graphane plane was 20 Å, insuring interactions between the layers were negligible. Proton diffusivities were computed from Born-Oppenheimer *ab-initio* molecular dynamics (AIMD) simulations in the NVE (microcanonical) ensemble with a step size of 0.25 fs. Details are given in Appendix A.1.

2.3 Proton Transport Dynamics

The self-diffusion coefficients, D, at different temperatures are plotted in Fig. 3. Extrapolation of the data gives an estimate of D at room temperature of 4×10^{-5} cm^{2}s^{-1}, which is

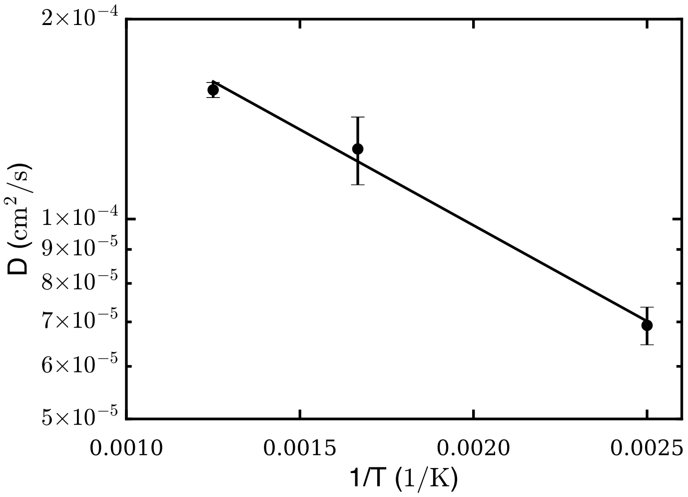

Figure 3: Self-diffusion coefficients at temperatures of 400, 600, and 800 K as determined from AIMD simulations.

fortuitously close to the self-diffusion coefficient of protons through bulk water computed from molecular simulations.[19] Diffusion coefficients of protons through Nafion depend dramatically on the hydration level. Simulations predict that diffusivity increases from 1.4×10^{-6} to 1.7×10^{-5} cm^{2}s^{-1} at room temperature as the number of water molecules increases from 6 to 15 per sulfonic acid group.[20] These simulations are in good agreement with experimental measurements for Nafion under similar conditions.[21] Our data were fitted to an Arrhenius expression, which yielded an activation energy of 60 meV. This is significantly lower than the experimentally measured activation energy for proton conductance in Nafion, which ranges from 0.1 to 0.36 eV, depending on water content [22]. Analysis of the AIMD simulations indicated that proton hopping takes place in concert with the rotation of hydroxyl groups and this rotation is expected to be the rate limiting step in PT.

2.4 Proton Transport Energetics

The rate limiting step was confirmed by computing the MEP for PT from the cNEB method. Our calculated barrier height for proton hopping along the OH chain is about 70 meV, as shown in Fig. 4. This barrier height is in very good agreement with the activation energy of 60 meV estimated from AIMD diffusivity calculations. We note that exact agreement is not expected between barrier heights from cNEB and apparent activation energies from Arrhenius plots for several reasons: (1) the barrier heights from cNEB calculations are zero Kelvin electronic energies while activation energies are temperature-averaged Gibbs free energies, (2) the AIMD calculations include anharmonic effects that are not captured in the cNEB calculations, and (3) the diffusivities are subject to statistical errors. The very low barrier computed from cNEB (Fig. 4) provides a second confirmation (with the AIMD results) of our expectation that hydroxylated graphane will conduct protons at fast rates under anhydrous conditions. As we tentatively observed in the AIMD simulations, cNEB confirms that the PT pathway consists of a concerted hopping mechanism involving rotation of hydroxyl groups about the C–O bond axis, along with the displacement of a proton. Key configurations from the MEP are shown in Fig. 5. We note an unexpected feature in the MEP that is elucidated by examining the configurations in Fig. 5: the MEP has two transition states, separated by a very shallow local minimum metastable state. The two end-point geometries, (a) and (e) in Fig. 5, are identical by translational symmetry and are characterized by a single OH bond pointing perpendicular to the 1-D chain of OH groups, with the H atom pointing to the center of a hexagon in the underlying graphane. The metastable intermediate, Fig. 5 (c), is similar in structure, except that the OH group perpendicular to the chain is oriented over a graphane C–C bond. The two transition states are almost isoenergetic (Fig. 4) and are visually identical, as seen in Fig. 5 (b) and (d). The transition states correspond to an OH group just before and just after the C–C bond center crossing. We also note two distinct proton hopping events in Fig. 5, as defined by a change in the nearest O for a given H. We have ignored quantum diffraction effects in our calculations. Zero-point energy corrections obtained from vibrational frequency calculations reduce the classical barrier height from 70 to 40 meV. We have estimated rate constants for PT using three different transition state theory (TST) approximations. Rate constants were determined using classical and quasi-classical treatment of TST [23], and tunneling effects were estimated using the semi-classical TST approximation.[24] Results from these calculations are shown in Fig. 20 of the Appendix A.3. Tunneling effects were found to be negligible for the temperatures considered here. This is not unexpected because the proton hopping barrier is both small and broad (Fig. 4). On the other hand, quantum effects estimated from zero-point energy corrections through the quasi-classical TST approximation increase the rate constant by about a factor of 1.7 near room temperature. Therefore, our classical treatment can be viewed as a lower bound estimate to the diffusivity.

Interestingly, although there is formally only one proton in the system, each of the H atoms involved in hydrogen bonding behave essentially as protons, i.e., each H atom bound to an O atom can potentially hop. Moreover, the effective charges on the H atoms, as computed from the DDEC6 population analysis method [25], are almost identical (Table. 3, Appendix A.6.3). Thus, the H atoms are, in a sense, indistinguishable, and the proton is highly delocalized. The charge delocalization is an unexpected feature and so we have verified that this is not an artifact due to system size effects by using a larger super cell; we also eliminated the possibility that the charge delocalization was due to self-interaction error by computing charges from Hartree-Fock level of theory (see Table 4 & 5 of Appendix A.6.3). Charge delocalization decreases the barrier to PT by reducing the polarization associated with moving a proton from one O atom to another.

We have estimated finite-size effects in our calculations by constructing a supercell consisting of 70 C atoms, 7 OH groups, and a single proton. Note that this system has different symmetry than the 4 OH system because of the odd number of OH groups in the unit cell. We have computed the cNEB MEP in this 7 OH system and plotted the results in Fig. 4. The MEP for the larger system has the same features as the smaller system and a barrier that is about 12 meV higher. The one qualitative difference between the two systems is that the 7 OH system has only a single proton hop (see Fig. 21 of Appendix A.4). This difference can be attributed to finite-size effects because rotation of an OH group in the smaller system has a larger influence due to periodic boundary conditions.

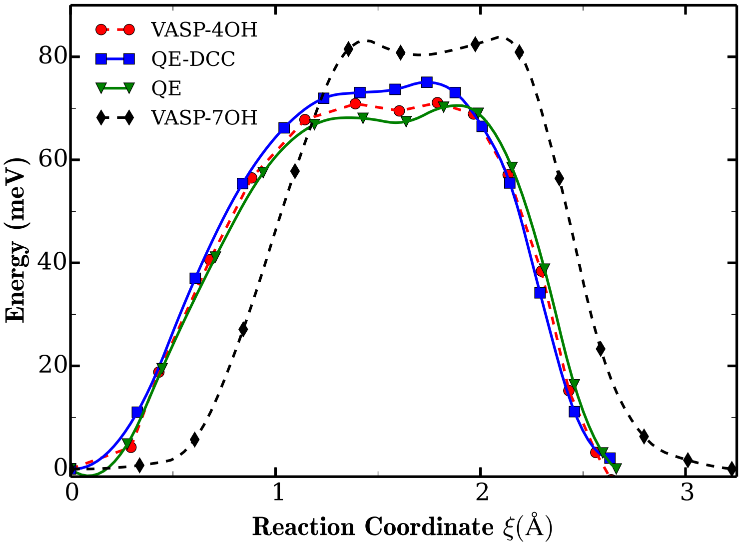

Figure 4: Minimum energy pathway (MEP) computed from the cNEB method for proton hopping on a 4-OH group system (see Fig. 2) computed from VASP (red circles) and Quantum Espresso (QE) without (green triangles) and with (blue squares) density-countercharge corrections. The MEP for a 7-OH group system is also shown (black diamonds) as a test of finite system size effects.

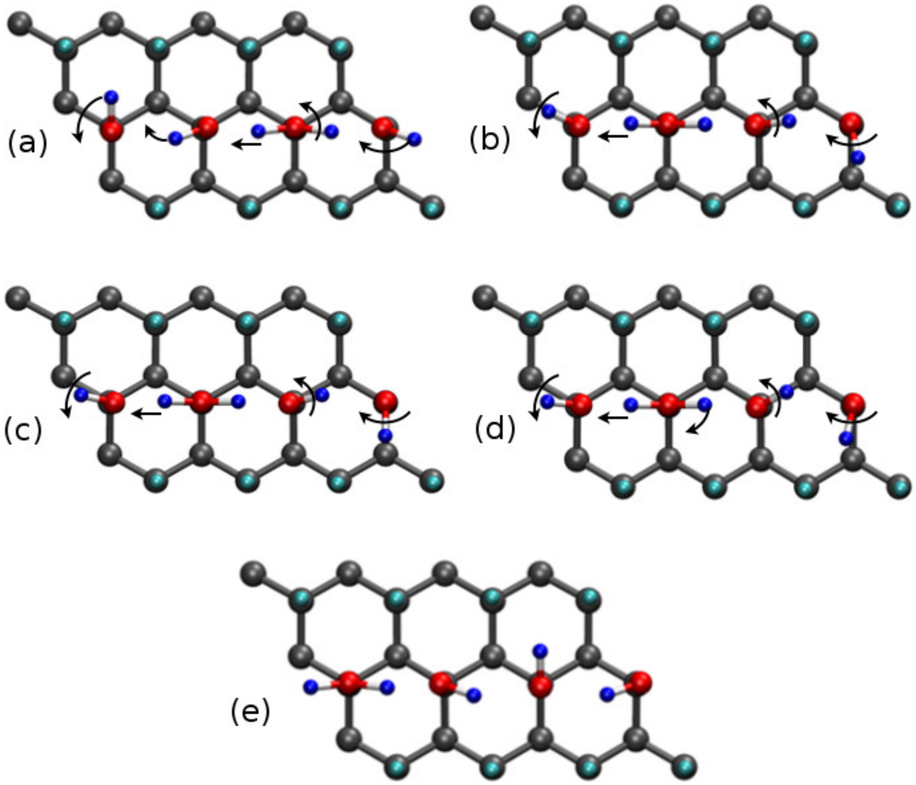

Figure 5: Atomic configurations computed from cNEB for the 4-OH group system (Fig. 2) for the (a) initial, (b) first transition state, (c) metastable intermediate, (d) second transition state and (e) final state. The concerted motion in each step is indicated with arrows (colors defined in Fig. 2).

2.4.1 Challenges in Charged Systems

Periodic DFT calculations of charged systems are problematic because of errors due to imposing an artificial jellium background.[26] We have estimated the extent of this error by implementing the density-countercharge (DCC) method of Dabo et al.[27] in an in-house modified version of QE. We computed the cNEB pathways for the 4 OH system using both the original QE code (no DCC) and the DCC corrected code. These MEPs are plotted in Fig. 4. Adding the DCC corrections increases the barrier by about 5 meV, indicating that the errors introduced due to the jellium background are very small. We also note that the 7 OH system provides an independent check of the error due to the charge because the system is larger but has the same net charge. However, in this case, the difference between the two systems includes other effects due to flexibility and periodicity, in addition to the charge density.

2.4.2 Transport Mechanism Details

One might assume that PT in the 1-D systems studied here would result in single-file mobility because the protons cannot pass one another. Single-file mobility is characterized by the mean square displacement (MSD) of protons being proportional to $t^{1/2}$, where t is time.[28] However, we found that this system follows the Einstein relation for Fickian diffusion (MSD $\propto t$) [28], as seen in Fig. 23 of the Appendix A.5. We constructed a lattice model to test whether the Fickian diffusion observed from AIMD simulations was due to artifacts of system size or short simulation times. The results of the lattice model also show Fickian diffusion (see Fig. 23). The system with a single proton effectively behaves as being in the infinite dilution limit even though all of the hydrogens on OH groups can hop. This unexpected outcome can be rationalized by considering the case without a proton. In this case, one has a contiguous chain of hydrogen bonded OH groups, but no protons and therefore no PT can take place. Thus, the 1-D system is analogous to a 1-D lattice model, where the OH chain without a proton is like an empty lattice, the chain with a single proton is similar to a lattice with one occupied site, but having the unique feature that any of the H atoms on the chain can hop. Simulations of a lattice model with 8000 OH groups and 4000 protons show that this “half-filled” system exhibits the expected single-file mobility, with the MSD $\propto t^{1/2}$ (see Fig. 24, Appendix A.5. Note that system size effects can give rise to anomalously large diffusivities for diffusion of fluids through very smooth nanopores.[29, 30] The hallmarks of this system size artifact are: (1) calculated diffusion barriers that are inconsistently large compared with measured diffusivities and (2) systematic deviations from MSD $\propto t$.[29] Our system does not display anomalous diffusivities because the calculated diffusion barrier from cNEB is consistent with the barrier computed from AIMD (Figs. 3 and 4) and we clearly observe MSD $\propto t$ (Fig. 23).

2.5 Conclusions

Several observations can be made based on our results. Firstly, the PT mechanism identified here is significantly different from mechanisms in bulk water and 1-D water wires. It has been shown that concerted PT through a Grotthuss mechanism [31] in both bulk water and water wires confined to 1-D channels, such as carbon nanotubes [32], results in unfavorable polarization of the water chain, the resolution of which requires significant solvent reorganization.[33, 13] Hydroxylated graphane has no hydrogen bonding defects like orientational D or L configurations as reported for PT in carbon nanotubes [33, 34], and hence there is no need for solvent reorganization. The only reorganization required is local in nature–involving the concerted rotation of a pair of adjacent OH groups. Moreover, since this system is anhydrous there is no large electrostatic penalty for desolvation, and the conductance of protons should not decrease with length of the 1-D path, as with narrow carbon nanotubes.[32]

A second observation is that hydroxylated graphane is potentially a significantly better material for anhydrous proton exchange membranes than existing materials. Proton conduction on OH functionalized polymers [6, 35], ionic crystals [36], and doped amorphous carbons [37] has been demonstrated, but none of these materials have optimal placement of hydrogen bonding groups. Hence, they lack the contiguous network of hydrogen bonds required for truly facile water-free PT. As noted by Nagamani et al., the presence of a hydrogen bond network is vital to fast and robust PT [35]. Another advantage of a functionalized surface over polymers is the reduced flexibility of the surface relative to a polymer; flexibility in the polymer chain disrupts hydrogen bonds and decreases the PT rate.

It is interesting to note the similarities between the contiguous 1-D OH chain of Fig. 5 and the hypothetical soliton system studied previously.[38] Although the charge is highly delocalized, our system does not exhibit soliton-like collective PT. This is because proton transport coupled with rotation of an OH group is inconsistent with the soliton mechanism.[38]

Hydroxylated graphane could potentially be produced by using electron-beam generated plasmas, which have been used to functionalize graphene with F, H, and O atoms.[39] This approach would produce a high degree of hydroxylation, rather than a 1-D chain of OH groups, but having a 2-D network of hydrogen bonds will provide redundant pathways for PT and thus be more robust than the 1-D system we have studied here. A single missing OH group in a 1-D chain effectively blocks PT (the estimated barrier is about 4.4 eV, see Fig. 28 and the discussion in the Appendix A.7 so for any practical material, a 2-D network is desired. We are currently investigating the characteristics of PT in a 2-D network.

3.0 Unraveling Anhydrous Proton Conduction in Hydroxygraphane

This work was published as: Bagusetty, A., & Johnson, J. K. (2019). Unraveling Anhydrous Proton Conduction in Hydroxygraphane. *J. Phys. Chem. Lett., 10(3), 518-523.*

3.1 Introduction

Proton conduction is of fundamental importance in fields as diverse as cell function,[40, 41] photosynthesis,[42, 43] enzyme catalysis,[44] and battery and fuel cell technologies.[45, 46, 4, 47] Proton transport in aqueous systems has been widely investigated through theoretical [48, 49] and experimental techniques [50, 49] for decades and is still an active area of research, as seen from recent intriguing findings of proton transport for water dissociation in nanoconfined channels[51, 52] and unusual proton transport characteristics at the temperature of maximum density.[53] In contrast, the study of of proton transport under anhydrous conditions has not been studied as extensively.[6]

Proton exchange membrane (PEM) fuel cells are increasingly important in applications such as fuel cell vehicles and portable power generation.[54] Limitations of current PEM fuel cells include the requirement that the operating temperature not exceed about 80°C and that the membrane be sufficiently hydrated. Both of these requirements are the result of materials property limitations of the polymer electrolyte membrane, Nafion,[5] used in the current generation of fuel cells. The fundamental issue is that Nafion is not an intrinsic proton conduction material—it is only capable of conducting protons when sufficiently hydrated. There are significant advantages to increasing the operating temperature of PEM fuel cells and eliminating the need for membrane humidification, including increased kinetic rates, the availability of higher quality waste heat, higher resistance to electrode poisoning, and simplified water management.[7, 55, 6] Hence, there is a need to develop new materials that facilitate proton transport under anhydrous or low humidity conditions.[56, 57]

Recent work has focused on the discovery and synthesis of new materials capable of proton conduction under low-humidity or anhydrous conditions.[58, 59, 60, 61, 62, 63, 64, 65] Porous metal organic frameworks and related materials have been proposed as Nafion replacements.[66, 67, 68, 59, 69, 63, 62, 70, 57] However, most of these materials have conductivities that are lower than Nafion or require water to be bound to the porous structure to facilitate proton conduction.[63] Even materials that have high intrinsic proton conductivity have high resistance to conduction across grain boundaries and could suffer from stability issues. Hence, there is still a need to both understand proton conduction under anhydrous conditions and to develop materials that have higher conductivity and stability than those now available.

In this letter we show that graphane (an sp^3 hydrogenated version of graphene [71]) that is functionalized with hydroxyl groups, which is known as graphanol or hydroxygraphane,[72] has the potential to conduct protons via a Grotthuss-like mechanism [31] in the complete absence of water. We have used density functional theory (DFT) to study proton conduction on hydroxygraphane—a quasi two-dimensional (2-D) material constructed by replacing all the hydrogen atoms on one side of graphane with hydroxyl groups (OH),[14] as shown in Fig. 6. We note that hydroxygraphane has been reported to be thermodynamically stable, according to *ab-initio* calculations.[73] More importantly, synthesis of hydroxygraphane has been reported, based on hydroboration of graphane oxide,[72] yielding stoichiometric ratios of OH and H groups.

We note that there have been two experimental reports in the literature of proton conduction on graphene oxide (GO).[74, 75] Karim et al.[75] found that GO conducts protons on the surface when humidified. They hypothesize that protons are conducted through a hydrogen bonded network of water adsorbed on the surface. This work supports our hypothesis that a hydrogen bonded network on the surface of graphene-related materials will facilitate the conduction of protons. Cao et al.[74] demonstrated that sulfonated GO nanosheets can be used to create three-dimensional networks when integrated with Nafion to form a polymer matrix. This composite material was found to conduct protons at rates comparable with Nafion. Cao and co-workers posit that the sulfonate groups favor formation of well-connected water channels. Neither of these materials can conduct protons at low humidity because they lack a sufficient density of hydrogen bonding groups on the surface to create a contiguous network of hydrogen bonds. In related work, Bagusetty *et al.* have predicted that graphane functionalized with a 1-D chain of hydroxyl groups can conduct protons under anhydrous conditions at appreciable rates.[76] However, this hypothetical material has not been made and is probably very difficult to make. Moreover, a single defect (e.g., a single missing OH group) will completely block proton conductivity along the 1-D chain.[76] Hydroxygraphane, in contrast, has been synthesized[72] and because the OH groups form a 2-D network of contiguous hydrogen bonds across the surface,[14] it should exhibit robust proton conductivity with respect to defects such as missing OH groups or carbon atoms. Hydroxygraphane also features a key descriptor for the facile conduction of protons, namely, an ordered and consistent distance between donor and acceptor (OH) groups of the hydrogen bonds, which was reported to enhance proton diffusivity in comparison to tortuous and amorphous morphologies present in most polymer electrolyte membranes.[77, 78]

The successful synthesis of hydroxygraphane[72] suggests that it is possible to experimentally test this material for proton conduction. Before doing so, it is highly advantageous to use atomistic simulations to identify the potential for hydroxygraphane to function as a PEM material. Some of the requirements that an effective intermediate temperature PEM material must have are: (1) an ability to conduct protons at acceptably high rates over a range of temperatures, even in the absence of water; (2) electrical insulation, i.e., it must be a wide bandgap semiconductor; (3) mechanical robustness. It is the aim of this letter to evaluate *in silico* the suitability of hydroxygraphane with respect to these three criteria.

3.2 Computational Methodology

Our calculations were carried out with DFT methods as implemented in the Vienna *ab-initio* simulation package (VASP).[79, 15, 80] The structural relaxation of the supercell shown in Fig. 6 gave lattice parameters of: $a = 10.703$ Å, $b = 8.027$ Å, $c = 20.0$ Å, α=β=90°, γ=120°. Projector augmented-wave (PAW) pseudopotentials [81] were employed to describe the interactions between valence electrons and frozen cores. A kinetic energy cutoff for the

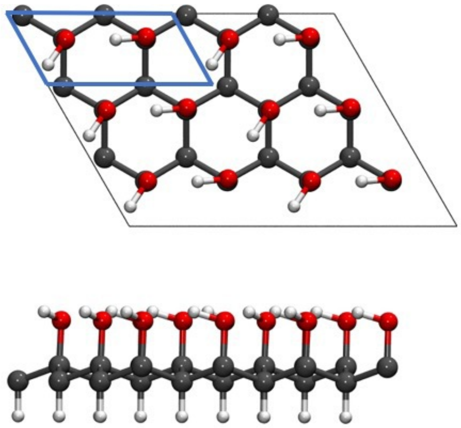

Figure 6: Top and side view of hydroxygraphane in the herringbone configuration (carbons in gray, oxygens in red, hydrogens in white). The primitive cell (containing 10 atoms) is shown by the solid blue lines. Solid black lines show the supercell which is a 3 × 2 replication of the primitive cell.

plane-wave expansion was set to 520 eV and total energy convergence for self-consistent field calculations was set to 10^{-9} eV to attain sufficient accuracy. The generalized gradient approximation exchange-correlation (XC) functional of Perdew-Burke-Ernzerhof (PBE) was used.[17, 82] The Brillouin zone sampling was performed using a Monkhorst-Pack **k**-point grid size of 7 × 7 × 1. All the ionic positions were relaxed until the forces were less than the tolerance of 10^{-3} eV/Å. A vacuum spacing of 20 Å in the direction perpendicular to the surface of hydroxygraphane was employed to mitigate the interactions between the layers under periodic boundary conditions. The calculated bond lengths for C—C, C—H, C—O were found to be 1.57 Å, 1.11 Å and 1.43 Å, respectively, for the optimized configuration in Fig. 6. These values agree well with those reported by Wang *et al.*[14]

Proton mobility was assessed by examining proton mean square displacements, which were computed from a set of ten independent Born-Oppenheimer *ab initio* molecular dynamics (AIMD) simulations. These were performed on a 2 × 2 × 1 configuration of the system shown in Fig. 6 having one excess proton, such that the system has an overall charge of +1 e. Simulations were performed at 800 K. Further details are given in Appendix B.1.

Calculations performed using DFT for charged systems under periodic boundary conditions impose an artificial counter-charge jellium background, which results in an error.[26] Bagusetty *et al.*[76] showed that this background charge error is not significant for computing the diffusion barriers for a similar charged system of 1-D hydroxylated graphane by comparing results with and without density-countercharge corrections.[27] The impact of charge error decreases with increasing volume of the supercell for fixed total charge. The supercell used in our AIMD calculations is about a factor of 4.5 larger in volume than that that used previously,[76] which indicates that charge corrections are not needed in this work. We also note that quantum effects such as diffraction and proton tunneling are neglected in this study. Based on previous work,[76] we estimate that proton conduction rates will increase significantly when quantum diffraction is accounted for, but that proton tunneling will have a negligible impact.

The Heyd-Scuseria-Ernzerhorf (HSE06) short-range screened hybrid functional [83, 84] was used for accurate band structure calculations because the PBE functional is known to underestimate the bandgap of semiconductors. We have evaluated the structural stability by exploring the harmonic phonon dispersion spectrum computed using the PHONOPY software package [85] in conjunction with VASP. The phonon calculations were carried out on a $3 \times 3 \times 1$ supercell (containing 90 atoms) constructed from the primitive cell configuration shown in Fig. 6.

3.3 Dynamics of Proton Conduction

We investigated the dynamic stability and proton conduction ability of hydroxygraphane containing one excess proton (H^+) by performing AIMD simulations at high temperatures (about 800 K). We observed that hydroxygraphane with an excess proton is stable (or at least metastable) because aside from proton hopping, no bond breaking events of the underlying structure were observed in any of the ten independent simulations at 800 K. Our analysis of the AIMD trajectories indicated that proton conduction occurs by hopping of an excess proton from one OH group to the next over a 2-D network of hydrogen bonds. We noted that the hydroxyl groups surrounding the center of excess charge (i.e., OH group with an excess proton) reorient themselves to accommodate the local changes made to the morphology due to the presence of the excess proton. The key to facile intrinsic proton conduction is the presence of a contiguous network of hydrogen bonds having an appropriate hydrogen bonding distance across the hydroxygraphane surface, coupled with the ability of the OH groups to rotate.[78, 35] We observed that proton conduction on hydroxygraphane takes place through a Grotthuss-like mechanism, where a proton is transferred from one OH group to another, followed by a different H^+ moving to the next OH group, as illustrated in Fig. 7. The mechanism of proton conduction is associated with a slight reorientation of the hydroxyl groups surrounding the excess charge, resulting in a reconfiguration of the hydrogen bonding network.

The proton mobility was quantified from the mean squared displacement (MSD) computed at multiple time origins and averaged over x and y directions along the plane of hydroxygraphane. A plot of the MSD as a function of time at 800 K is plotted in Fig. 8. The proton self-diffusion coefficient was estimated from the MSD plots as described in the Appendix B.1. Our computed value is $D = 1.1 \times 10^{-5}$ cm^2/s with an uncertainty of $\pm 2.6 \times 10^{-6}$ cm^2/s (twice the standard deviation). For comparison, the value of D for 1-D hydroxylated graphane at 800 K is 1.56×10^{-4} cm^2/s.[76] The observed reduction in the proton mobility is expected in going from a 1-D chain of hydroxylated graphane to a 2-D network in hydroxygraphane, and is due to the difference in the hydrogen bonding topology. There is a maximum of two hydrogen bonds (one donor and one acceptor) on any given OH group on 1-D hydroxylated graphane because there are only two neighboring OH groups. However, any OH group on hydroxygraphane has a coordination of six neighboring OH groups to which it can hydrogen bond. Hence, any given OH group could have three hydrogen bonds, one donor and two acceptors, and therefore the energy required to rotate an OH group is, on average, significantly higher than for the 1-D system.

Another difference between the 1-D hydroxylated graphane and 2-D hydroxygraphane cases is that protons can obviously only diffuse along the 1-D chain of OH groups in the former, but protons can diffuse in any direction on the hydroxygraphane surface. Indeed, our MSD data show that proton mobility in the x and y directions is statistically equivalent,

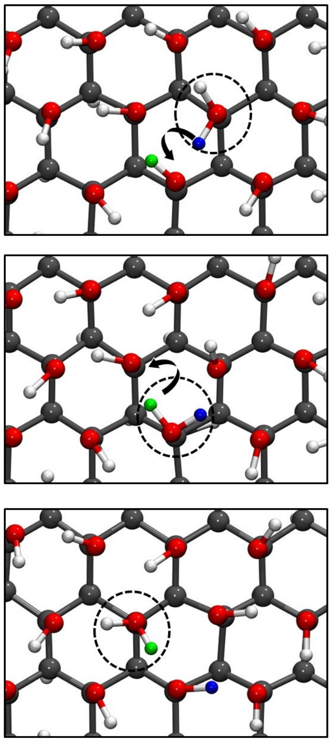

Figure 7: Snapshots of a proton conduction event in protonated hydroxygraphane from AIMD simulations at 800 K. An excess proton associated with a hydroxyl group is marked with a dashed circle to indicate the charge center. Protons participating in the conduction event are colored blue and green to aid in visualization. Hopping of these protons illustrate a Grotthuss-like mechanism (atom colors defined in Fig. 6).

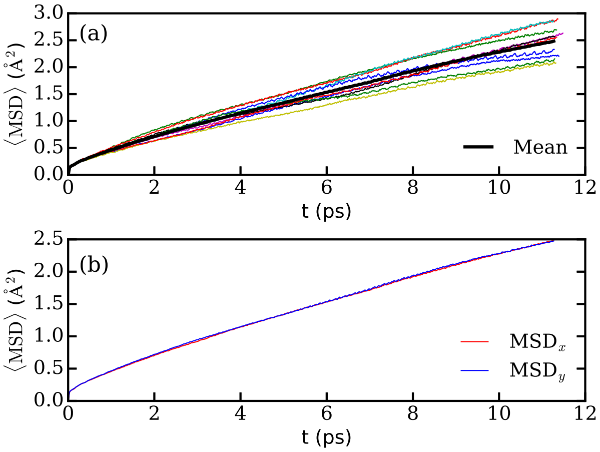

Figure 8: (a) Profiles of proton mean squared displacement as a function of time for hydroxygraphane with an excess proton at an average temperature of about 800 K. Thin lines in various colors are results from each of the ten uncorrelated simulations. The mean MSD profile is shown as the thick black curve. (b) Contributions of the proton MSD in x and y directions.

as can be seen from Fig. 8(b). Hence, hydroxygraphane having defects (e.g., missing OH groups or missing C atoms) will still conduct protons, whereas a missing OH group on 1-D hydroxylated graphane will result in a complete blockage of proton conduction.[76] The purpose of this paper is to establish that proton conduction does occur on hydroxygraphane, and to explore its mechanical and electronic properties. This paper does not attempt to fully characterize the diffusion coefficients and the corresponding conductivities, which can be determined from the Einstein relation and Nernst-Einstein equation[86], respectively. We will explore the temperature dependence of diffusivity and conductivity at longer time scales and with higher statistical precision in a future paper.

3.4 Electronic Properties

It is an obvious requirement that PEM materials be electronically insulating. We have computed the bandgap of hydroxygraphane using four different exchange-correlation functionals. We compared results from the PBE[17, 82] semi-local generalized gradient functional and three hybrid functionals, HSE06,[83, 84] PBE0,[87] and B3LYP,[88] which include different amounts of Hartree-Fock (HF) exchange. Results of these calculations are shown in Table 1. As expected, the bandgap predicted from PBE is significantly smaller than values computed from the hybrid functionals. We believe that the HSE06 functional is the most accurate of the exchange-correlation functionals we tested because it is known to be accurate for semiconductors.[89] The larger bandgap computed from PBE0 is likely a result of using a larger amount (25%) of full-range HF exchange, in comparison to B3LYP, which has 20% full-range HF exchange and HSE06 with 25% short-range HF exchange.

The band structure for hydroxygraphane computed from the HSE06 functional is shown in Fig. 14. We see from this figure that the bandgap is direct and is located at the Γ point. We note that the band gap reported by Wang *et al.* computed from the PBE functional is about 1 eV larger than our PBE value.

Table 1: Values of the bandgap of hydroxygraphane computed from various exchange-correlation (XC) functionals

XC functional	Bandgap (eV)
PBE	2.23
HSE06	3.43
PBE0	4.10
B3LYP	3.11

One might expect that an excess proton added to hydroxygraphane would create a localized charge center, i.e., one H atom bound to a hydroxyl group could be identified as the "proton" and would have a significantly larger positive charge than the rest of the H atoms bound to other OH groups. We have tested this hypothesis by computing the charge on each

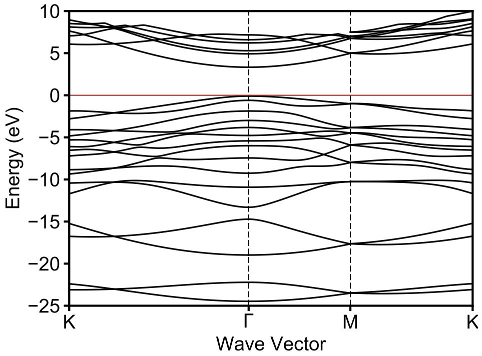

Figure 9: HSE06 electronic band structure of hydroxygraphane along a high-symmetry path. The Fermi level is shifted to zero energy and represented by a horizontal red line.

atom of hydroxygraphane with a single added proton using the Density Derived Electrostatic and Chemical (DDEC6) charge analysis approach.[25, 90] We found that the charges on H atoms bound to OH groups are all very similar, indicating that the excess proton is fairly delocalized (see Fig 30 and Tables 6 and 7 of Appendix B.2). This delocalization of the charge is consistent with our observation of a Grotthuss-like proton conduction mechanism. This is similar to the case for 1-D hydroxylated graphane [76] and for graphamine.[91] We have computed phonon dispersion curves using the finite-displacement method [85] to investigate the stability of hydroxygraphane (see Fig. 31 in Appendix B.3). Instabilities in the form of soft modes (modes with imaginary frequencies) were not found along any high-symmetry direction of the Brillouin zone under the harmonic approximation. The lack of soft modes indicates that hydroxygraphane is mechanically stable.

3.5 Elastic Properties

The elastic properties were investigated to provide insights into the mechanical rigidity of the hydroxygraphane. We have computed the in-plane Young's modulus Y, which is a 2-D version of Young's modulus, for hydroxygraphane as described in the Appendix B.4.

These calculations gave $Y = 252$ J/m^2. For comparison, this value of Y falls in-between the reported values for chair graphane (243 J/m^2) [92, 93] and graphene (340 ± 50 J/m^2) [94]. The increase in Y for hydroxygraphane relative to chair graphane is the result of the 2-D network of hydrogen bonds on the surface of hydroxygraphane, which provides resistance to in-plane stretching and compression. We have also computed Poisson's ratio ν for hydroxygraphane as described in Appendix B.4. Our computations gave $\nu = 0.11$, which is comparable to graphene ($\nu = 0.16$) [94] and almost double that of the parent material, chair graphane ($\nu = 0.07$).[92] Our computed values of Y and ν for hydroxygraphane indicate that it has reasonable mechanical properties for a PEM material.

3.6 Conclusions

We have demonstrated *in silico* that hydroxygraphane is an intrinsic proton conduction material, capable of conducting protons anhydrously through a Grotthuss-like mechanism, whereby a proton hops from one OH group to another, followed by a different proton hopping to a third neighboring OH group. It is the contiguous network of hydrogen bonds on the surface of hydroxygraphane that provides the necessary pathways for proton transport. We believe that proton conduction will occur through a similar mechanism for any surface having a network of hydrogen bonded moieties, even in the complete absence of water. Importantly, morphological defects, such as the absence of one or more adjacent hydroxyl groups, will have a minor impact on proton conduction because of the presence of redundant percolating hydrogen bonding pathways. Our DFT calculations provide evidence that hydroxygraphane has the requisite electronic and mechanical properties for making a practical proton exchange membrane material capable of operating at intermediate temperatures and low humidities. Given the recently reported synthesis of hydroxygraphane, [72] our work provides strong motivation to experimentally test our predictions of anhydrous proton transport.

4.0 Graphamine: Amine Functionalized Graphane for Intrinsic Anhydrous Proton Conduction

This work was published as: Bagusetty, A., Livingston, J., & Johnson, J. K. (2018). Graphamine: Amine-Functionalized Graphane for Intrinsic Anhydrous Proton Conduction. *J. Phys. Chem. C, 123(3), 1566-1571.*

4.1 Introduction

Proton exchange membrane (PEM) fuel cells are becoming increasingly important for use in applications such as fuel cell electric vehicles and portable power generation.[54] This has lead to a search for more cost-effective and robust materials for proton conduction (PC) to replace Nafion, the current default PC material. One of the main shortcomings of Nafion is that it is not an inherent PC material, i.e., it only conducts protons when hydrated. This leads to problems with water management and results in a relatively narrow window of operating temperatures (< 80°C) for Nafion-based PEM fuel cells. Development of intrinsically PC materials would allow PEM fuel cells to operate over wider temperature ranges, even under anhydrous conditions.[76, 68, 6]

New PC materials designed to function under anhydrous or low-humidity conditions include organic polyelectrolytes [58] and crystalline porous materials, such as cucurbituril-based organic molecular porous materials [67], metal organic frameworks [62, 57], metallopolymers[95] and covalent organic frameworks.[59, 69] However, existing materials are subject to a variety of limitations,[57] highlighting the need for development of new PC materials that fulfill all property and cost requirements for PEM fuel cells.

Recently, graphane [71] functionalized with a 1D chain of hydroxyl groups has been shown to exhibit facile PC under anhydrous conditions.[76] The key advantage of hydroxylated graphane compared with other anhydrous PC materials is that the OH groups are covalently bound to the surface with the correct spacing to form a percolating network of

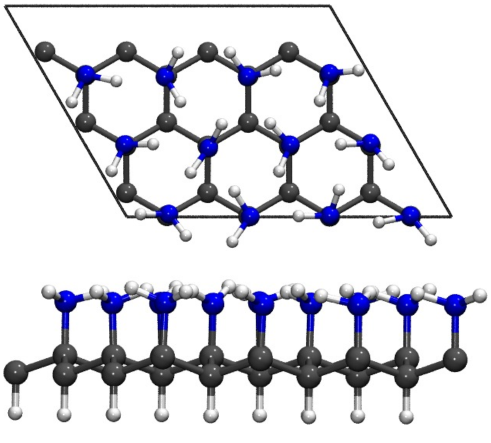

Figure 10: Schematic representation of top and side view of a graphamine supercell (carbons in gray, nitrogens in blue, hydrogens in white). Solid lines show the supercell boundaries in the $\vec{a}$ and $\vec{b}$ directions.

hydrogen bonds on the surface, which is required for rapid anhydrous PC. Moreover, this network is relatively rigid, meaning that thermal fluctuations do not disrupt the hydrogen bonding network as much as in more flexible materials, such as polymers. Given these features, we seek to identify other functional derivatives of graphane for robust anhydrous PC. In this work, we examine surface functionalization of chair graphane with amine groups (–NH_2) as a potential anhydrous PC material. The objectives of this paper are to: (1) test whether amine-functionalized graphane (graphamine) can conduct protons under anhydrous conditions, (2) estimate the bandgap of graphamine, and (3) explore the mechanical properties of graphamine. The bandgap is of interest because any practical PEM material must be electrically insulating to avoid short circuiting the fuel cell. Good mechanical properties are required for constructing robust fuel cell stacks. We here report density functional theory (DFT) calculations predicting the PC, electronic, and mechanical properties of graphamine.

4.2 Computational Methodology

All the AIMD simulations were performed using the Quickstep module [96] in the CP2K package [97]. The Perdew-Burke-Ernzerhof (PBE) [17] generalized gradient approximation (GGA) exchange-correlation functional was used, along with a hybrid Gaussian and plane waves method, [98] employing DZVP-MOLOPT basis sets [99] with GTH pseudopotentials [100]. A plane-wave energy cut-off of 440 Ry and a relative plane-wave energy cut-off of 40 Ry for the reference grid represented by Gaussian functions in a multi-grid domain is used. The orbital transformation method [101] was used to optimize the wave functions at each step of the simulations. AIMD simulations within the NVT (canonical) ensemble were performed for thermal equilibration using colored-noise GLE thermostat [102, 103]. A time step of 0.5 fs for integration under Γ point sampling of the Brillouin zone was employed. A set of five independent NVE (microcanonical) ensemble simulations were performed starting from initial configurations (positions and velocities) obtained from thermalized NVT simulations. The NVE AIMD simulations were run for 30 ps for data collection.

Electronic and mechanical properties (phonon density of states and elastic constants) require a higher level of accuracy than PC dynamics calculations; we have therefore carried out these calculations using the Vienna *Ab initio* Simulation Package (VASP) [79, 15, 80]. Projector augmented-wave pseudopotentials [81] were employed to describe the interactions between valence electrons and frozen cores. A kinetic energy cut-off for the plane-wave expansion of 520 eV was used. We used the PBE[17] GGA exchange-correlation functional for the structural and mechanical calculations. The structural relaxation and lattice properties (a = 10.703 Å, b = 8.027 Å, c = 20.0 Å, α=β=90°, γ=120°) for the supercell shown in Fig. 10 were computed on a $7 \times 7 \times 1$ **k** point grid. The energies were converged to within 10^{-9} eV and the ionic positions were optimized until the forces were converged to less than 10^{-3} eV/Å. A vacuum spacing of 20 Å in the $\vec{c}$ direction was used to mitigate the periodic interactions. Harmonic phonon dispersion calculations were computed at the PBE level of theory using Phonopy [85]. We used a $3 \times 3 \times 1$ supercell of the configuration shown in Fig. 10 for the phonon calculations.

Our DFT calculations were carried out using a single layer of graphamine supercell, as shown in Fig. 10 (see Appendix C for atomic coordinates). Graphamine was constructed by replacing the surface H atoms on one side of graphane with amine groups. As a result of functionalization, the C–C bond length increases from 1.54 Å [93] to 1.62 Å. Alternately, one could completely functionalize both sides of graphane, producing a fully saturated graphamine to increase the overall conduction. We employed *ab initio* molecular dynamics (AIMD) simulations performed at a temperature of about 1000 K in the constant energy (microcanonical) ensemble to estimate the thermodynamic stability and proton diffusivity of graphamine having one additional proton per supercell, such that the system has a +1 e charge. It is well known that periodic DFT calculations of charged systems are problematic because of the errors due to imposing an artificial jellium background.[26] However, Bagusetty et al. have shown that no significant errors arise for computing PC on hydroxylated graphane.[76] We therefore do not apply any charge-based corrections in this work.

4.3 Results and Discussion

4.3.1 Structural Configuration

Chemical functionalization of sp^3 hybridized graphane to form aminated graphane gives a C—N covalent bond length of 1.48 Å in comparison to the semi-ionic C—N bond length of 1.518 Å reported for amine functionalized graphene.[104] The hydrogens of the amine groups in graphamine tend to orient roughly towards the centers of the underlying graphane hexagons rather than to align with the C—C bonds, as seen in Fig. 10. The average H—N—H bend angle is 107.8°, as computed for the configuration in Figure 10. We have computed the electron localization function for graphamine with one excess proton; the resulting isosurfaces is shown in Fig. 11. We see from this plot that hydrogen atoms on an amine group are generally oriented toward the lone pairs on a neighboring nitrogen, confirming the expectation that graphamine forms a hydrogen bonding network. The isosurface densities along the amine group with an excess proton (highlighted with a dotted circle in Fig. 11) indicate the

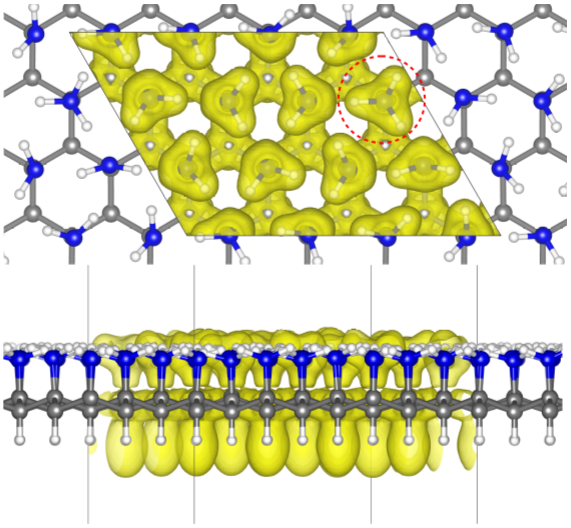

Figure 11: Top and side views of an electron localization function with an isosurface value of 0.6 for graphamine with an excess proton. Dotted circle represents the amine group with an excess proton.

covalent bonding nature of the excess proton with the –NH_2 group, as seen by the apparent equivalence of the isosurface for all three H atoms. This is also confirmed from the consistency of the N–H bond lengths on the –NH_3 group, which are 1.01, 1.06, and 1.06 Å. An analysis of the hydrogen bonds gave a mean N$\cdots$H and N$\cdots$N hydrogen bond distance of 2.2(±0.32) and 2.68(±0.08) Å, respectively. In comparison, hydrogen bonding distances for N$\cdots$H and N$\cdots$N in liquid ammonia are reported to be 2.7 and 3.35 Å, respectively.[105] The shorter hydrogen bonding donor-acceptor distances observed in graphamine compared to liquid ammonia, coupled with the observation that the NH_2 groups on graphamine can rotate (as seen from AIMD simulations) indicate that proton transfer should be more facile on graphamine than in liquid ammonia.

4.3.2 Proton Conduction Dynamics

An analysis of the AIMD simulations showed that PC occurs through proton hopping along the 2-D hydrogen bonding network of graphamine, accompanied by rotation of NH_2

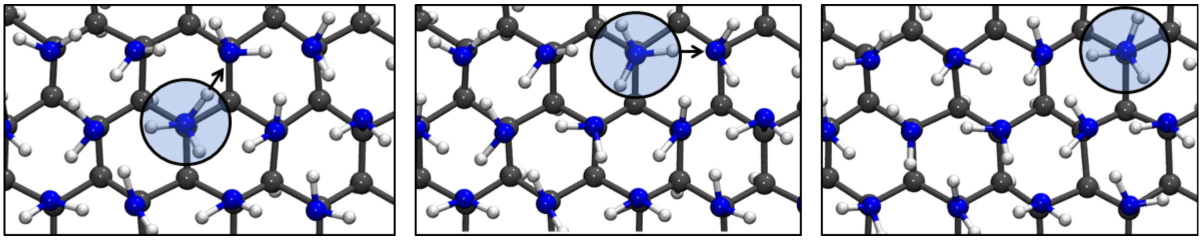

Figure 12: Snapshots from an AIMD simulation showing an example of a Grotthuss-like proton conduction event. The system contains one excess proton and the charge center is marked with the shaded circle in each snapshot. The direction of the proton hop is indicated by the arrow (colors are defined in Figure 10).

groups. Given the morphology of graphamine, the protons are transported by hopping between adjacent amine groups in a Grotthuss-like mechanism, [31] facilitated by hydrogen bonding between neighboring amine groups. The average number of hydrogen bonds (donor and acceptor) per NH_2 group is about 3, as computed from a distance-based criterion. Hydrogen bonds were determined based on a geometric distance criterion of an N—H distance ≤ 2.7 Å for non-bonded atoms.[105] Hydrogen bond distance data and PC events were collected from AIMD trajectories at 1000 K.

An example of a proton hopping event obtained from snapshots from an AIMD simulation is shown in Fig. 12, from which one can observe only slight reorientation of the neighboring amine groups as a result of the hopping event. We have computed mean square displacements (MSD) of all H atoms bound to N atoms from AIMD simulations at about 1000 K for the graphamine system with one proton. The plot of MSD/t, where t is time is shown in Fig. 13. The flat profile (MSD/t = constant at large values of t) is a signature of Fickian diffusion, i.e., $dr^2 \propto Ddt$ where D is the Fickian diffusion coefficient.[28] The diffusion coefficient at 1000 K, estimated from the Einstein relation ($D = \lim_{t\to\infty}\langle|r(t)-r(0)|^2\rangle/(2dt)$, where $d = 2$ is the dimensionality of the system) is 1.62×10^{-5} cm^2/s. For comparison, simulations of PC in Nafion at room temperature give D in the range of 1.4×10^{-6} cm^2/s to 1.7×10^{-5} cm^2/s, depending on the level of hydration.[20] We note that proton diffusivity in Nafion drops dramatically above about 80° C because of the loss of water from the membrane.[10] We have plotted the components of MSD/t in the x and y directions in the inset of Fig. 13. The approximate equivalence of the MSD in these directions implies that the diffusivity in the x and y directions is the same.

We observed from AIMD simulations that the PC mechanism involves a proton moving from the —NH_3 group to a neighboring —NH_2 group, as seen in Fig. 12. One might reasonably assume that one or more of the H atoms on the —NH_3 group would have a significantly larger charge than the H atoms on the —NH_2 groups on the graphamine surface. In other words, it seems reasonable to assume that the center of charge would be highly localized. We have checked this assumption by computing the charge distribution on the H atoms bound to N atoms for the system with a single proton using the Density Derived Electrostatic and Chemical (DDEC6) charge analysis approach [90]. However, our DDEC6 calculations show that the charge is highly delocalized (see charge analysis in Fig. 35 and Tables 9 and 10 of the Appendix C). The largest value of the charge is 0.287 e, and while it does belong to an H atom on the —NH_3 group, this value is only slightly larger than the next largest charge of 0.277 e, which is on an —NH_2 group. The mean charge on all H atoms bound to N is 0.257 e and the standard deviation is 0.013 e. This indicates that the charge center is delocalized, even though graphamine is a wide bandgap semiconductor (as shown below).

4.3.3 Mechanical and Electronic Properties

Having established that graphamine has the ability to conduct protons under anhydrous conditions, we turn to questions of whether it has suitable electronic and mechanical properties for a PEM material. Specifically, PEM materials must be electrically insulating and mechanically robust.

4.3.4 Electronic Band Structure

Graphane is a wide bandgap material with a direct bandgap of 3.5 eV as estimated from GGA for the ground state chair conformation.[106] Functionalization of graphane can reduce the bandgap; it has been reported that introducing a hydroxyl group defect by the

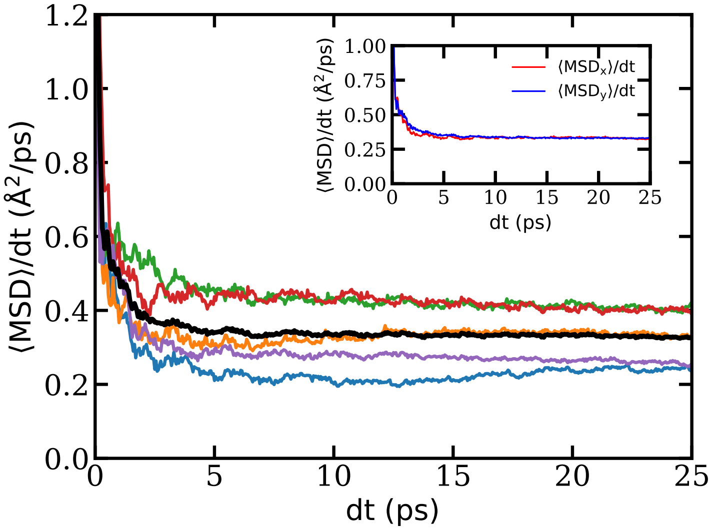

Figure 13: Plots of the mean square displacements divided by time of all the H atoms bound to N atoms on the graphamine surface having one proton. Plots for five independent runs are shown in various colors and the average of the five runs is shown as the thick black curve. The average temperature of the simulations was about 1000 K. Inset shows the isotropic nature of diffusivity in the x and y directions.

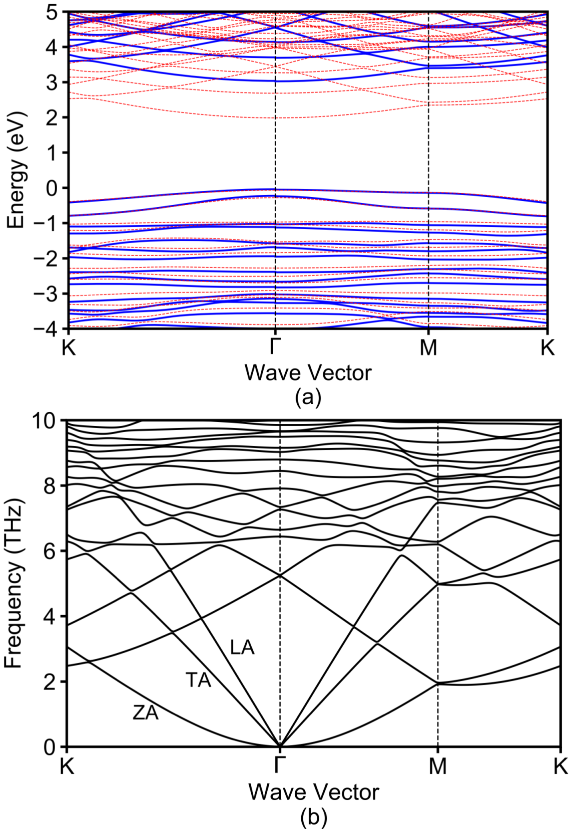

Figure 14: (a) PBE (dashed red lines) and HSE06 (solid blue lines) band structure of graphamine along high-symmetry paths showing a direct bandgap of 2.04 and 3.08 eV respectively. The Fermi level is shifted to zero energy. (b) Phonon dispersion curves calculated for graphamine.

replacement of an H atom in a 3 × 3 graphane supercell reduces the GGA bandgap to 3.3 eV.[106] Replacing all the H atoms on one surface of graphane with hydroxyl groups gives a material with an estimated bandgap of 3.22 eV [14]. Given these trends, we expect that the bandgap of graphamine will be reduced with respect to graphane. We employed the Heyd-Scuseria-Ernzerhorf (HSE06) hybrid functional [83] to obtain an accurate band structure because it is well-known that the GGA formalism generally underestimates the bandgap of semiconductors. We have computed the band structure of graphamine using both the PBE and hybrid HSE06 functionals. Both methods predict that graphamine is a wide-bandgap semiconductor with a direct gap at the Γ point. The PBE bandgap is 2.04 eV while the screened-hybrid HSE06 functional, which predicts accurate bandgaps for typical semiconductors, [89] gives a gap of 3.08 eV. Both the PBE and HSE06 band structures are shown in Fig. 14(a). An upward offset of the valence band maximum (VBM) is observed when going from PBE to HSE06 leading to the increase in the bandgap from 2.04 eV to 3.08 eV. There are no significant differences observed for the alignment of conduction band minimum (CBM) using both the functionals. These calculations indicate that graphamine has an appropriate bandgap to be used as a PEM material.

In the Figure 15, we show a plot of the partial density of states indicating the contribution from various atomic orbitals. The contribution to the valence band maximum is dominated by the amine groups, while the regime close to conduction band minimum is from the sp^3 carbon atoms. This suggests that an electron charge transfer occurs from the plane of amine groups to the sp^3 carbon atoms.

4.3.5 Phonon and Elastic Properties

We have computed the phonon dispersion curves for graphamine in order to estimate its stability. The curves are plotted in Figure 14(b). The absence of soft modes (modes with imaginary frequencies) along any high-symmetry direction of the Brillouin zone indicates that there are no instabilities in graphamine, within the harmonic approximation. Only the lower frequency dispersion branches with values less than 10 THz are shown in Figure 14(b) in order to focus on the acoustic modes along principle directions (the full phonon

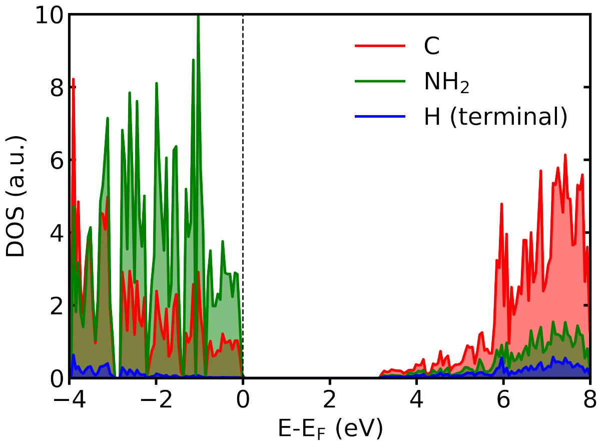

Figure 15: Calculated partial density of states according to the atomic types for graphamine.

dispersion spectrum in shown in Figure 36 of Appendix C). The longitudinal acoustic LA and transverse acoustic TA branches show linear profiles, while the out of plane acoustic ZA modes show quadratic dispersion. This is very similar to the behavior observed for graphene and its layered derivatives.[107] We have also calculated the phonon density of states, shown in Figure 36 of Appendix C. Thermal properties of graphamine computed from the phonon density of states, are shown in Figure 37 from Appendix C. We performed calculations for the elastic properties under harmonic strain limits (ϵ ¡ ± 2%) by applying uniaxial and equi-biaxial in-plane strain. Calculation of in-plane Young's modulus, (Y) and Poisson's ratio, (ν), are estimated from elastic constants C_{11} and C_{12} related by the expressions (details are presented in Appendix C.4),

$$Y = \frac{C_{11}^2 - C_{12}^2}{C_{11}} \tag{4.1}$$

$$\nu = \frac{C_{12}}{C_{11}} \tag{4.2}$$

The calculated value of Y is 262 J/m^2, which falls in between the reported values for chair graphane (243 J/m^2) [92, 93] and graphene (340 ± 50 J/m^2).[94] Note that the in-plane Young's modulus is appropriate for a 2-D material and has different units than the Young's modulus for a bulk material, i.e., the correct units for the in-plane Young's modulus is energy per unit area, rather than energy per unit volume. The reduction of the in-plane Young's modulus for chair graphane relative to graphene is the result of sp^3 hybridization, which makes graphane easier to deform under loading compared to sp^2 hybridized graphene. Our calculations show that functionalization of graphane with amine groups yields a higher value of Y compared to graphane because the hydrogen bonded network of amine groups provides additional resistance to applied strain. Hence, there should be an opportunity to tune Y to a certain degree through control of the degree of functionalization. We note that our results are for graphamine with a single side functionalized with amine groups. We predict that functionalization of both sides of graphane with amine groups will produce an even larger value of Y. The value of Poisson's ratio was determined to be 0.13, which is close to the values reported for graphene (0.16) [94] and almost double than chair graphane (0.07) [92]. An observed increase in the value of ν compared to chair graphane can be attributed to the formation of a 2-D network of hydrogen bonding layer from amine groups. This dense network of hydrogen bonds provides resistance to longitudinal elongation thus increasing the value of ν.

4.4 Conclusions

In summary, we have predicted that graphamine is a promising PEM material for facilitating PC under anhydrous and low-humidity conditions. Graphamine has a contiguous network of hydrogen bonds that are much closer than in liquid ammonia. This compressed hydrogen bonding network, coupled with the ability of the —NH_2 groups to rotate, facilitates PC in the compete absence of water, as seen from our AIMD simulations. We have shown that graphamine is a wide bandgap semiconductor, having a direct gap of 3.08 eV. The phonon density of states and dispersion relations indicate that graphamine is mechanically stable. It has an in-plane Young's modulus larger than unfunctionalized graphane. Amine functionalized graphene oxide has been experimentally synthesized,[108, 109, 110, 111, 112, 113] but that fully aminated graphane has not yet been produced. Our work provides motivation for synthesis and characterization of more uniformly functionalized graphamine.

5.0 Role of Nuclear Quantum Effects on the Isotopic Fractionation of Water Isotopologues

5.1 Introduction

The relative abundance of an isotope between two coexisting phase has been of interest for several decades and more specially towards the understanding of liquid-vapor isotope fractionation ratio (IFR). Recent analysis from IFR studies have revealed a new perspectives regarding the role of microalgae inducing isotope fractionation in Uranium.[114] This IFR have been historically related to the ratio of vapor pressures of light and heavy isotopic species in the liquid and vapor phases.[115, 116, 117] Moreover, there are several studies focused on the deuterium and hydrogen (D/H) IFR in water liquid-vapor [117, 118] and vapor-ice phases.[119, 120] In contrast, tritium and hydrogen (T/H) IFR in water has not been investigated as extensively.[121]

Nuclear quantum effects (NQE) are known to impact the properties of water in subtle ways. The main reason for this is that hydrogen bonding is central to water's unique properties, and hydrogen bonding is subject to NQE, even at room temperature, because of the light mass of the hydrogen atom. The salient role of nuclear quantum effects associated with the hydrogen and its isotopes has long been of interest.[122, 123] Although the chemical composition of water being H_2O is quite simple, there are a number permutations for hydrogen isotopes (^1H, ^2H, ^3H) and oxygen isotopes (^{16}O, ^{17}O, ^{18}O) that can alter the inherent properties. The determination of relative abundance of these isotopes in any given two phases in equilibrium poses a challenge. In this work, we characterize the H/X (X:D,T) fractionation ratio associated with the liquid-vapor equilibrium involving deuterated water (HDO) or tritiated water (HTO). This equilibrium fractionation ratio determines the ratio of isotopic species when liquid and vapor phases are in equilibrium.

Due to the lighter mass of the hydrogen, nuclear quantum effects (NQEs), such as delocalization, zero-point energy, and tunneling, manifest their effects on the nature of hydrogen bonds and in turn become the source of the anomalous behavior of water. These NQEs are much less pronounced for tritium than the other isotopes of hydrogen because it has the heaviest mass. Tritium can readily react with water or hydrocarbons from the surrounding environment via isotopic exchange of the hydrogen atoms. Despite being of interest for a wide range of technological applications, there has been a significant gap in the fundamental understanding of quantum effects and its associated dynamics of tritium with the surrounding environments.[124, 125] In contrast, hydrogen/deuterium (H/D) fractionation has been extensively assessed ranging from interstellar environment,[126, 127] proteins,[128] rocks samples[129] to water at triple point[130] and phase equilibrium.[118]

With the advances in molecular simulation methodologies, the inclusion of isotopic effects have emerged from simple ratio of vapor pressures, Van't Hoff relation[131] and Feynman-Hibbs effective potentials[132] to quantum instanton approximation,[133] quasi-harmonic approximation,[134] multiple time step integrators,[135] thermodynamic integration,[136] free energy pertubation,[134] and direct thermodynamic estimators.[137, 138] Along with an emerging adoption of machine learning techniques to molecular simulations, neural network (NN) based force fields have gained popularity for their higher accuracy, lower computational costs, transferability, ease of adoption and scaling. With the limitations offered by the conventional classical force fields and the computationally intensive nature of first principles based methods, there has been tremendous progress towards the development of NN-based force fields for water clusters [139, 140, 141] and bulk water.[142, 143, 144, 145, 146] Several NN-based force fields were also reported to explicitly investigate NQEs of water.[130, 147, 148] Recently, Ceriotti et al.[147] have reported a flexible and dissociable revPBE0-D3-based NN force field for bulk water that can reproduce the electronic structure description and NQEs in comparison to experiments. With the computational performance, linear-scaling characteristics and its integration with the widely adopted molecular simulation framework LAMMPS [149], this revPBE0-D3-based NN force field was used to evaluate the liquid vapor isotope fractionation ratio of water isotopologues, HDO and HTO. In this work, we demonstrate theoretical predictions of liquid vapor isotope fractionation ratio of water isotopologues (HDO and HTO), inversion temperature for their flipping of abundance from liquid to vapor phase and with an evaluation of the NN-revPBE0-D3 based water model.

5.2 Simulation Methodology

5.2.1 Isotope Fractionation Ratio

The relative abundance of any isotopic species for a given thermodynamic media is governed by the equilibrium isotope fractionation ratio. In this work, the thermodynamics related to the isotope fractionation ratio between two media specifically liquid(l) and vapor(v) for the two isotopic species X and $X^{'}$ is denoted by $\alpha_{(\mathrm{l-v})}$ and given by the equilibrium,

$$\mathrm{X}_{(l)} + \mathrm{X}^{'}_{(v)} \leftrightharpoons \mathrm{X}_{(v)} + \mathrm{X}^{'}_{(l)} \tag{5.1}$$

The $\alpha_{(\mathrm{l-v})}$ for the above equilibrium is determined by the atomic ratios of naturally abundant isotope (X) and rare isotope $X^{'}$ in both liquid and vapor phase and conveniently associated with the change in equilibrium free energy ($\Delta\Delta\mathrm{A}_{\mathrm{l-v}}$) as given by,

$$\alpha_{(l-v)} = \frac{(X^{'}/X)_l}{(X^{'}/X)_v} = e^{-\beta\Delta\Delta A_{l-v}} \tag{5.2}$$

where $\Delta\Delta\mathrm{A}_{\mathrm{l-v}} = \Delta\mathrm{A}_{\mathrm{l}} - \Delta\mathrm{A}_{\mathrm{v}}$, is the difference between the change of free energy for isotopic substitution in liquid and vapor phase.

The $\alpha_{(\mathrm{l-v})}$ is traditionally determined by performing thermodynamic integration with respect to a virtual isotopic mass (μ) undergoing transition from the abundant isotopic mass $\mu = X$ to rare isotopic mass $\mu = X^{'}$ given by,

$$\Delta\Delta A_{l-v} = \int_{X}^{X^{'}} \frac{\Big\langle E_k(\mu)\Big\rangle_v}{\mu} - \frac{\Big\langle E_k(\mu)\Big\rangle_l}{\mu} d\mu \tag{5.3}$$

where $\langle \mathrm{E}_{\mathrm{k}}(\mu)\rangle$ is the quantum kinetic energy of nuclei with mass μ.

We consider two separate isotopic exchange reactions in which tritium present in the diluted tritiated water liquid phase is replaced as tritium oxide or tritiated water vapor (HTO). Isotopic exchange involves the transfer a HTO molecule in the vapor phase to the liquid phase with a simultaneous transfer of a H_2O molecule from liquid phase to vapor phase given the reaction,

$$\mathrm{H_2O}_{(l)} + \mathrm{HXO}_{(v)} \leftrightharpoons \mathrm{H_2O}_{(v)} + \mathrm{HXO}_{(l)} \tag{5.4}$$

5.2.2 Path Integral Molecular Dynamics

The IFR was determined for the above equilibrium reaction using PIMD framework as implemented in the python package i-PI[150, 151] to evolve nuclear degrees of freedom. The forces and energies for the nuclear coordinates of the system were evaluated using LAMMPS.[149] The liquid water phase configuration consisted of 216 water molecules and a single water molecule in vacuum to represent the vapor phase. The PIMD simulations were performed for temperatures ranging between 300 and 620 K under NVT ensemble with the configurations kept at appropriate densities. A time step of 0.25 fs and 32 imaginary time slices or beads were used for each particle with in PIMD framework as it was shown to sufficiently convergence the desired properties for the temperature range.[130, 118] Our simulations were performed using two different water models (a) a flexible anharmonic q-TIP4P/F water model[152], and (b) a revPBE0-D3-based neural network (NN-revPBE0-D3) potential.[147] We note here that the NN-revPBE0-D3 potential was shown to predict the structural properties and contributions of NQE quite accurately for the systems of cubic ice, hexagonal ice and liquid water.[147] Interface for the NN potential with LAMMPS was accomplished by using USER-NN package.[153]

5.2.3 Acceleration Schemes

Given the computationally expensive nature of evaluating the thermodynamic mass integral, we have used the scheme of direct scaled-coordinates (SC) estimator to evaluate isotope fractionation ratio $\alpha_{(\mathrm{l-v})}$.[137] The SC estimator was chosen over direct thermodynamic estimator to evaluate $\alpha_{(\mathrm{l-v})}$ because of the inherent inefficiency in handling this transformation mass ratio ≈ 3 and sensitive to statistical errors with the number of time slices.[137, 134] The protocol essentially involves a virtual isotopic substitution of one of the H atom in a random H_2O molecule to the T atom for any given thermodynamic phase. With the relative ratio of partition functions of both the isotopes involved in the substitution for each phase, $\alpha_{(\mathrm{l-v})}$ is directly determined. To reduce any statistical errors associated with the direct substitution of a single H_2O molecule in the liquid phase, we have employed quantum alchemical exchanges to also sample the rest of the water molecules for direct substitution, to avoid performing multiple independent simulations.[154] It was reported that a direct substitution associated with H/D fractionation leads to a large fluctuations in the estimator.[134] Hence, a similar strategy as reported in Ref. [130], was adopted to perform back substitution starting with a heavier isotope atom ($\mathrm{m_T}$=2.992 $\mathrm{m_H}$, $\mathrm{m_D}$=1.9984 $\mathrm{m_H}$) to hydrogen atom ($\mathrm{m_H}$) over few intermediate masses ($\mathrm{m_1}$=2.5 $\mathrm{m_H}$, $\mathrm{m_2}$=2.0 $\mathrm{m_H}$, $\mathrm{m_3}$=1.5 $\mathrm{m_H}$). The resultant H/T fractionation ratio for the l-v equilibrium is determined by the inverse combined product of the fractionation ratio of the intermediate masses involved in the back substitution given by,

$$\alpha_{l-v}^{\mathrm{H}\rightarrow\mathrm{X}} = \frac{1}{\left(\alpha_{l-v}^{\mathrm{X}\rightarrow\mathrm{m_1}} \cdot \alpha_{l-v}^{\mathrm{m_1}\rightarrow\mathrm{m_2}} \cdot \alpha_{l-v}^{\mathrm{m_2}\rightarrow\mathrm{m_3}} \cdot \alpha_{l-v}^{\mathrm{m_3}\rightarrow\mathrm{m_H}}\right)} \tag{5.5}$$

5.3 Results and Discussion

5.3.1 Isotope Fractionation of Water Isotopologues, HDO and HTO

The liquid-vapor IFR of H/D and H/T for the equilibrium reaction in Eq. 5.4 was shown in the Fig. 16. An inversely proportional relation between IFR and the square of the temperature was reported.[157] Our simulations predicted a crossover inversion temperature for which the isotopic abundance of the heavier water isotopologues changes from the liquid to vapor phase as the temperature increases. Over the temperatures regime ($<$ 400 K), the enrichment of HDO and HTO was preferred in the bulk liquid phase over vapor phase implied by the value of $\alpha > 1$. At 293 K, the value of 10^3 log(α) for H/T is greater than H/D indicating that the selectivity of HTO/H_2O is larger than that for HDO/H_2O in the liquid phase as estimated from the simulations and as well as experiments. Similarly, at 613 K, the enrichment of HTO in the vapor phase is larger than that for HDO. However, the crossover for enrichment of HTO and HDO from liquid to vapor phase was observed at a temperature of about 470 K and 550 K respectively (inset of Fig. 16).

In comparison to experiments, the magnitude of 10^3 log(α) for both the H/D and H/T IFR was over estimated by the simulations employing the q-TIP4P/F water model as seen in Fig. 16. We note here that the inversion temperature for H/D determined from the

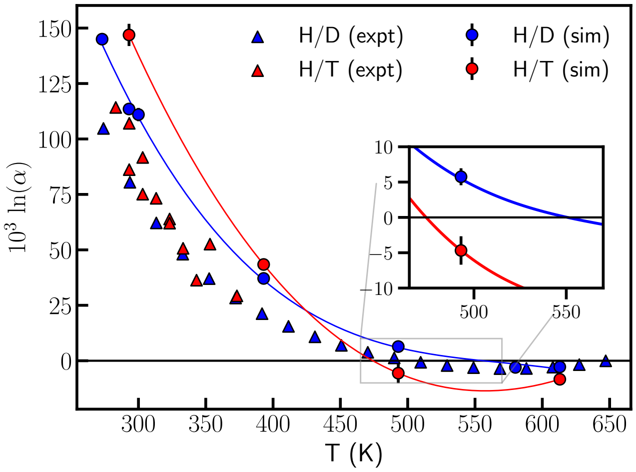

Figure 16: Liquid-vapor equilibrium isotope fractionation ratio (IFR) for HXO (X: D,T). Inversion temperature of IFR was observed above 490 K and 550 K for T and D respectively. Inset shows the temperature regime of isotopic inversion from liquid to vapor abundance for T and D. H/T is shown for experiments (red triangles)[155, 156] and simulations (red circles). Data for H/D from experiments (blue triangles)[116] and simulations (blue circles, this work & Ref. [130]). The solid lines are just a guide for the data obtained from simulations using q-TIP4P/F water model.[152] Standard deviations are indicated by error bars. The data is shown in Table. 12 and 11 of Appendix D.

simulations was about 550 K in comparison to 500 K as reported from the experiments.[116] This agrees well with the similar theoretical observations reported by Markland et al.[118] for H/D. Due to the lack of experimental studies for the higher temperature ranges of H/T IFR, no such comparisons about the inversion temperature was possible between the simulations and experiments.

The theory of vapor pressure isotope effects (VPIE) was historically employed to study the system of H_2O/HTO under equilibrium vaporization for a wide range of temperatures.[155] Under this formalism, the value of $\alpha_{(l-v)}$ were approximated for any given water isotopologue (HXO) by the ratio of partial pressure of H_2O to its heavier isotopologue given by the relation:

$$P^s_{\mathrm{H_2O}}/P^s_{\mathrm{HXO}} \approx \alpha_{(l-v)} = \frac{(X'/X)_l}{(X'/X)_v} \tag{5.6}$$

where $\mathrm{P}^s_{\mathrm{H_2O}}$ and $\mathrm{P}^s_{\mathrm{HXO}}$ are the saturation vapor pressures of H_2O and HXO respectively. By employing VPIE, an approximation to the temperature of inversion for IFR from liquid to vapor phase for HDO and HTO was approximated to be around 500 K and 550 K respectively. This interpretation of IFR from the VPIE provides us with an estimation of the range of temperatures for the inverse IFR.

5.3.2 Evaluation of NN-revPBE0-D3 Potential for IFR

Fig. 17 shows a comparison for the prediction of 10^3 log(α) for H/D IFR using NN-revPBE0-D3, q-TIP4P/F with the experimental data. When it comes to the H/D IFR, NN-revPBE0-D3 water model produces the most accurate results in agreement with the experiments. Over the regime of HDO abundance in liquid phase, the NN-revPBE0-D3 performs better over q-TIP4P/F water model but the error marginally increases for the temperature 613 K, where the isotopologue abundance is preferred in vapor phase. At the lowest temperature of 293 K, the well-known q-TIP4P/F water model over predicts the H/D IFR by over 40%, where as the average error margin for NN-revPBE0-D3 model is only 12%. The tabulation of 10^3 log(α) for both the H/D and H/T were reported in Table. 11 and 12. Moreover, a different NN-based water model (NN-B3LYP-D3) trained from B3LYP

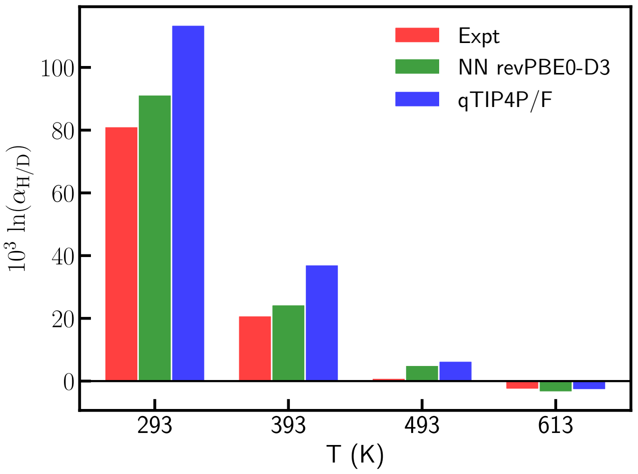

Figure 17: Evaluation of the water models q-TIP4P/F[152] and NN-revPBE0-D3[147] for the determination of H/D isotope fractionation ratio in comparison with experiments.

functional with D3 dispersion correction reported an accuracy for H/D liquid vapor IFR in comparison to experiments[116] with an average over-prediction of about 43% for the temperatures, 273 and 300 K.[130] The H/T liquid vapor IFR estimated from NN-revPBE0-D3 observe a similar trend as seen for H/D IFR with the values predicted by NN-revPBE0-D3 were lower than q-TIP4P/F (see Table. 11). We note here that the inversion of isotope fractionation ratio into the vapor phase abundance of HTO was predicted by qTIP4P/F at 493 K where as the liquid phase abundance was suggested by the NN-revPBE0-D3 for the same temperature. However, there is also a general agreement of both the water models predicting a relative abundance of HTO over HDO ($\alpha_{\mathrm{H/T}} > \alpha_{\mathrm{H/D}}$) in both the liquid and vapor phase for the temperature range between 293 K and 613 K.

5.4 Conclusions

In conclusion, this work illustrates the predictions for H/D and H/T fractionation ratios and that these ratios provide an excelled metric to assess the magnitude of quantum effects predicted by different water models. We have demonstrated that there is relatively an abundance of HTO over HDO in both the liquid and vapor phases. These IFRs for various water isotopologues were computed quite efficiently using direct scaled coordinates estimator to directly determine the fractionation ratios over traditional approaches of performing computationally intensive thermodynamic integration. The NN-revPBE0-D3 model predicts the H/D ratio better in comparison to experiments and hence we predict that this NN-based water model would also be a better fit to compute H/T ratio, since there is a lack of experimental data for the H/T ratio.

6.0 Investigating Cocrystallization of the Mixture of Poly-oxacyclobutane and Water Isotopologues

6.1 Introduction

Among the polyoxyalkene (—$[(CH_2)_mO]_n$—) series, a unique member polyoxacyclobutane (POCB) exhibits unusual characteristics of cocrystallization when mixed with water to form POCB crystalline hydrate [158]. Four different crystal polymorphs (Forms I, II, III, IV) [159, 160] were reported, out of which Form I was stabilized in a crystalline form only in the presence of water via hydrogen bonding to form a crystalline hydrate [161]. With one water molecule per monomeric unit, the unit cell was shown to have the POCB chain in a planar zig-zag form, all-trans backbone with the water molecules located along channels so that they hydrogen-bond with the ether oxygen of POCB as well as with neighboring water molecules. The unit cell of POCB hydrate is shown in Fig. 18.

Recent work by Velankar et al.[158] have investigated a peculiar phase diagram of POCB water mixtures. This work have also reported on the formation of POCB crystalline hydrate that is in solid-liquid equilibrium obtained for the case of higher molecular weight POCB and a liquid-liquid equlibrium was also observed for the lower molecular weights of POCB.

Our hypothesis was to understand whether a POCB crystalline hydrate can be formed that is enriched with the heavier water isotopologues of HDO and HTO with in the hydrate framework. This process of cocrystallization lead to a low cost and energy efficient means of concentrating the heavier isotopologues present in dilute proportions. By employing path integral molecular dynamics simulations, we have investigated the feasibility of cocrystallization of POCB-water mixture enriched by HDO and HTO by determining the isotopic selectivity factor.

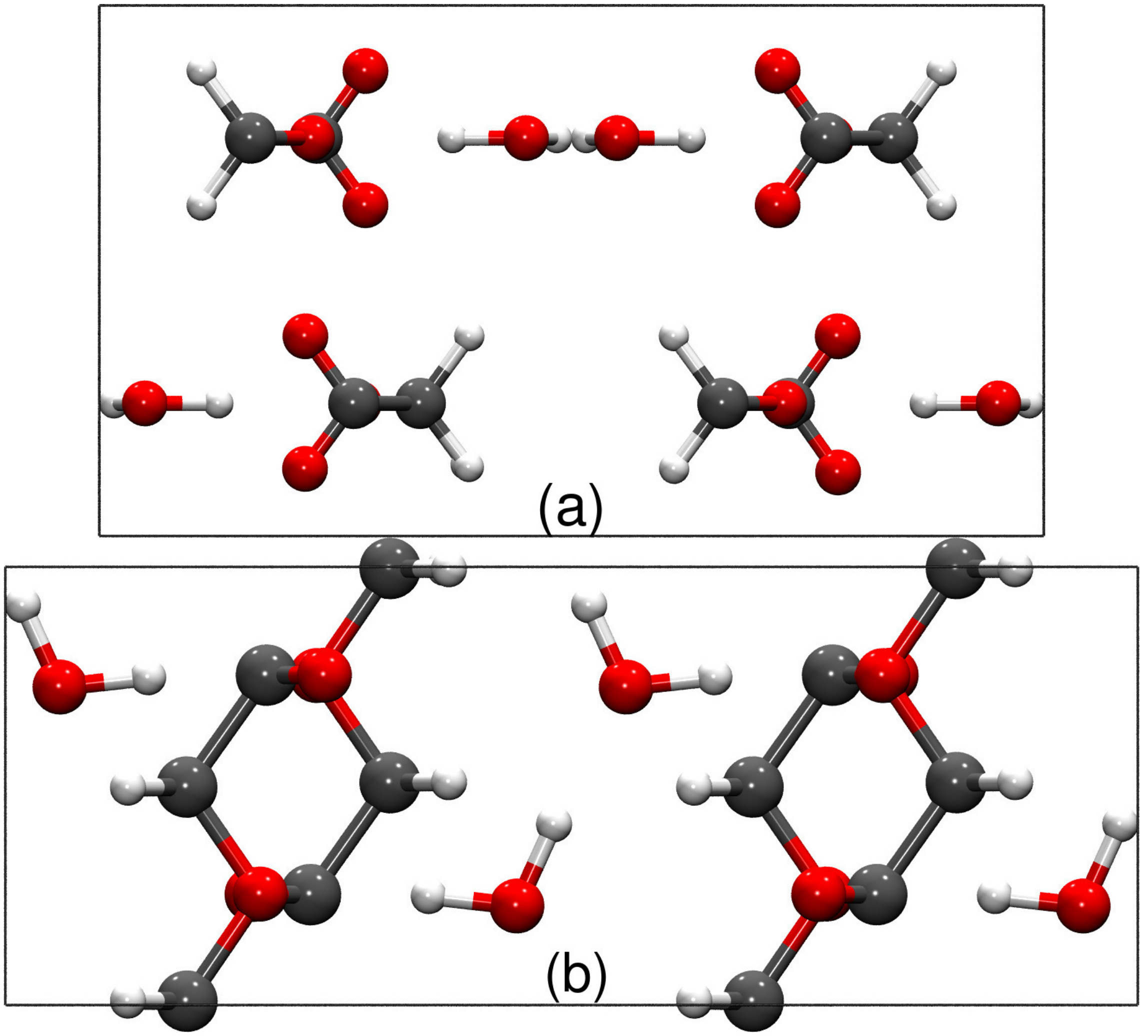

Figure 18: Unit cell configuration of Poly-oxacyclobutane (POCB) crystal.

6.2 Experimental Characterization of POCB and Water Cocrystallization

There has been extensive work covering the domain of preparing POCB polymer with higher molecular weights ranging several thousands of g/mol.[162, 163, 164] However, a very few processes were developed that involves the polymerization of lower molecular weight grades of POCB namely from the condensation polymerization of 1,3-propanediol by DuPont.[165, 166, 167] Experiments were conducted using the mixtures of lower molecular weight POCB and water in different proportions that resulted in unusual phase behavior. Interstingly, it was also reported from the experimental investigations that the POCB can readily crystallize with the adsorption of water from the moist air. The melting point of the POCB crystalline hydrate was reported to be about 310 K, which is higher the melting temperature of both the pure species POCB and water. Note that the melting temperature of the crystalline hydrate is independent of the composition of the POCB and water. Phase equilibria studies found that the POCB is not miscible with water indicating liquid-liquid equilibria under liquid conditions. However, a solid-liquid equilibrium was also established between POCB crystal hydrate with either the water-rich phase or polymer rich phase depending on the composition of water. Techniques of cloud point and melting point determination for the POCB-water mixture and hydrate crystals were performed respectively. Also differential scanning calorimetry was used to examine the hydrate crystals.[158] These experiments were performed with POCB obtained from DuPont under the commercial name of Cerenol. Most of the experiments were performed with grade H650 denoting a molecular weight was 650 g/mol.

6.3 Theory and Computational Methods

The preferential adsorption of water isotopologues HDO and HTO in the form of cocrystallization of water POCB mixture to yield a POCB crystal hydrate was investigated using path integral molecular dynamics (PIMD) framework as implemented in the i-PI package[150, 151]. Since H_2O, HDO and HTO differ only by their nuclear mass, the relative difference of their physical properties were mostly dictated by the differences in their NQEs. These NQEs can be quantified within the PIMD formalism. Every classical particle was transformed into several imaginary beads or replicas (P=32 in this case) governing imaginary time path integral framework of quantum mechanics schematically represented in the Figure 18. In this work, we have computed equilibrium isotopic fractionation ratio or selectivity factor (α) for the water isotopologues HXO {X: D,T} represented by their selective adsorption into POCB hydrate given by,

$$H_2O_{(POCB)} + HXO_{(l)} \rightleftharpoons H_2O_{(l)} + HXO_{(POCB)} \tag{6.1}$$

$$\alpha = \frac{[HXO/H_2O]_{(POCB)}}{[HXO/H_2O]_{(l)}} \tag{6.2}$$

where [HXO/H_2O] represents the relative mole fractions of HXO and H_2O for a given phase and the subscripts (l) and (POCB) represents the bulk water and POCB crystal hydrate phase respectively. For instance, the value of α greater than unity represents a dominant preference of heavier water isotopologue HXO in POCB crystal hydrate over the bulk water phase.

All the PIMD simulations were performed using the NVT ensemble over a temperature range of 240 K to 300 K the melting point of POCB crystalline hydrate (310 K) [158] to determine the temperature dependence of isotopic selectivity. These PIMD simulations were performed using a time step of 0.25 fs in conjuction with the LAMMPS package [149] to evaluate the forces and energies. Configurations for the bulk water and POCB crystalline hydrate phase were equilibrated to appropriate densities. The bulk water configuration consisted of 216 water molecules and POCB crystalline hydrate was represented by a 2 × 2 × 4 super cell (unit cell in Fig. 18) encompassing 64 water molecules as the water of crystallization. A flexible, anharmonic q-TIP4P/F water model [152] and OLSA-AA [168] for POCB were used to appropriately consider the nuclear quantum effects.

6.4 Results & Summary

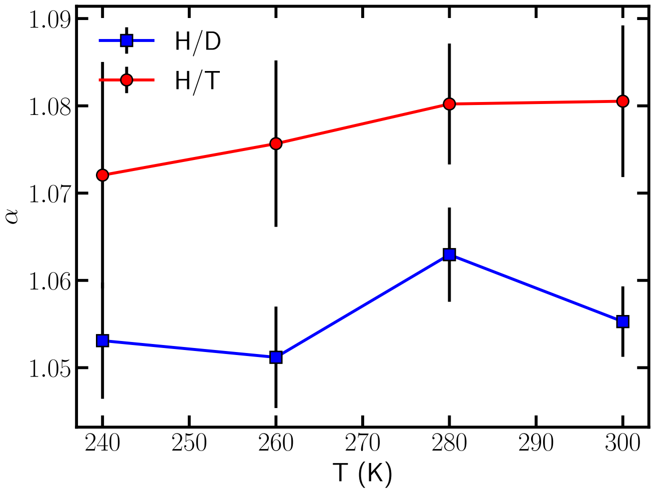

Figure 19: Isotope fractionation ratio (α) for HTO/H_2O and HDO/H_2O as a function of temperature for the cocrystallization of POCB and water isotopologues mixture. The solid line is just a guide for the eye. Standard deviations are indicated by error bars.

Results from our PIMD simulations revealed that a positive value of α was observed for HDO and HTO indicating the formation of POCB crsytalline hydrate with either HDO or HTO isotopologues as shown in Fig. 19. A maximum value of α was observed for both the HDO and HTO isotopic preference at around 280 K. It was also observed in Fig. 19 that the isotopic selectivity of HTO is more favorable over HDO towards the formation of crystal hydrate for the temperatures considered for this study. This seperation factor was attributed to the manifestation of nuclear quantum effects in the form of differences in the nuclear quantum kinetic energy for different water isotopologues.

7.0 Future Work

7.1 Investigating Cocrystallization of the Mixture of Poly-oxacyclobutane and Water Isotopologues

The work to understand the isotopic affinity of HDO and HTO for the formation of crystalline hydrate of POCB was discussed in the Chapter. 6. The above studies were performed using OPLS and q-TIP4P/F force fields to represent POCB polymer and water molecules respectively. It would be imperative to investigate the interplay of the above mentioned force fields to accurately determine the isotope fractionation ratio of cocrystallization of POCB-water mixtures. The future work under this thrust is summarized below:

- Develop a force-field based on the data obtained from DFT simulations using PBE0 function with D3 dispersion corrections. This DFT data is obtained by performing *ab-initio* Hessian matrix calculations in cartesian coordinate space using the framework of QuickFF protocols.
- Perform the path integral molecular simulations again using the newly developed DFT-based force field to determine the isotope selectivity factor for HDO and HTO.
- Compare and contrast the relevant results obtained from the native force-field of using OPLS and q-TIP4P/F with the DFT-based force field.

7.2 Addressing Thermodynamic Stability and Temperature Dependence of Proton Diffusivity

Having established the characterization of graphane functionalized with hydroxyl (Chapters. 2 and 3) and amine groups (Chapter 4) for efficient and facile proton transport, it would be an interesting step to investigate the thermodynamic stability and also the temperature dependece of proton diffusivities for the above said materials. The future work under this thrust is summarized below:

- Perform free calculations to understand the thermodynamic stability associated with the formation of defects in the form of (a) creating of water molecule from the center of exccess or protonated hydroxy group of graphanol and (b) in the form of creating an ammonia molecule from the center of excess charge represented as protonated amine group on graphamine.
- Perform AIMD simulations to compute the proton diffusivities at different temperatures with one excess proton for graphanol and graphamine.

7.3 Molecular Recognition of Water in Porous Coordination Polymer

To shed light on molecular recognition of water adsorption with in a porous framework, we have focused on calcium squarate, $[Ca(C_4O_4)(H_2O)]\cdot 1.5H_2O_n$, a family of porous coordination polymers that can encapsulate water molecules with in the cavities. Calcium squarate (CaSq) was also reported to be synthesized according to Robl et al.[169] It was reported from the experimental investigations that a shrinkage of lattice volume was observed with the loading of water molecules in the 3D cavities established by the framework. A gradual loading of 0.5, 1.0 and 1.5 molecules of water (guest water molecules) per Ca ion in the unit cell induces incremental shrinkage of lattice as observed by the variation of lattice parameters with respect to an unoccupied configuration of CaSq. Our current workflow is to perform structural relaxation calculations and ab-initio molecular dynamics (MD) simulations in the NpT ensemble for CaSq with an empty framework and also with different loading amounts of guest water molecules to determine the lattice parameters for the temperature of 303 K and 1.0 bar. Our priliminary results obtained from the simulations performed for the unoccupied lattice configuration and with a maximum occupied configuration with guest molecules (i.e., 1.5 water molecules per Ca ion) revealed a shrinkage of 0.3% for the lattice parameter a. This lattice shrinkage can be attributed to the formation of hydrogen bonding between the H_2O molecule that are inherent part of the framework and the guest water molecules. The future work is summarized below:

- Perform structural relaxations for the configurations of 0.5 and 1.0 loading of guest water molecules.

- Determination of lattice parameter from AIMD-NpT simulations for the above said loadings.

- Publish the manuscript that provides insights into the lattice shrinkage, hydrogen bond dynamics of water adsorption with in CaSq framework from the perspective of *ab-initio* simulations.

7.4 Facile Separation of Medically Indispensable $^{18}O_2$ from $^{16}O_2$ Using Carbon Nanotubes

Isotopic selectivity of molecular oxygen $^{18}O_2$ from $^{16}O_2$ was observed from our force-field based path integral molecular simulations of 1 nm diameter isolated single walled carbon nanotube (SWCNT) of chiral index (7,8). This selectivity was achieved for the (7,8) SWCNT adsorbed with the molecular oxygen loading of 7.0 mmol/g. Given the observed isotopic selection factor for (7,8) SWCNT, we would like to investigate the dependence of $^{18}O_2$ isotope selectivity for different diamter of SWCNT and with appropriate adsorbent loadings. The future work is summarized below:

- Perform GCMC simulations using RASPA to achieve appropriate adsorbate loading of $^{16}O_2$ with different SWCNT chiral index configurations of (4,4), (5,5), (7,7) and (10,10).

- Dependence of isotope selectivity for $^{18}O_2$ would be investigated for the above chiral indices.

- Investigation of isotope selecitivity factor for zero loading configurations of SWCNTs with indices (4,4), (5,5), (7,7) and (10,10) would also be performed.

7.5 Unraveling the Affinities of Tritiated Water for Polymeric Materials

The hypothesis of this work is to investigate the affinity of strongly binding tritiated water to a polymeric material. The analysis for the affinity of tritiated water is based on the Gibbs free energy of the following equilibrium,

$$H_2O_{(bulk)} + HTO_{(polymer)} \leftrightharpoons H_2O_{(polymer)} + HTO_{(bulk)} \tag{7.1}$$

where, the reactant states are the configurations of HTO bound to the polymer denoted with "$HTO_{(polymer)}$" along with the bulk water phase "$H_2O_{(bulk)}$". On the products side, the tritiated water bound to polymer is now replaced with normal water "$H_2O_{(polymer)}$" and the tritiated water is displaced to the bulk phase "$HTO_{(bulk)}$". The above reaction measures the affinity for the tritiated water to be associated with the polymer in the form of free energy change of hydrogen bonding strength. It also signifies the importance of displacing a HTO molecule hydrogen bonded with the polymer to the bulk aqueous phase and replacing the same with a light water H_2O taken from the bulk aqueous phase. The free energy change for the above reaction determines whether the HTO prefers to be bound more strongly to the polymer compared to the bulk aqueous phase. The future work under this thrust is summarized below:

- Perform isotope selectivity studies at different temperatures for poly-vinyl acetate.
- Refine the exisiting manuscript with updated results section.

8.0 Summary of Publications from Ph.D.

- Bagusetty, A., Choudhury, P., Saidi, W. A., Derksen, B., Gatto, E., & Johnson, J. K. (2017). Facile anhydrous proton transport on hydroxyl functionalized graphane. Phys. Rev. Lett., 118(18), 186101.
- Bagusetty, A., & Johnson, J. K. (2019). Unraveling Anhydrous Proton Conduction in Hydroxygraphane. J. Phys. Chem. Lett., 10(3), 518-523.
- Bagusetty, A., Livingston, J., & Johnson, J. K. (2018). Graphamine: Amine-Functionalized Graphane for Intrinsic Anhydrous Proton Conduction. J. Phys. Chem. C., 123(3), 1566-1571.
- Bagusetty, A., Cheng, B., Ceriotti, M., Xiao, X. & Johnson, J.K. (2019) Role of nuclear quantum effects on the isotope fractionationation of water isotopologues. J. Chem. Phys., *In preparation*
- Ewing, C. S., Bagusetty, A., Patriarca, E. G., Lambrecht, D. S., Veser, G., & Johnson, J. K. (2016). Impact of support interactions for single-atom molybdenum catalysts on amorphous silica. Ind. Eng. Chem. Res., 55(48), 12350-12357.

Works from 1-4 were included as chapter 1-4 in this dissertation.

Appendix A Facile Anhydrous Proton Transport on Hydroxyl Functionalized Graphane

A.1 Molecular Dynamics Calculations

Ab initio molecular dynamics calculations were performed to estimate the self-diffusivity of protons as a function of temperature. Constant temperature runs of 1 ps were initially performed to equilibrate the system. The temperature was scaled every 25 time steps to the target value during the equilibration period. The ending configuration and velocities were used to run AIMD *NVE* simulations to avoid thermostat errors that were noted in test runs using the Nosé thermostat [170]. The simulations were run for an additional 20 ps for data collection at nominal temperatures of 400, 600, and 800 K. The proton self-diffusivity was calculated using the Einstein expression, $D = \lim_{t\to\infty} \mathrm{MSD}/(2t)$, where D is the self-diffusivity, t is the time, and MSD is the mean square displacement in the direction of the 1-D OH chain. At least 100 independent simulations were performed at each temperature for statistical accuracy.

A.2 Energy Barrier Calculations

VASP calculations were performed with projector augmented-wave pseudopotentials [81]. Vanderbilt ultrasoft pseudopotentials [171] were used for QE calculations. The climbing-image nudged elastic band (cNEB) technique [18] was used to find the energy barrier height related to the proton hopping process. The replicas were allowed to converge until the forces were less than 0.025 eV/Å. The end points representing initial and final states along the proton transport (PT) process were relaxed to a force convergence of 5×10^{-3} eV/Å before performing cNEB calculations. We have optimized the transition states and metastable intermediate state to high accuracy (5×10^{-4} eV/Å) followed by vibrational frequency analysis; each of the transition states has a single mode with an imaginary frequency. This strict relaxation tolerance was adopted because the PT barrier was found to be so low. Vibrational frequency analysis confirmed that the metastable intermediate state was a true minimum (all modes had real frequencies). Test calculations using the PW91 [172] exchange-correlation functional gave similar results.

A.3 Rate Constants for Proton Transport

The classical barrier for PT obtained from cNEB was used to estimate rate constants for the PT process as a function of temperature. Plots of the rate constants computed from classical harmonic transition state theory (TST), quasi-classical harmonic [23], and semi-classical TST approximations [24] as a function of temperature are given in Fig. 20.

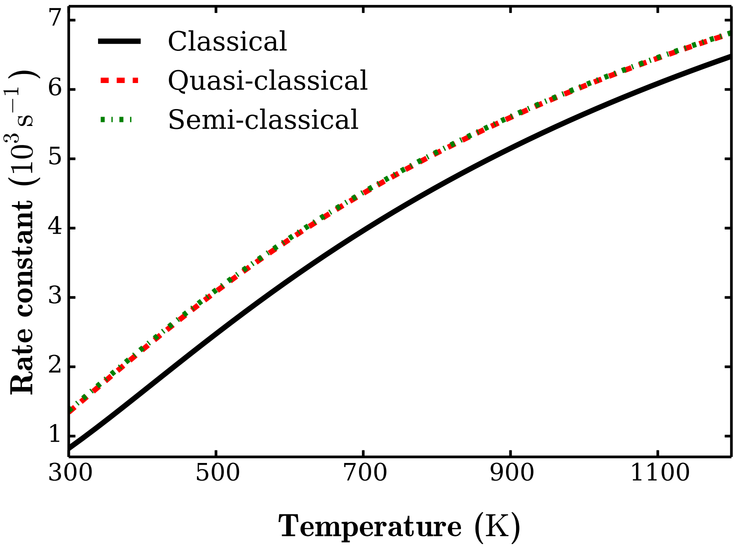

Figure 20: Rate constants for proton transport computed from classical, quasi-classical, and semi-classical transition state theory approximations for temperatures ranging from 300 to 1200 K.

A.4 Finite-size Effects

We have constructed a larger hydroxylated graphane supercell to investigate finite-size effects. The larger supercell contains 70 C atoms and seven hydroxyl groups forming a periodic 1-D chain of hydrogen bonds, shown in Fig. 21. The supercell lattice parameters for the four and seven hydroxyl group systems are given in Table 2.

Table 2: Lattice parameters for the supercells containing 4 and 7 hydroxyl groups.

System	a (Å)	b (Å)	c (Å)	α (°)	β (°)	γ (°)	C	H	O
4-OH	9.856	7.392	20.000	90	90	120	24	25	4
7-OH	17.534	12.524	40.000	90	90	120	70	71	7

A.5 Lattice Monte Carlo Simulations

A lattice Monte Carlo (LMC) model was constructed in order to verify that the Fickian diffusion profile observed from the AIMD simulations is not an artifact of system size or short simulation time. The model incorporates the observed PT mechanism by requiring that a proton hop only happen if a proton aligned perpendicular to the OH chain can rotate, such that the the excess proton is shuttled along the OH chain. The LMC model consists of a 3×N grid, with N particles on the center row representing the protons associated with OH groups aligned along the 1-D chain. Excess protons can be randomly placed in the two off-center rows of the grid. This setup is shown in Fig. 22 for a grid size of $N = 4$ with one excess proton and is analogous to configuration observed from AIMD simulations for the 4 OH group system, also shown in that figure.

The concerted proton hopping mechanism cannot be directly mapped into the LMC model, since a slightly different mechanism was used to simulate a move in the LMC model. The LMC algorithm is as follows: (1) a lattice size N is selected and a number of excess protons $M \leq N$ are randomly populated either above or below the center lattice, subject to

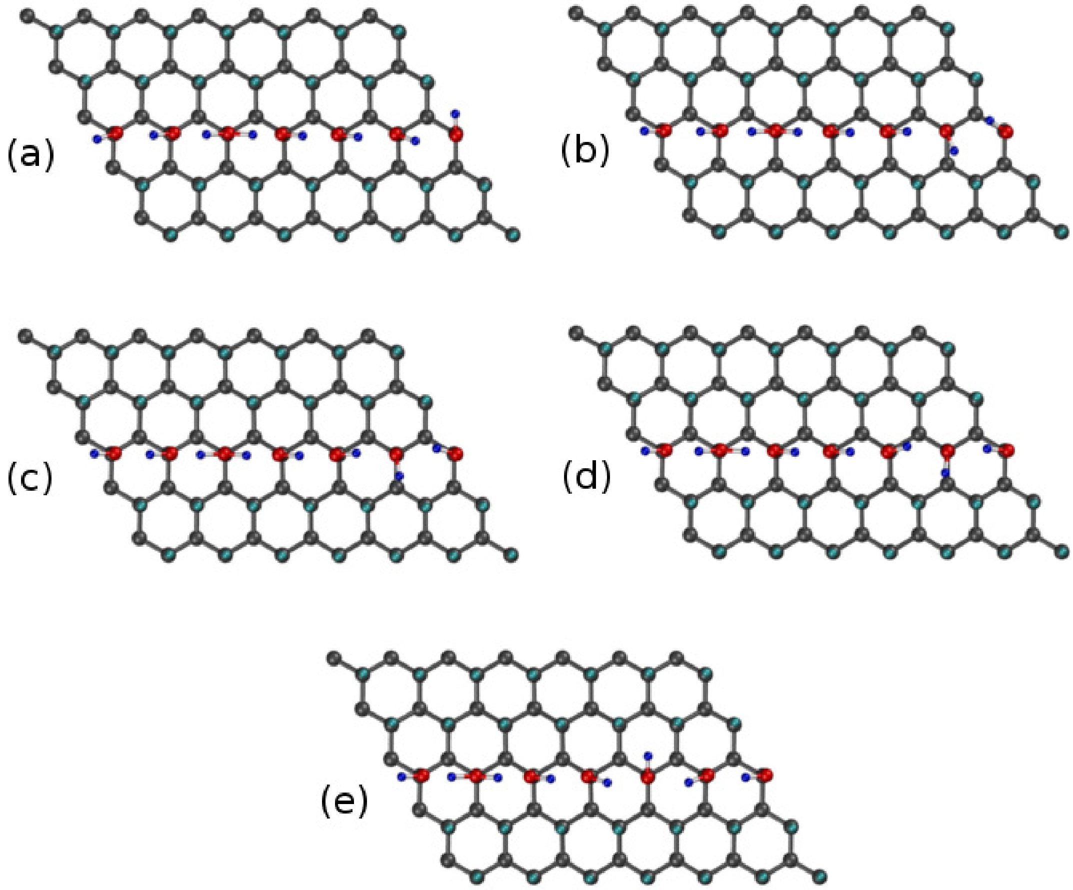

Figure 21: Atomic configurations computed from cNEB for the 7-OH group system for the (a) initial state, (b) first transition state, (c) metastable intermediate, (d) second transition state, and (e) final state.

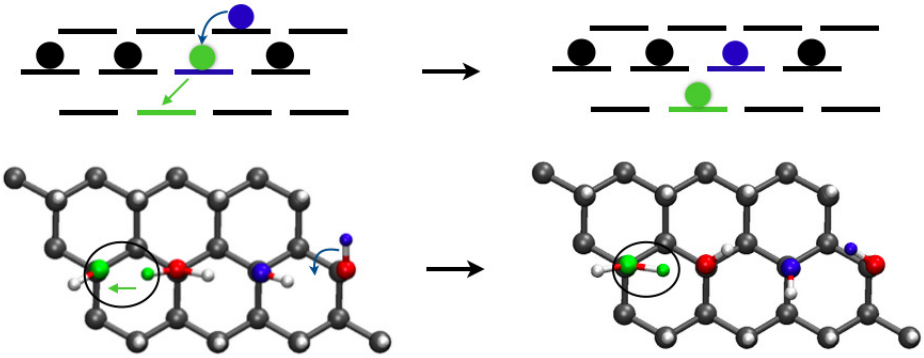

Figure 22: (Top panel) Representative configuration for the LMC model. The off-center particle (blue) initiates a move to a center row location (blue underscore). The center particle (green) displaces to a target off-center location (green underscore). (Bottom panel) Analogous configurations to the LMC model as observed from AIMD simulations. Curved blue arrow indicates the rotation of the hydroxyl group and the green arrow represents the shuttle of proton. The final configurations are shown to the right.

the constraint that the adjacent sites in that row are empty and the site directly opposite (below or above the center) is also empty; (2) one of the off-center particles (representing OH groups aligned perpendicular to the 1-D chain) is randomly selected to initiate the move; (3) the selected particle is randomly assigned a direction (left or right) for the attempted move, which mimics the rotation of a hydroxyl group from an orientation perpendicular to the 1-D chain to an orientation aligned with the chain; (4) if the lattice site on the opposite side of the 1-D chain and in the direction of travel (left or right) is empty then the move is deemed feasible, and a particle in the center row in the direction of travel is displaced to that empty site (as illustrated in Fig. 22), else the move is rejected. This last step can be interpreted as the rotation of an OH group aligned with the 1-D chain to a position perpendicular to the chain. Steps (2)-(4) are repeated a specified number of times.

A LMC system was constructed with $N = 4000$ OH groups and one excess proton to test system size effects. Simulations were run for 10^6 attempted moves, averaged over 104 independent runs. Results from these simulations are plotted in Fig. 23, where one can see that the MSD divided by time is essentially a constant, indicating Fickian diffusion. Simulations involving smaller systems employing AIMD and finite size systems with longer time scales employing LMC techniques showed qualitatively similar results as seen in Fig. 23. Lattice Monte Carlo simulations were also carried out for a system of $N = 8000$ OH groups and $M = 4000$ protons. A total of eight independent simulations, each carried out for 10^6 trial moves, were performed. The MSD divided by the square root of the time is plotted in Fig. 24, from which one can see that MSD/$t^{1/2}$ is essentially constant, confirming single-file diffusion.

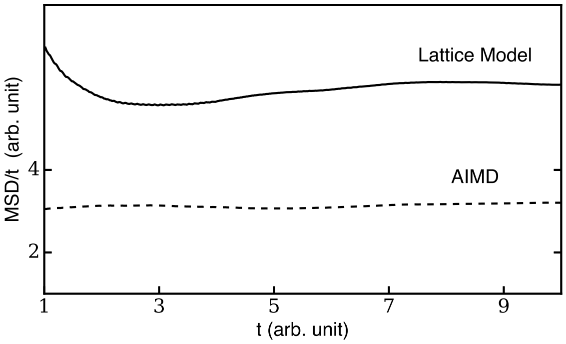

Figure 23: Evidence of Fickian diffusion, as seen by a plot of MSD/t being a constant computed from AIMD simulations at 800 K (dashed) and LMC model calculations (solid). The LMC model results are in arbitrary units and have been scaled to facilitate plotting on the same graph.

A.6 Analysis

A.6.1 Exchange-Correlation Functional Test

The effect of the choice of the exchange-correlation functional was tested by comparing results computed from the Perdew-Burke-Ernzerhof (PBE) [17] form of the generalized gradient approximation with calculations using the PW91 functional [172, 173], which has been shown to give good results for water [174]. The proton hopping minimum energy pathway for

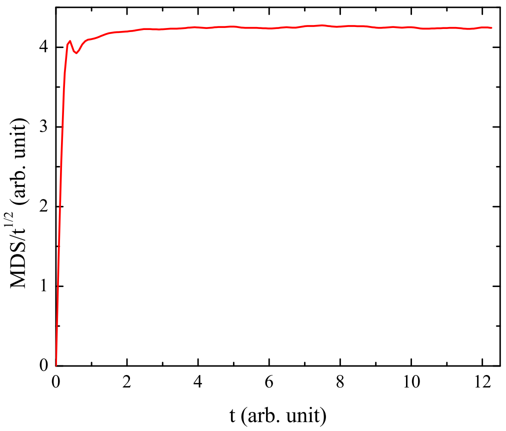

Figure 24: Evidence of single-file diffusion, as seen by a plot of MSD$/t^{1/2}$ being a constant, computed from the LMC model with 8000 OH groups and 4000 protons. The LMC model results are in arbitrary units.

the 4OH system computed from each of these functionals is plotted in Fig. 25. The results are in remarkably good agreement, giving us confidence that the PBE results are physically reasonable.

A.6.2 Hydrogen Bond Analysis

The distances between the oxygen atoms of the hydroxyl groups sharing the excess proton in the PT process along the minimum energy pathway were measured for both the 4 and 7 OH systems. The excess proton is identified as the one that hops from one O atom to the neighboring O atom. The results are plotted in Fig. 26. The data in the figure indicate that the O–O spacing is close to optimial for PT, because the spacing decreases only slightly when the PT event takes place.

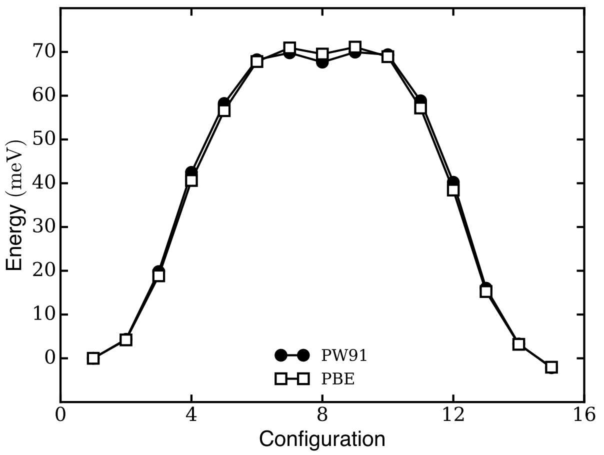

Figure 25: Comparison of relative single point energies computed from the PBE and PW91 exchange-correlation functionals for the 4 OH group system. The configurations were taken from the PBE cNEB calcualtions.

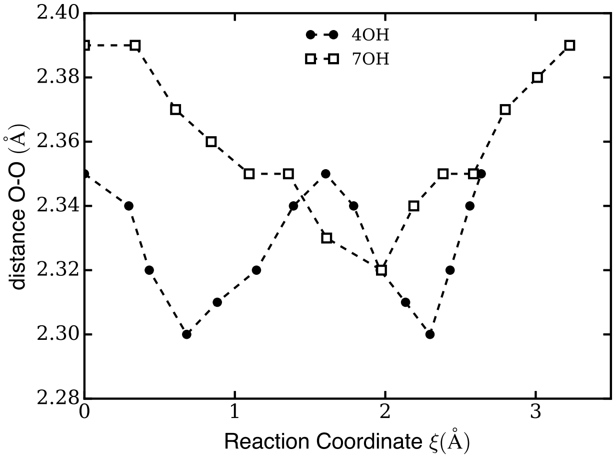

Figure 26: Plot of the O–O distances of the OH groups sharing the excess proton along the minimum energy pathway for 4 and 7 OH group systems.

A.6.3 Charge Delocalization

The hypothesis of indistinguishable protons participating in the PT process was tested by computing the partial atomic charges from the Density Derived Electrostatic and Chemical (DDEC6) charge analysis approach [25, 90]. This analysis was performed for various configurations on the minimum energy pathway describing the PT event as computed from the climbing image nudged elastic band calculations. The electron densities for these configurations were computed from both PBE and Hartree-Fock as implemented in VASP (v5.4.1). The Hartree-Fock calculations gave similar results to PBE, confirming that the charge delocalization is not due to density functional theory self-interaction error. Charges for the 7 OH system were also computed to estimate finite size effects on the charges. The partial atomic charges computed from PBE for the 4 OH and 7 OH systems are reported in Tables 3 and 4, respectively. The DDEC6 charges from Hartree-Fock calculations are shown in Table 5.

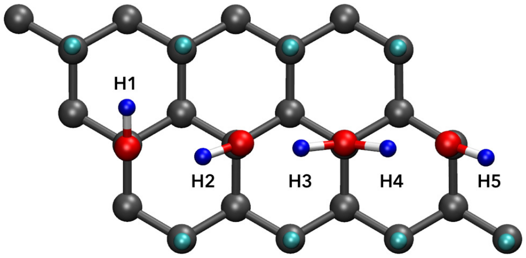

Figure 27: Atom labels corresponding to the Atom IDs in Tables 3 and 5.

A.7 Morphological Defects

The most common defect for the 1-D system studied in this work is expected to be a missing hydroxyl group. We have estimated the proton diffusion barrier for a system having a hydroxyl group vacancy. We removed a single hydroxyl group from the system shown in Fig. 1 and replaced the missing OH group with a hydrogen atom to saturate the carbon atom associated with vacancy (see Fig. 28). The barrier to proton hopping from the

Table 3: Net partial charges computed from DDEC6 for protons participating in the hydrogen bonded network at different configurations on the diffusion pathway in a 4 OH system. Atom IDs are defined in Fig. 27.

Atom ID	Initial State	TS 1	Local Min.	TS 2	Final State
H1	0.3772	0.4148	0.4174	0.4172	0.4125
H2	0.4104	0.4163	0.4156	0.4134	0.3781
H3	0.4125	0.3814	0.3815	0.3803	0.3695
H4	0.3782	0.3680	0.3673	0.3677	0.3777
H5	0.3687	0.3817	0.3813	0.3821	0.4113

Table 4: Net partial charges computed from DDEC6 for protons participating in the hydrogen bonded network at different configurations on the diffusion pathway in a 7 OH system. The atom IDs correspond to numbering the H atoms bound to oxygens in Fig. 21 from left to right.

Atom ID	Initial State	TS 1	Local Min.	TS 2	Final State
H1	0.3564	0.3741	0.3788	0.3876	0.3926
H2	0.3836	0.3922	0.3935	0.4041	0.4030
H3	0.4036	0.4044	0.4030	0.4030	0.4040
H4	0.3780	0.3887	0.3873	0.3800	0.3568
H5	0.3527	0.3598	0.3565	0.3560	0.3605
H6	0.3608	0.3543	0.3565	0.3564	0.3537
H7	0.4027	0.3605	0.3556	0.3574	0.3784
H8	0.4036	0.4048	0.4036	0.3954	0.3851

Table 5: Net partial charges computed from DDEC6 using electon densities computed from Hartree-Fock theory for protons participating in the hydrogen bonded network at different configurations on the diffusion pathway in a 4 OH system. Atom IDs are defined in Fig. 27.

Atom ID	Initial State	TS 1	Local Min.	TS 2	Final State
H1	0.4222	0.4841	0.4853	0.4886	0.4827
H2	0.4798	0.4889	0.4838	0.4802	0.4265
H3	0.4796	0.4335	0.4260	0.4235	0.3950
H4	0.4242	0.3962	0.3960	0.3971	0.4264
H5	0.3970	0.4266	0.4291	0.4342	0.4823

initial state to the final state shown in Fig. 28 was estimated by manually constructing the transition state by placing the diffusing proton mid-way between the neighboring OH groups and relaxing all the atoms in the system. Hence, we approximated the transition state barrier by performing a series of geometry relaxations on transition state configurations estimated from interpolated pathways between initial and final states. The configuration having the lowest energy is shown in Fig. 28 (c) and (d). The barrier is estimated to be about 4.4 eV, which clearly show that proton transport is effectively blocked by the presence of a single hydroxyl group vacancy.

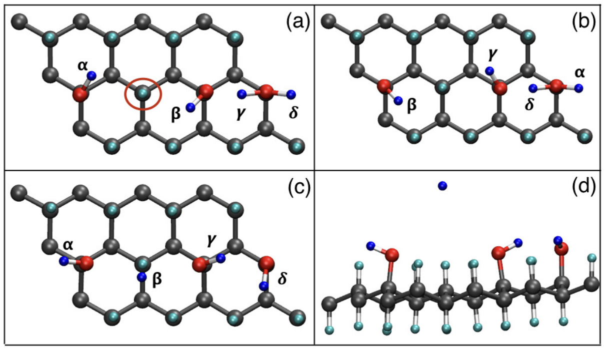

Figure 28: Atomic configurations for a proton hopping event for a system containing a hydroxyl group vacancy defect. (a) Initial state, shown with the hydroxyl group vacancy defect, capped with a hydrogen atom, identified with a red circle, (b) final state, (c) transition state, and (d) Side-on view of the transition state. All the hydrogen atoms participating the hop are tagged with Greek letters ($\alpha, \beta, \gamma, \delta$) for identification and tracking (carbons in gray, oxygens in red, hydrogens bound to oxygens in dark blue, hydrogens bound to carbon in light blue).

Appendix B Unraveling Anhydrous Proton Conduction in Hydroxygraphane

B.1 Computational Methodology

The AIMD simulations were performed using Γ point k-space sampling with a time step of 0.25 fs on a $2 \times 2 \times 1$ supercell of the configuration shown in Figure 1 to reduce finite-size effects. The supercell used for AIMD simulations is shown in Figure 29. The supercell, comprised of 241 atoms, included an excess proton such that the entire system had a net charge of +1 e. Each run consisted of a canonical ensemble (NVT) run, wherein the temperature of the system was equilibrated to 800 K using a Nosé thermostat[170], followed by a microcanonical (NVE) ensemble production run for at least 22 ps.

The mean squared displacement (MSD) was computed from each of the ten independent AIMD simulations. Multiple time origins, with a time between origins of 200 fs, were used to improve the statistics and the MSDs for each run were averaged over x and y directions along the plane of hydroxygraphane. The diffusion coefficient was estimated from the Einstein relation ($D = \lim_{t\to\infty}\langle|r(t) - r(0)|^2\rangle/(2dt)$, where $d = 2$ is the dimensionality of the system) by fitting a line to the linear regions of the MSD verses time plots for each of the ten independent runs. An average diffusion coefficient and a standard deviation were computed from the ten values of D.

B.2 DDEC6 Partial Atomic Charges

The partial charges on the hydrogen atoms participating in the proton conduction process were computed for the system shown in Figure 30 from the Density Derived Electrostatic and Chemical (DDEC6) charge analysis approach.[25, 90] Table 6 presents the statistics of partial atomic charges and the actual charges of the protons are given in Table 7. The net atomic DDEC6 charges reported were computed by analyzing the charge densities obtained from VASP.

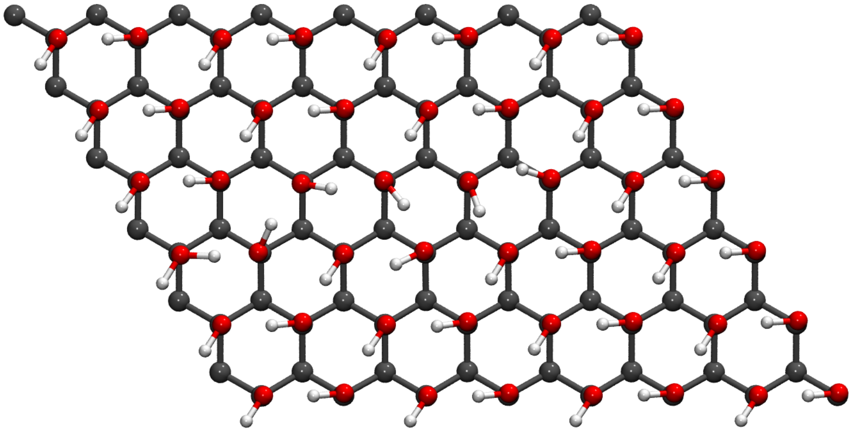

Figure 29: Supercell of protonated hydroxygraphane used for AIMD simulations.

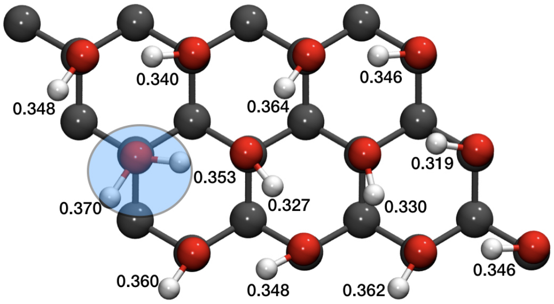

Figure 30: Configuration of protonated hydroxygraphane with net DDEC6 atomic partial charges on the protons bound to hydroxyl groups. The center of excess charge is shown by the circle.

Table 6: Statistics (mean, maximum, minimum and standard deviation) of DDEC6 atomic partial charges of protonated hydroxygraphane in comparison to the protonated 1-D hydroxylated graphane.[76]

Quantity	Hydroxygraphane	1-D hydroxylated graphane
$\overline{q}$	0.347	0.380
q_{max}	0.37	0.404
q_{min}	0.32	0.3527
q_{σ}	0.014	0.02

B.3 Phonon Properties

The spectrum of phonon bands is shown in Figure 31 for a 3×3 supercell configuration (total number of atoms = 90) of the primitive cell of hydroxygraphane shown in Figure 6 of Chapter 3.

B.4 Elastic Properties

The elastic properties of hydroxygraphane were computed from DFT under induced deformations within harmonic strain limits ($\epsilon < \pm\ 2\%$). The rectangular supercell used to determine elastic properties is shown in Figure 38. With an application of uniaxial and equi-biaxial strain to the lattice vectors, the in-plane 2-D Young's modulus, (Y) and Poisson's ratio, (ν), were estimated as a function of elastic constants C_{11} and C_{12} related by the expressions,

$$Y = \frac{C_{11}^2 - C_{12}^2}{C_{11}} \tag{B.1}$$

$$\nu = \frac{C_{12}}{C_{11}}. \tag{B.2}$$

Table 7: DDEC6 partial charges for protons of hydroxyl groups (coordinates in Cartesian format) of the protonated hydroxygraphane shown in Figure 30.

x	y	z	q
6.100916	3.933451	11.313620	0.319882
-1.363149	2.699204	11.244620	0.369235
2.220519	1.070927	11.296000	0.348896
4.665542	2.761095	11.324020	0.330375
-0.398904	5.920192	11.325260	0.339953
4.770224	5.933185	11.312980	0.346656
2.630429	5.201999	11.368980	0.364803
5.233040	0.632261	11.326840	0.362692
-2.551866	5.155654	11.306020	0.348524
7.366636	1.528383	11.334120	0.346649
0.237644	3.507186	11.282680	0.353881
-0.011377	0.624431	11.263460	0.359867
2.354982	2.959652	11.312660	0.326642

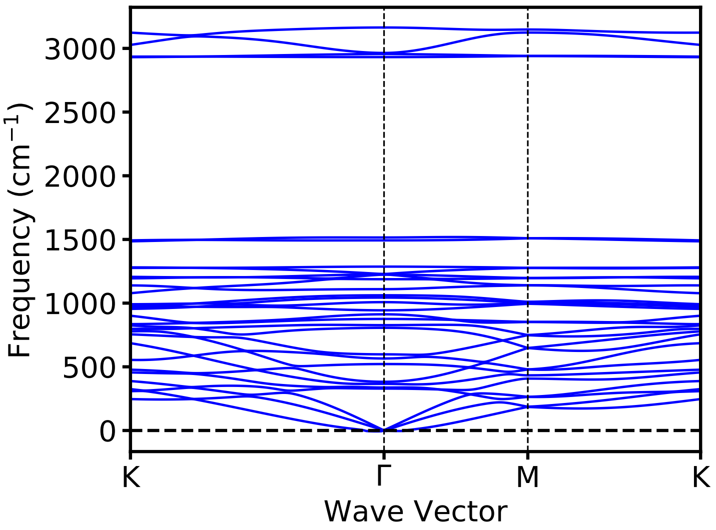

Figure 31: Phonon dispersion spectrum for hydroxygraphane computed using the harmonic approximation within PBE.

The elastic strain energy (E_s) per unit area was estimated from the difference between the electronic energy of the configuration under strain ($\epsilon \neq 0$) and equilibrium ($\epsilon = 0$). These elastic strain energies (E_s) were determined from geometry relaxation of the atoms under deformation; the data were fitted to a parabolic expression to determine elastic constants. For a system under uniaxial deformation, strain was applied only along the x-direction ($\epsilon_{yy} = 0$) and the calculated strain energy was fitted to a parabolic expression, $E_s(\epsilon_{xx}) = C_{11}\epsilon_{xx}^2/2$. Similarly, equi-biaxial ($\epsilon_{xx} = \epsilon_{yy}$) strain energy was fitted to the expression $E_s(\epsilon_{xx}) = (C_{11} + C_{12})\epsilon_{xx}^2$. The fitted elastic constants were $C_{11} = 254.31$ J/m^2, $C_{12} = 27.27$ J/m^2. Note that these are 2-D elastic constants, hence the units are J/m^2 rather than J/m^3, as would be the case for 3-D materials. A plot of the fit is shown in Figure 39. A set of 20 lattice parameters were obtained by perturbing the equilibrium lattice parameters to reflect compression and tension. The atomic positions were then scaled to accommodate the new lattice parameters and the atoms were allowed to fully relax until the energy convergence tolerance of 10^{-8} eV.

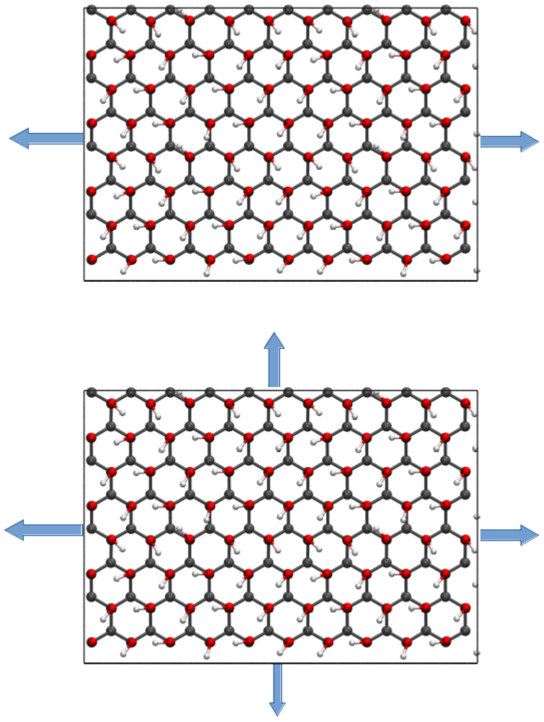

Figure 32: Equilibrium supercell used to compute elastic properties is shown under (top) uniaxial strain, (bottom) equi-biaxial strain.

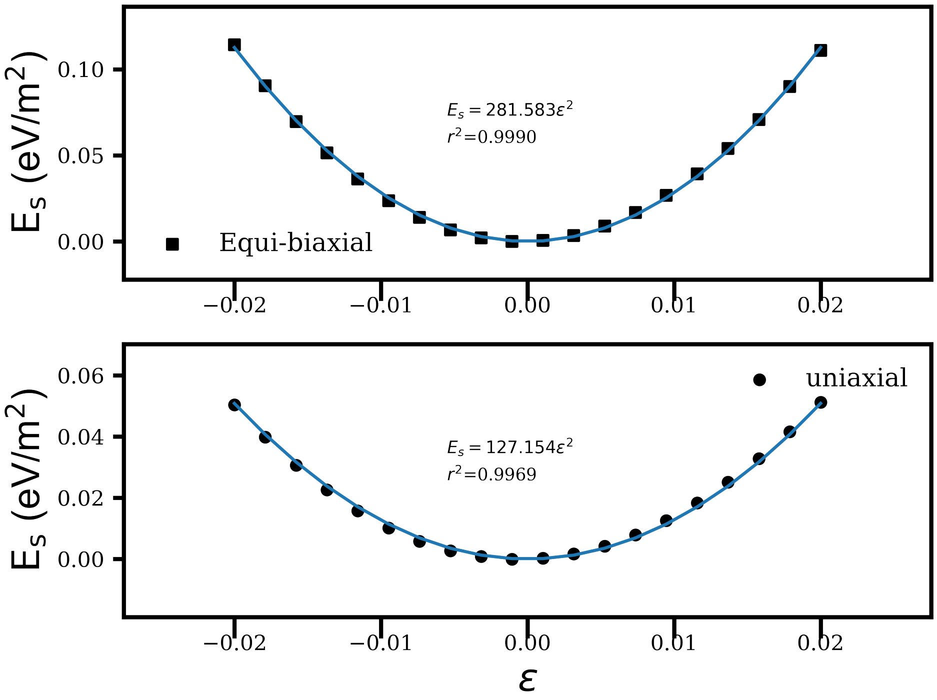

Figure 33: Parabolic fit of strain energy per unit area under uniaxial and equi-biaxial strain loading with in the limits of ± 2% for hydroxygraphane in configuration shown in Figure 38.

B.5 Atomic Coordinates for Graphanol

Fractional representation of positions in VASP format for hydroxygraphane in Fig. 1. of main text.

```
GOH
   1.00000000000000
    10.3651176752712431    0.0000000000000000    0.0000000000000000
    -3.8869191282267161    6.7323414150000005    0.0000000000000000
     0.0000000000000000    0.0000000000000000   20.0000000000000000
   C    O    H
    24    12    24
Direct
  0.3792507164788759  0.2150116916096672  0.4790320906045538
  0.2955072449047660  0.3252245491111579  0.4547671725778223
  0.3792460551398376  0.5483399345503835  0.4790411399335247
  0.2955030690847769  0.6585578133145953  0.4547751465095998
  0.3792450998724700  0.8816770929189540  0.4790473181800216
  0.2954984963769610  0.9918851073372994  0.4547790209940072
  0.6292462853018826  0.2119888704610970  0.4790266427524623
  0.5454989998873858  0.3234551264459297  0.4547713639932098
  0.6292527863894348  0.5453269763590095  0.4790327274412142
  0.5454946248110213  0.6567811567597820  0.4547813891172962
  0.6292442679491165  0.8786541570345014  0.4790385005029515
  0.5454916282395355  0.9901117784692494  0.4547792385606511
  0.8792453392605699  0.2149898843208575  0.4790048659178773
  0.7954897559372394  0.3251944171489057  0.4547520373965769
  0.8792485015586791  0.5483236667546920  0.4790141852366289
  0.7954903067388230  0.6585300292622956  0.4547593260147241
  0.8792421551444159  0.8816588579209000  0.4790179079585860
  0.7954824921920028  0.9918547018984870  0.4547568323591262
  0.1292524610390123  0.2120225108093816  0.4790154208342526
  0.0455024975226549  0.3234758553315547  0.4547505023225558
  0.1292445201449964  0.5453447577202690  0.4790222379290814
  0.0455023446872396  0.6568095703095792  0.4547613198823470
  0.1292458330416058  0.8786801201192062  0.4790351710648837
  0.0455008908615603  0.9901378717718454  0.4547618869124305
  0.3847433591339376  0.5562326484920042  0.5507019056135376
  0.6347769126001465  0.5447794749794829  0.5506978927250233
  0.8847553377274346  0.5561719700162551  0.5506776485557086
  0.1347359688999922  0.5447985363173408  0.5506851295924129
  0.1347335939325067  0.8781575019694022  0.5506963940664330
  0.8847570942981894  0.8895394138031458  0.5506760011082328
  0.6347637537559074  0.8781137562509285  0.5507021306331106
  0.3847389821713901  0.8895479685419041  0.5507076406263814
  0.1347636414938087  0.2115171367232029  0.5506789737601686
  0.8847523531222247  0.2228583110970639  0.5506647267060079
  0.6347513863496504  0.2114430083211227  0.5506915341992961
  0.3847382382997985  0.2229009434464586  0.5506959667039347
  0.5447822160278437  0.6554850218901273  0.3995077682472400
  0.7947719773589801  0.6588752998648914  0.3994854232165507
  0.0448173086191046  0.6555799027882423  0.3994871415959929
  0.2948454691686992  0.6589541809858316  0.3995002396799179
  0.0448120061326918  0.9888411934350306  0.3994878245293470
```

```
0.7947185971759594  0.9921383779466620  0.3994818450463025
0.5447637654130237  0.9887875180647171  0.3995046717259174
0.2948050286604451  0.9922228578980965  0.3995045196592619
0.2948428816566245  0.3256191849638153  0.3994906633752026
0.5447997212292095  0.3221801972183563  0.3994957320922050
0.7947653756207715  0.3255414133127753  0.3994757849368973
0.0448357159194306  0.3222382135601236  0.3994754380339630
0.7879437094456712  0.5453208626664405  0.5648617789944219
0.0379567051697393  0.4264836927742168  0.5648618593784426
0.2880088923732177  0.2123547331970839  0.5648549537951364
0.5380188740498560  0.4264582109717865  0.5648802572573879
0.2879714359901265  0.8788683396077296  0.5648817522644438
0.7879490152325660  0.8787183712499494  0.5648570744148479
0.5380012992224846  0.7597874976209332  0.5648854036994588
0.5379864725100917  0.0931020134424184  0.5648702031208674
0.0379623587177838  0.7598404185564294  0.5648728080081620
0.7879517469866288  0.2120594123049984  0.5648466783641682
0.2879737506987571  0.5455390754539268  0.5648750623644619
0.0380184504237384  0.0931703866677383  0.5648654269127545
```

Appendix C Graphamine: Amine Functionalized Graphane for Intrinsic Anhydrous Proton Conduction

C.1 Bonding & Lattice Parameters

The optimal lattice constant (a_0=1.545) was determined by fitting first-principles $E(V)$ energy(volume) data to the third-order Birch-Murnaghan equation of state shown in Figure 34. A list of all appropriate bonding parameters for the graphamine is listed in Table 8.

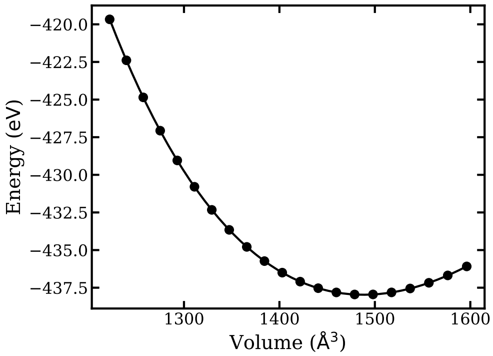

Figure 34: Total energy as a function of volume for the fit of the Birch-Murnaghan equation of state.

Table 8: Average bond lengths (Å) for the topology of graphamine

Bond type	Bond length
C—C	1.62
C—H	1.10
C—N	1.48
N—H	1.02

C.2 DDEC6 Partial Atomic Charges

The indistinguishable nature of the protons of the amine groups participating in the PC process (for the configuration in Figure 30) was tested by computing the partial atomic charges from the Density Derived Electrostatic and Chemical (DDEC6) charge analysis approach.[90] Table 6 presents the statistics of partial atomic charges and the actual charges of the protons are given in Table 7. The net atomic DDEC6 charges reported are computed by analyzing the charge densities obtained from VASP.

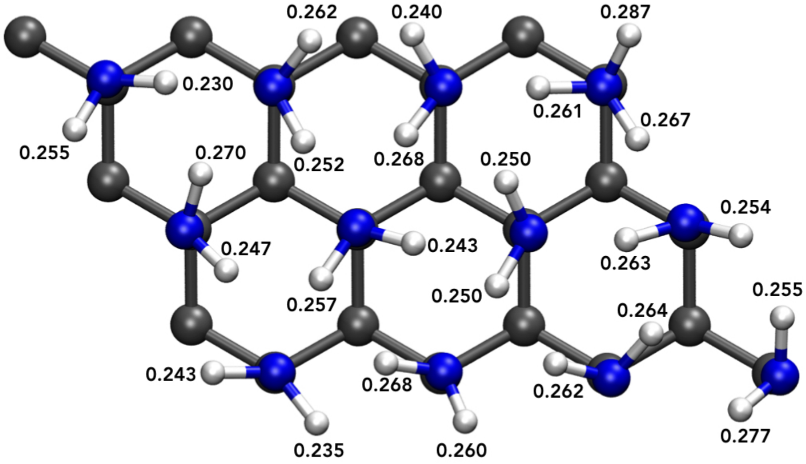

Figure 35: Schematic representation of top view, graphamine (4 × 3) supercell with an excess proton (carbons in gray, nitrogens in blue, hydrogens in white). DDEC6 atomic partial charges of the protons are noted.

C.3 Phonon Properties

All the phonon bands for a 3×3 supercell of the configuration of graphamine shown in Figure 1 of the main text (total of 648 atoms) are shown in Figure **??**. The phonon modes can be categorized into three regions: high, middle and low frequencies, which corresponds to the ranges ≈ 80—110 THz, ≈ 45—55 THz, ≈ 0 —40 THz, respectively. A feature of

Table 9: Statistics (mean, maximum, minimum and standard deviation) of DDEC6 atomic partial charges of protonated graphamine in comparison to the protonated 1-D hydroxylated graphane [76]

Quantity	Graphamine (this work)	1-D hydroxylated graphane[76]
$\overline{q}$	0.257	0.380
q_{max}	0.287	0.404
q_{min}	0.229	0.3527
q_{σ}	0.013	0.02

degeneracy for the optical modes can be found at several frequency ranges along the principle directions. We have also calculated the total phonon density of states (PDOS) (shown on the right of Figure **??**). An analysis of the PDOS suggests that the sharp peaks at ≈ 2950 cm^{-1} (88.44 THz) corresponds to C—H stretching and the region between ≈ 3000 and 3500 cm^{-1} (90 and 105 THz) is related to the N —H stretching modes. Convergence of the size of the supercell was tested by comparing results from 2×2×1 and 3×3×1 calculations. We did not find any significant differences in the computed phonon frequencies between the supercell dimensions. Hence, a 3×3×1 supercell was used to assure accuracy of the calculations.

The phonon density of states calculations were used to generate thermodynamic properties of graphamine, specifically the Helmholtz free energy, the entropy, and the specific heat capacity, as a function of temperature. The results of these calculations are plotted in Figure 37.

Table 10: DDEC6 partial charges for protons of amine groups (coordinates in Cartesian format) of protonated graphamine shown in Figure 30

x	y	z	q
0.089106	3.190138	4.418300	0.269171
-3.741856	6.902757	4.294100	0.243256
0.432799	1.610127	4.418560	0.246854
1.718076	3.723220	4.305420	0.252748
1.812217	5.348050	4.385620	0.262284
-2.205284	6.075514	4.271940	0.235236
1.978178	1.530945	4.298580	0.256931
3.039425	0.158753	4.403280	0.268328
3.368613	3.836946	4.308640	0.268068
3.449020	5.460538	4.281160	0.240221
3.475827	2.076492	4.349740	0.242828
0.263792	6.079977	4.377560	0.259875
4.831578	1.416657	4.303540	0.250217
4.975458	3.084845	4.440540	0.250497
5.528588	4.578911	4.218520	0.261013
5.776081	0.169570	4.419540	0.261804
6.945028	2.129403	4.339520	0.262915
6.987971	5.425487	4.329960	0.287465
7.115103	3.745863	4.222740	0.267854
7.341340	0.601628	4.356020	0.264667
4.757761	6.243540	4.449460	0.277082
8.804862	2.243281	4.409720	0.253956
9.319486	0.857380	4.404520	0.255595
-0.494370	4.674680	4.323420	0.229054
-1.957060	3.923983	4.356400	0.255776

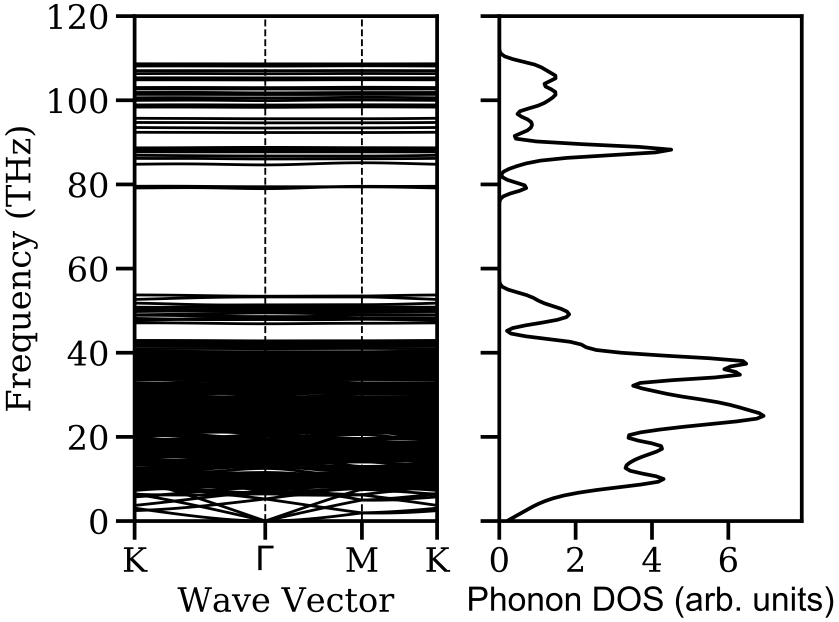

Figure 36: Phonon dispersion curves (left) and phonon density of states (right) computed with the PBE functional for a 3×3 supercell of the graphamine system shown in Figure 1 of the main text.

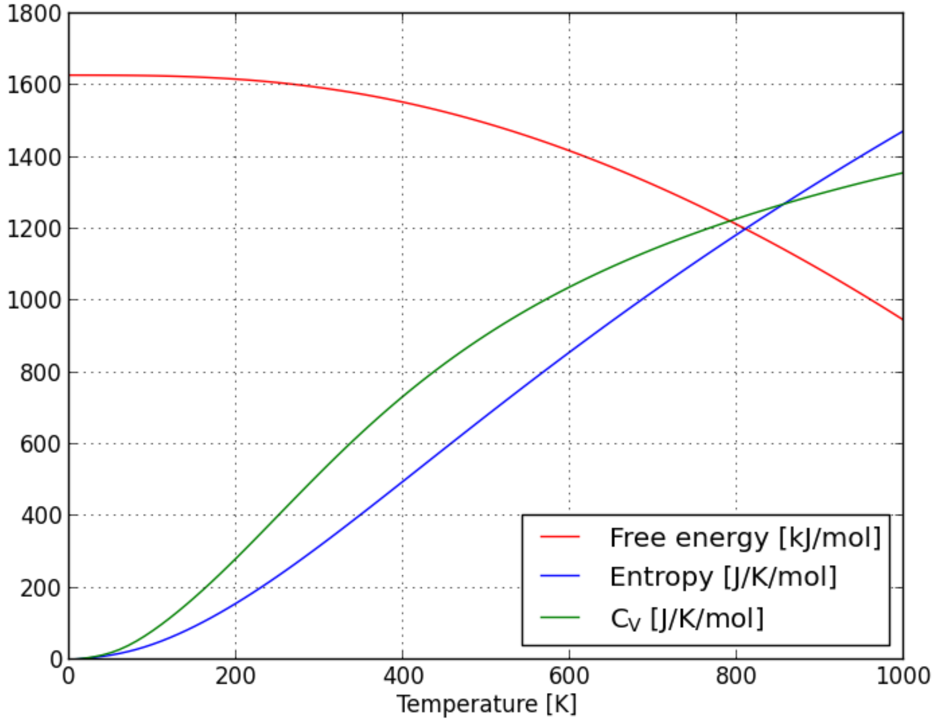

Figure 37: Thermodynamic properties for graphamine computed from the phonon density of states.

C.4 Elastic Properties

A rectangular supercell (Figure 38) was used for these calculations. A set of 20 lattice parameters were obtained by perturbing the equilibrium lattice parameters accordingly to reflect compression and tension. The atomic positions were then scaled to accommodate the new lattice parameters and the atoms were allowed to fully relax until the energy convergence tolerance of 10^{-8} eV. The elastic strain energy (E_s) per unit area was determined as a difference between electronic energy under strain ($E_s(\epsilon)$) and system at equilibrium ($E_s(\epsilon = 0)$). Under uniaxial conditions, strain was applied only along x-direction ($\epsilon_{yy} = 0$) and strain energy was fitted to a parabolic expression $E_s(\epsilon_{xx}) = C_{11}\epsilon_{xx}^2/2$. Similarly, equi-biaxial ($\epsilon_{xx} = \epsilon_{yy}$) strain energy was fitted to an expression $E_s(\epsilon_{xx}) = (C_{11} + C_{12})\epsilon_{xx}^2$. Elastic strain energies under the conditions of uniaxial and equi-biaxial strain loading were fitted to a parabolic equation and the elastic constants (C_{11}=267.09, C_{12}=34.59) were determined. A plot of the fit is shown in Figure 39.

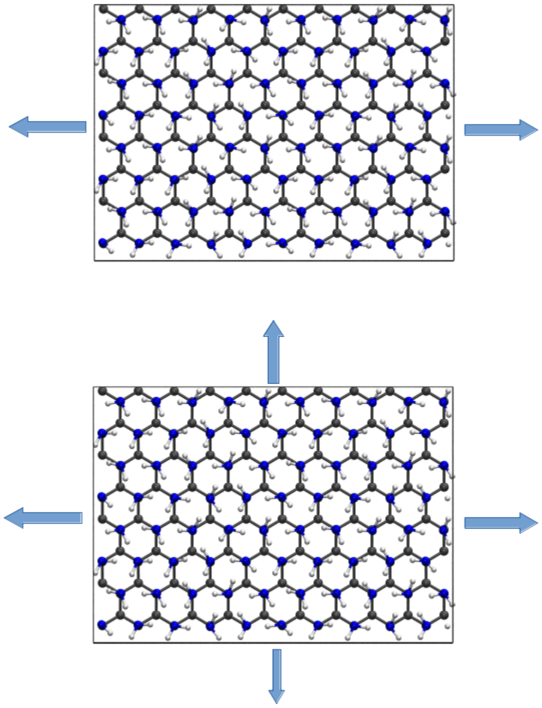

Figure 38: Equilibrium supercell used to compute elastic properties is shown under (top) uniaxial strain, (bottom) equi-biaxial strain.

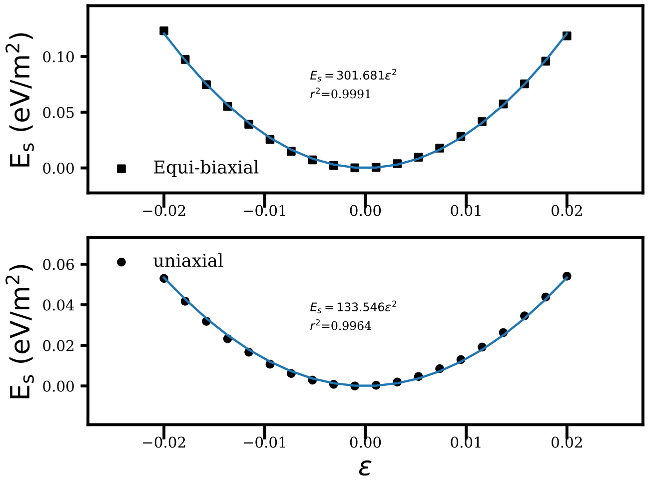

Figure 39: Parabolic fit of strain energy under uniaxial and equi-biaxial strain loading within the limits of ± 2%.

C.5 Atomic Coordinates of Graphamine

Fractional representation of positions for graphamine in Figure 1. of main text.

```
GNH2
   1.00000000000000
    10.7030863061231525    0.0000000000000000    0.0000000000000000
    -4.0136573647961828    6.9518584800000003    0.0000000000000000
     0.0000000000000000    0.0000000000000000   20.0000000000000000
   C    N    H
    24    12    36
Direct
  0.3745019151868440  0.6701008126533704  0.1251131538690408
  0.2911539101208593  0.4490174884662125  0.1009129194218735
  0.1259329597462816  0.0056141178947602  0.1256845331822101
  0.5417074996849509  0.7801367759300702  0.1010436508308580
  0.2917672193684045  0.1149743582445821  0.1003194786079173
  0.3754008674383157  0.3363215189332098  0.1256296562766789
  0.6243693821842402  0.6687346040384885  0.1256691637712113
  0.5417520624068025  0.4475867940798414  0.1011368196390258
  0.3756411734180066  0.0030422766520403  0.1241332594188878
  0.7911271123402572  0.7805252046960237  0.1010434446443231
  0.6261051273753336  0.3372083948153743  0.1251463131567982
  0.5431279552719452  0.1159199560083629  0.1002211394994784
  0.8760017479611026  0.6716780985818368  0.1255210304947640
  0.7930419542784287  0.4489525020378679  0.1012258492993533
  0.6257259041562309  0.0031220659804954  0.1246466243136691
  0.8766031252736850  0.3381858712031018  0.1252776002766627
  0.7923039416051012  0.1142556954419323  0.1011751974300411
  0.8748960906478518  0.0035916363102297  0.1253499817774776
  0.0421604743731989  0.1147027164416659  0.1011075816002014
  0.1249865643394417  0.3381700991204697  0.1252081413061810
  0.2921469323373777  0.7824621058642823  0.1003796168693751
  0.0419695359534112  0.4484406558123500  0.0998499839370292
  0.1252387294590578  0.6712460430963296  0.1252392969793828
  0.0418337764971591  0.7826300735690455  0.1013318721602319
  0.3660049385752613  0.6628626740152642  0.1985508021305322
  0.1343050034029180  0.0133683241100714  0.1998813082292637
  0.3736997228506665  0.3254800014843818  0.1984137896962267
  0.6191193672046426  0.6631285819954507  0.2005437373345011
  0.3801346074934819  0.0008068855080335  0.1982998927378331
  0.6308889219221047  0.3405446850081187  0.1998468404420638
  0.6219521771696791  0.9990580158918184  0.1990635732680583
  0.8780583359935092  0.6793294756033262  0.2000804003074871
  0.8806413385088154  0.3489265582169026  0.1988547046131471
  0.8745178171525750  0.0046853441518751  0.1997405233194919
  0.1220056148193333  0.3425313569502602  0.1983022835261791
  0.1264398353524887  0.6725040979459497  0.1994079425657839
  0.0476390068485501  0.0128776895667405  0.2198586839409126
  0.2100006719959029  0.3445655319943516  0.2168206926823298
  0.2910343053443395  0.4493298795557968  0.0456802570610256
  0.4489639564353259  0.7780830671426546  0.2201965329867085
  0.3687808537299232  0.5454308469366641  0.2144675691279299
  0.1356900552396456  0.8914348101360496  0.2153294942271557
```

0.2751620246499180	0.2093660482545394	0.2160473016184500
0.2913895841970933	0.1159985235077209	0.0450925730449632
0.5427586057952601	0.7791559280976835	0.0458078417410902
0.4566588775883882	0.4392091350226785	0.2221776900050058
0.6094278807606643	0.7787812473627004	0.2155983756392363
0.2904789273161307	0.8825139809018561	0.2161669058261494
0.3765349953695832	0.1208709398834178	0.2132787560884345
0.5414439206774475	0.4477088403966048	0.0459059571915337
0.5499036551586315	0.2156026587769895	0.2181560335847677
0.7179731163309935	0.6934069265890501	0.2173293609755484
0.7902666544230791	0.7790955573682163	0.0458084539962127
0.5446660633775094	0.1192988455347484	0.0450202434266973
0.6073927048936519	0.4429019117509038	0.2152301864465584
0.5250485380834565	0.9974761130484572	0.2110588375198703
0.7939106409582263	0.4498970534055076	0.0460265941311761
0.7006323836190045	0.1281429602770787	0.2157251685425796
0.7879269645446266	0.3439795961297961	0.2155536167657701
0.9729674508814385	0.6939496731138264	0.2167633262524777
0.8003215919038286	0.5499425431511600	0.2177638962131110
0.7922490822337065	0.1134237544731865	0.0459257533547933
0.7758607056068254	0.9794392785062501	0.2150815578673957
0.8988920655943218	0.2482775673152076	0.2197481015130545
0.8782825845554866	0.8818444905759782	0.2134961191629332
0.0408963467073360	0.1104411423336115	0.0458463366869580
0.2913480755583698	0.7814367839188858	0.0451500320335042
0.2085876570092023	0.6429207603662079	0.2121495324743093
0.0349048371283968	0.2176098096832405	0.2140061855606239
0.0406615554196859	0.4485213661264536	0.0445463404208492
0.0343721375900258	0.5431613071170532	0.2127858793570012
0.0409137106654046	0.7832208022190602	0.0460840834147081

Appendix D Liquid-vapor Isotope Fractionation Ratio for Water Isotopologues

Table 11: Data of Liquid-vapor H/D IFR for $H_2O_{(l)} + HDO_{(v)} \leftrightharpoons H_2O_{(v)} + HDO_{(l)}$ from q-TIP4P/F, NN-revPBE0-D3 and Experiements [116]

T (K)		$10^3\ ln(\alpha)$	
	[Expt]^1	[q-TIP4P/F]	[NN-revPBE0-D3]
293	81.147	113.507 ± 1.89	91.265 ± 1.88
393	20.858	37.112 ± 2.17	24.371 ± 2.67
493	0.933	6.394 ± 1.52	5.041 ± 1.12
613	-2.640	-2.783 ± 1.2	-3.496 ± 1.87

The experimental data of H/D fractionation ratio were regressed to the expression below,

$$1158.8(T^3/10^9) - 1620.1(T^2/10^6) + 794.84(T/10^3) - 161.04 + 2.9992(10^9/T^3) \qquad \text{(D.1)}$$

where T is temperature in K.

Table 12: Data of Liquid-vapor H/T IFR for $H_2O_{(l)} + HTO_{(v)} \leftrightharpoons H_2O_{(v)} + HTO_{(l)}$ from q-TIP4P/F, NN-revPBE0-D3 and Experimets [155, 156]

T (K)	$10^3\ ln(\alpha)$ [Expt]	T (K)	$10^3\ ln(\alpha)$ [q-TIP4P/F]	 [NN-revPBE0-D3]
283	114.221	293	146.915 ± 5.0	121.845 ± 3.12
293	86.177	393	43.403 ± 1.33	22.092 ± 4.23
293.03	107.059	493	-5.605 ± 4.50	5.230 ± 1.23
303	75.107	613	-8.364 ± 0.12	-9.143 ± 1.043
303.01	91.667			
313.02	73.250			
323	63.913			
	73.250			
333.01	50.693			
343	36.332			
353	52.592			

Bibliography

[1] K.D. Kreuer, M. Schuster, B. Obliers, O. Diat, U. Traub, A. Fuchs, U. Klock, S.J. Paddison, and J. Maier. Short-side-chain proton conducting perfluorosulfonic acid ionomers: Why they perform better in pem fuel cells. *J. Power Sources*, 178(2):499–509, 2008.

[2] K.D. Kreuer. On the development of proton conducting polymer membranes for hydrogen and methanol fuel cells. *J. Membr. Sci.*, 185(1):29–39, 2001.

[3] M. Eikerling, A. A. Kornyshev, A. M. Kuznetsov, J. Ulstrup, and S. Walbran. Mechanisms of proton conductance in polymer electrolyte membranes. *J. Phys. Chem. B*, 105(17):3646–3662, 2001.

[4] K.D. Kreuer. Proton conductivity: Materials and applications. *Chem. Mater.*, 8(3):610–641, 1996.

[5] Kenneth A. Mauritz and Robert B. Moore. State of understanding of nafion. *Chem. Rev.*, 104(10):4535–4586, 2004.

[6] Martin F.H. Schuster and Wolfgang H. Meyer. Anhydrous proton conducting polymers. *Annu. Rev. Mater. Res.*, 33(1):233–261, 2003.

[7] Jianlu Zhang, Zhong Xie, Jiujun Zhang, Yanghua Tang, Chaojie Song, and *et al.* High temperature pem fuel cells. *J. Power Sources*, 160(2):872–891, 2006.

[8] James B Duncan and David A Nelson. The separation of tritiated water using supported polyphosphazene membranes. *J. Membrane Sci.*, 157(2):211–217, 1999.

[9] Viral Mehta and Joyce Smith Cooper. Review and analysis of pem fuel cell design and manufacturing. *J. Power Sources*, 114(1):32–53, 2003.

[10] Michael A. Hickner, Hossein Ghassemi, Yu Seung Kim, Brian R. Einsla, and James E. McGrath. Alternative polymer systems for proton exchange membranes (pems). *Chem. Rev.*, 104(10):4587–4612, 2004.

[11] Sung Yeon Kim, Suhan Kim, and Moon Jeong Park. Enhanced proton transport in nanostructured polymer electrolyte/ionic liquid membranes under water-free conditions. *Nat. Commun.*, 1(7):1–7, 2010.

[12] Yangbin Chen, Michael Thorn, Scott Christensen, Craig Versek, Ambata Poe, Ryan C. Hayward, Mark T. Tuominen, and S. Thayumanavan. Enhancement of anhydrous proton transport by supramolecular nanochannels in comb polymers. *Nat. Chem.*, 2(6):503–508, 2010.

[13] Linas Vilčiauskas, Mark E. Tuckerman, Gabriel Bester, Stephen J. Paddison, and Klaus-Dieter Kreuer. The mechanism of proton conduction in phosphoric acid. *Nat. Chem.*, 4(6):461–466, 2012.

[14] Wei L Wang and Efthimios Kaxiras. Graphene hydrate: Theoretical prediction of a new insulating form of graphene. *New J. Phys.*, 12(12):125012, 2010.

[15] G. Kresse and J. Furthmüller. Efficient iterative schemes for ab initio total-energy calculations using a plane-wave basis set. *Phys. Rev. B*, 54(16):11169–11186, 1996.

[16] Paolo Giannozzi, Stefano Baroni, Nicola Bonini, Matteo Calandra, Roberto Car, Carlo Cavazzoni, Davide Ceresoli, Guido L Chiarotti, Matteo Cococcioni, Ismaila Dabo, and *et al.* Quantum espresso: a modular and open-source software project for quantum simulations of materials. *J. Phys.: Condens. Matter*, 21(39):395502, 2009.

[17] John P. Perdew, Kieron Burke, and Matthias Ernzerhof. Generalized gradient approximation made simple. *Phys. Rev. Lett.*, 77(18):3865–3868, 1996.

[18] Graeme Henkelman, Blas P. Uberuaga, and Hannes Jónsson. A climbing image nudged elastic band method for finding saddle points and minimum energy paths. *J. Chem. Phys.*, 113(22):9901, 2000.

[19] Tyler J. F. Day, Alexander V. Soudackov, Martin Čuma, Udo W. Schmitt, and Gregory A. Voth. A second generation multistate empirical valence bond model for proton transport in aqueous systems. *J. Chem. Phys.*, 117(12):5839, 2002.

[20] Shulu Feng and Gregory A. Voth. Proton solvation and transport in hydrated nafion. *J. Phys. Chem. B*, 115(19):5903–5912, 2011.

[21] Shimon Ochi, Osamu Kamishima, Junichiro Mizusaki, and Junichi Kawamura. Investigation of proton diffusion in nafion®117 membrane by electrical conductivity and nmr. *Solid State Ionics*, 180(6-8):580–584, 2009.

[22] Marcella Cappadonia, J Wilhelm Erning, Seyedeh M Saberi Niaki, and Ulrich Stimming. Conductance of nafion 117 membranes as a function of temperature and water content. *Solid State Ionics*, 77(nil):65–69, 1995.

[23] Tejs Vegge. Locating the rate-limiting step for the interaction of hydrogen with mg (0001) using density-functional theory calculations and rate theory. *Phys. Rev. B*, 70(3):035412, 2004.

[24] Justin T. Fermann and Scott Auerbach. Modeling proton mobility in acidic zeolite clusters: Ii. room temperature tunneling effects from semiclassical rate theory. *J. Chem. Phys.*, 112(15):6787–6794, 2000.

[25] Thomas A. Manz and Nidia Gabaldon Limas. Introducing ddec6 atomic population analysis: Part 1. charge partitioning theory and methodology. *RSC Adv.*, 6(53):47771–47801, 2016.

[26] G. Makov and M. C. Payne. Periodic boundary conditions in ab initio calculations. *Phys. Rev. B*, 51(7):4014–4022, 1995.

[27] Ismaila Dabo, Boris Kozinsky, Nicholas E. Singh-Miller, and Nicola Marzari. Electrostatics in periodic boundary conditions and real-space corrections. *Phys. Rev. B*, 77(11):115139, 2008.

[28] Alberto Striolo. The mechanism of water diffusion in narrow carbon nanotubes. *Nano Lett.*, 6(4):633–639, 2006.

[29] Nils E. R. Zimmermann, Timm J. Zabel, and Frerich J. Keil. Transport into nanosheets: Diffusion equations put to test. *J. Phys. Chem. C*, 117(14):7384–7390, 2013.

[30] Anh Phan, David R. Cole, R. Gregor Weiß, Joachim Dzubiella, and Alberto Striolo. Confined water determines transport properties of guest molecules in narrow pores. *ACS Nano*, 10(8):7646–7656, 2016.

[31] Noam Agmon. The grotthuss mechanism. *Chem. Phys. Lett.*, 244(5-6):456–462, Oct 1995.

[32] Christoph Dellago and Gerhard Hummer. Kinetics and mechanism of proton transport across membrane nanopores. *Phys. Rev. Lett.*, 97(24):245901, 2006.

[33] Timothy C. Berkelbach, Hee-Seung Lee, and Mark E. Tuckerman. Concerted hydrogen-bond dynamics in the transport mechanism of the hydrated proton: A first-principles molecular dynamics study. *Phys. Rev. Lett.*, 103(23):238302, 2009.

[34] Christoph Dellago, Mor M. Naor, and Gerhard Hummer. Proton transport through water-filled carbon nanotubes. *Phys. Rev. Lett.*, 90(10):105902, 2003.

[35] Chikkannagari Nagamani, Usha Viswanathan, Craig Versek, Mark T. Tuominen, Scott M. Auerbach, and S. Thayumanavan. Importance of dynamic hydrogen bonds and reorientation barriers in proton transport. *Chem. Commun.*, 47(23):6638, 2011.

[36] AI Baranov, BV Merinov, AV Tregubchenko, VP Khiznichenko, LA Shuvalov, and NM Schagina. Fast proton transport in crystals with a dynamically disordered hydrogen bond network. *Solid State Ionics*, 36(3-4):279–282, 1989.

[37] V. I. Ivanov-Omskii and S. G. Yastrebov. Transport of protons in amorphous hydrogenated carbon. *Semiconductors*, 39(8):941–943, 2005.

[38] E. S. Kryachko and V. P. Sokhan. Soliton model for collective proton transfer in extended realistic hydrogen-bonded systems. *Proc. R. Soc. A*, 439(1906):211–226, 1992.

[39] M. Baraket, S. G. Walton, E. H. Lock, J. T. Robinson, and F. K. Perkins. The functionalization of graphene using electron-beam generated plasmas. *Appl. Phys. Lett.*, 96(23):231501, 2010.

[40] Judy Hirst. Mitochondrial complex i. *Annu. Rev. Biochem.*, 82(1):551–575, 2013.

[41] Sheue Yann Cheng, Jack L Leonard, and Paul J. Davis. Molecular aspects of thyroid hormone actions. *Endocr. Rev.*, 31 2:139–70, 2010.

[42] Ute Armbruster, Viviana Correa Galvis, Hans-Henning Kunz, and Deserah D. Strand. The regulation of the chloroplast proton motive force plays a key role for photosynthesis in fluctuating light. *Curr. Opin. Plant Biol.*, 37:56 – 62, 2017.

[43] David J. Vinyard, Gennady M. Ananyev, and G. Charles Dismukes. Photosystem ii: The reaction center of oxygenic photosynthesis. *Annu. Rev. Biochem.*, 82(1):577–606, 2013.

[44] Sanjib Paul, Tanmoy Kumar Paul, and Srabani Taraphder. Reaction coordinate, free energy, and rate of intramolecular proton transfer in human carbonic anhydrase ii. *J. Phys. Chem. B.*, 122(11):2851–2866, 2018.

[45] Ahmet Kusoglu and Adam Z. Weber. New insights into perfluorinated sulfonic-acid ionomers. *Chem. Rev.*, 117(3):987–1104, Jan 2017.

[46] Dong Won Shin, Michael D. Guiver, and Young Moo Lee. Hydrocarbon-based polymer electrolyte membranes: Importance of morphology on ion transport and membrane stability. *Chem. Rev.*, 117(6):4759–4805, 2017.

[47] Mykhaylo V. Lototskyy, Ivan Tolj, Moegamat Wafeeq Davids, Yevgeniy V. Klochko, and et al. Metal hydride hydrogen storage and supply systems for electric forklift with low-temperature proton exchange membrane fuel cell power module. *Int. J. Hydrog. Energy*, 41(31):13831–13842, Aug 2016.

[48] Dominik Marx. Proton transfer 200 years after von grotthuss: Insights from ab initio simulations. *ChemPhysChem*, 7(9):1848–1870, Sep 2006.

[49] Noam Agmon, Huib J. Bakker, R. Kramer Campen, Richard H. Henchman, Peter Pohl, Sylvie Roke, Martin Thämer, and Ali Hassanali. Protons and hydroxide ions in aqueous systems. *Chem. Rev.*, 116(13):7642–7672, 2016.

[50] C. T. Wolke, J. A. Fournier, L. C. Dzugan, M. R. Fagiani, T. T. Odbadrakh, H. Knorke, K. D. Jordan, A. B. McCoy, K. R. Asmis, and M. A. Johnson. Spectroscopic snapshots of the proton-transfer mechanism in water. *Science*, 354(6316):1131–1135, Dec 2016.

[51] Daniel Muñoz Santiburcio and Dominik Marx. Nanoconfinement in slit pores enhances water self-dissociation. *Phys. Rev. Lett.*, 119(5), Jul 2017.

[52] Yamila A. Perez Sirkin, Ali Hassanali, and Damián A. Scherlis. One-dimensional confinement inhibits water dissociation in carbon nanotubes. *J. Phys. Chem. Lett*, 9(17):5029–5033, Aug 2018.

[53] Emilia V. Silletta, Mark E. Tuckerman, and Alexej Jerschow. Unusual proton transfer kinetics in water at the temperature of maximum density. *Phys. Rev. Lett.*, 121(7), Aug 2018.

[54] Jung-Ho Wee. Applications of proton exchange membrane fuel cell systems. *Renew. Sust. Energy. Rev.*, 11(8):1720–1738, Oct 2007.

[55] Brian C. H. Steele and Angelika Heinzel. Materials for fuel-cell technologies. *Nature*, 414(6861):345–352, Nov 2001.

[56] Jin-Soo Park, Mun-Sik Shin, and Chang-Soo Kim. Proton exchange membranes for fuel cell operation at low relative humidity and intermediate temperature: An updated review. *Curr. Opin. Electrochem.*, 5(1):43–55, Oct 2017.

[57] Padmini Ramaswamy, Norman E. Wong, and George K. H. Shimizu. Mofs as proton conductors–challenges and opportunities. *Chem. Soc. Rev.*, 43(16):5913, Apr 2014.

[58] S.J. Paddison. Proton conduction mechanisms at low degrees of hydration in sulfonic acid-based polymer electrolyte membranes. *Annu. Rev. Mater. Sci.*, 33(1):289, Aug 2003.

[59] Suman Chandra, Tanay Kundu, Sharath Kandambeth, Ravichandar BabaRao, Yogesh Marathe, Shrikant M. Kunjir, and Rahul Banerjee. Phosphoric acid loaded azo $(-N = N-)$ based covalent organic framework for proton conduction. *J. Am. Chem. Soc.*, 136(18):6570, Apr 2014.

[60] Hong-Bin Luo, Mei Wang, Jin Zhang, Zheng-Fang Tian, Yang Zou, and Xiao-Ming Ren. Open-framework chalcogenide showing both intrinsic anhydrous and water-assisted high proton conductivity. *ACS Appl. Mater. Interfaces*, 10(3):2619–2627, Jan 2018.

[61] Munehiro Inukai, Satoshi Horike, Tomoya Itakura, Ryota Shinozaki, Naoki Ogiwara, Daiki Umeyama, Sanjog Nagarkar, Yusuke Nishiyama, Michal Malon, Akari Hayashi, and et al. Encapsulating mobile proton carriers into structural defects in coordination polymer crystals: High anhydrous proton conduction and fuel cell application. *J. Am. Chem. Soc.*, 138(27):8505–8511, Jul 2016.

[62] G. K. H. Shimizu, J. M. Taylor, and S. Kim. Proton conduction with metal-organic frameworks. *Science*, 341(6144):354, Jul 2013.

[63] Satoshi Horike, Daiki Umeyama, and Susumu Kitagawa. Ion conductivity and transport by porous coordination polymers and metal–organic frameworks. *Acc. Chem. Res.*, 46(11):2376–2384, 2013.

[64] Linas Vilčiauskas, Mark E. Tuckerman, Gabriel Bester, Stephen J. Paddison, and Klaus-Dieter Kreuer. The mechanism of proton conduction in phosphoric acid. *Nat. Chem.*, 4(6):461–466, Apr 2012.

[65] Jeff A. Hurd, Ramanathan Vaidhyanathan, Venkataraman Thangadurai, Christopher I. Ratcliffe, Igor L. Moudrakovski, and George K. H. Shimizu. Anhydrous proton conduction at 150 ° c in a crystalline metal-organic framework. *Nat. Chem.*, 1(9):705–710, Oct 2009.

[66] Ai-Lin Li, Qiang Gao, Jian Xu, and Xian-He Bu. Proton-conductive metal-organic frameworks: Recent advances and perspectives. *Coord. Chem. Rev.*, 344:54 – 82, 2017.

[67] Minyoung Yoon, Kyungwon Suh, Hyunuk Kim, Yonghwi Kim, Narayanan Selvapalam, and Kimoon Kim. High and highly anisotropic proton conductivity in organic molecular porous materials. *Angew. Chem. Int. Ed.*, 50(34):7870–7873, Jun 2011.

[68] Sanjog S. Nagarkar, Sreekuttan M. Unni, Amitosh Sharma, Sreekumar Kurungot, and Sujit K. Ghosh. Two-in-one: Inherent anhydrous and water-assisted high proton conduction in a 3d metal-organic framework. *Angew. Chem.*, 126(10):2676, Dec 2013.

[69] Yongwu Peng, Guodong Xu, Zhigang Hu, Youdong Cheng, Chenglong Chi, Daqiang Yuan, Hansong Cheng, and Dan Zhao. Mechanoassisted synthesis of sulfonated covalent organic frameworks with high intrinsic proton conductivity. *ACS Appl. Mater. Interfaces*, 8(28):18505, Jul 2016.

[70] Padmini Ramaswamy, Norman E. Wong, Benjamin S. Gelfand, and George K. H. Shimizu. A water stable magnesium mof that conducts protons over 10^{-2} s cm^{-1}. *J. Am. Chem. Soc.*, 137(24):7640, Jun 2015.

[71] Jorge O. Sofo, Ajay S. Chaudhari, and Greg D. Barber. Graphane: A two-dimensional hydrocarbon. *Phys. Rev. B.*, 75(15):153401, Apr 2007.

[72] Hwee Ling Poh, Zdeněk Sofer, Petr Šimek, Ivo Tomandl, and Martin Pumera. Hydroboration of graphene oxide: Towards stoichiometric graphol and hydroxygraphane. *Chem. Eur. J.*, 21(22):8130–8136, Apr 2015.

[73] Francesco Buonocore, Andrea Capasso, and Nicola Lisi. An ab initio study of hydroxylated graphane. *J. Chem. Phys.*, 147(10):104705, Sep 2017.

[74] Li Cao, Hong Wu, Pengfei Yang, Xueyi He, Jinzhao Li, Yan Li, Mingzhao Xu, Ming Qiu, and Zhongyi Jiang. Graphene oxide-based solid electrolytes with 3d prepercolating pathways for efficient proton transport. *Adv. Funct. Mater.*, page 1804944, Oct 2018.

[75] Mohammad Razaul Karim, Kazuto Hatakeyama, Takeshi Matsui, Hiroshi Takehira, Takaaki Taniguchi, Michio Koinuma, Yasumichi Matsumoto, Tomoyuki Akutagawa,

Takayoshi Nakamura, Shin-ichiro Noro, and et al. Graphene oxide nanosheet with high proton conductivity. *J. Am. Chem. Soc.*, 135(22):8097–8100, May 2013.

[76] Abhishek Bagusetty, Pabitra Choudhury, Wisssam A. Saidi, Bridget Derksen, Elizabeth Gatto, and J. Karl Johnson. Facile anhydrous proton transport on hydroxyl functionalized graphane. *Phys. Rev. Lett.*, 118(18):186101, 2017.

[77] Edward B. Trigg, Taylor W. Gaines, Manuel Maréchal, Demi E. Moed, Patrice Rannou, Kenneth B. Wagener, Mark J. Stevens, and Karen I. Winey. Self-assembled highly ordered acid layers in precisely sulfonated polyethylene produce efficient proton transport. *Nat. Mater.*, 17(8):725–731, May 2018.

[78] Daiki Umeyama, Satoshi Horike, Munehiro Inukai, Tomoya Itakura, and Susumu Kitagawa. Inherent proton conduction in a 2d coordination framework. *J. Am. Chem. Soc.*, 134(30):12780–12785, Jul 2012.

[79] G. Kresse and J. Hafner. Ab initio molecular dynamics for liquid metals. *Phys. Rev. B*, 47(1):558–561, 1993.

[80] G. Kresse and J. Furthmüller. Efficiency of ab-initio total energy calculations for metals and semiconductors using a plane-wave basis set. *Comput. Mater. Sci.*, 6(1):15–50, 1996.

[81] G. Kresse and D. Joubert. From ultrasoft pseudopotentials to the projector augmented-wave method. *Phys. Rev. B*, 59(3):1758–1775, 1999.

[82] Yingkai Zhang and Weitao Yang. Comment on "generalized gradient approximation made simple". *Phys. Rev. Lett.*, 80(4):890–890, Jan 1998.

[83] Jochen Heyd, Gustavo E. Scuseria, and Matthias Ernzerhof. Hybrid functionals based on a screened coulomb potential. *J. Chem. Phys.*, 118(18):8207, May 2003.

[84] Jochen Heyd, Gustavo E. Scuseria, and Matthias Ernzerhof. Erratum: "hybrid functionals based on a screened coulomb potential" [j. chem. phys. 118, 8207 (2003)]. *J. Chem. Phys.*, 124(21):219906, Jun 2006.

[85] A Togo and I Tanaka. First principles phonon calculations in materials science. *Scr. Mater.*, 108:1–5, Nov 2015.

[86] G. Prentice. *Electrochemical Engineering Principles*. Prentice-Hall International Se. Prentice Hall, 1991.

[87] Carlo Adamo and Vincenzo Barone. Toward reliable density functional methods without adjustable parameters: The pbe0 model. *J. Chem. Phys.*, 110(13):6158–6170, Apr 1999.

[88] P. J. Stephens, F. J. Devlin, C. F. Chabalowski, and M. J. Frisch. Ab initio calculation of vibrational absorption and circular dichroism spectra using density functional force fields. *J. Phys. Chem.*, 98(45):11623–11627, Nov 1994.

[89] Alejandro J. Garza and Gustavo E. Scuseria. Predicting band gaps with hybrid density functionals. *J. Phys. Chem. Lett.*, 7(20):4165, Oct 2016.

[90] Nidia Gabaldon Limas and Thomas A. Manz. Introducing ddec6 atomic population analysis: Part 2. computed results for a wide range of periodic and nonperiodic materials. *RSC Adv.*, 6(51):45727–45747, 2016.

[91] Abhishek Bagusetty, Joshua Livingston, and J. Karl Johnson. Graphamine: Amine functionalized graphane for intrinsic anhydrous proton conduction. *J. Phys. Chem. C*, Dec 2018.

[92] M. Topsakal, S. Cahangirov, and S. Ciraci. The response of mechanical and electronic properties of graphane to the elastic strain. *Appl. Phys. Lett.*, 96(9):091912, 2010.

[93] Emiliano Cadelano, Pier Luca Palla, Stefano Giordano, and Luciano Colombo. Elastic properties of hydrogenated graphene. *Phys. Rev. B*, 82(23):235414, Dec 2010.

[94] C. Lee, X. Wei, J. W. Kysar, and J. Hone. Measurement of the elastic properties and intrinsic strength of monolayer graphene. *Science*, 321(5887):385, Jul 2008.

[95] Chanchal Chakraborty, Utpal Rana, Rakesh K. Pandey, Satoshi Moriyama, and Masayoshi Higuchi. One-dimensional anhydrous proton conducting channel formation at high temperature in a pt(ii)-based metallo-supramolecular polymer and imidazole system. *ACS Appl. Mater. Interfaces*, 9(15):13406, Apr 2017.

[96] Joost VandeVondele, Matthias Krack, Fawzi Mohamed, Michele Parrinello, Thomas Chassaing, and Jürg Hutter. Quickstep: Fast and accurate density functional calculations using a mixed gaussian and plane waves approach. *Comput. Phys. Commun.*, 167(2):103–128, 2005.

[97] Jürg Hutter, Marcella Iannuzzi, Florian Schiffmann, and Joost VandeVondele. Cp2k: Atomistic simulations of condensed matter systems. *WIREs Comput Mol Sci.*, 4(1):15–25, 2013.

[98] Gerald Lippert, Jürg Hutter, and Michele Parrinello. The gaussian and augmented-plane-wave density functional method for ab initio molecular dynamics simulations. *Theor. Chem. Acc.*, 103(2):124–140, 1999.

[99] Joost VandeVondele and Jürg Hutter. Gaussian basis sets for accurate calculations on molecular systems in gas and condensed phases. *J. Chem. Phys.*, 127(11):114105, 2007.

[100] S. Goedecker, M. Teter, and J. Hutter. Separable dual-space gaussian pseudopotentials. *Phys. Rev. B*, 54(3):1703–1710, 1996.

[101] Joost VandeVondele and Jürg Hutter. An efficient orbital transformation method for electronic structure calculations. *J. Chem. Phys.*, 118(10):4365, 2003.

[102] Michele Ceriotti, Giovanni Bussi, and Michele Parrinello. Nuclear quantum effects in solids using a colored-noise thermostat. *Phys. Rev. Lett.*, 103(3):030603, 2009.

[103] Michele Ceriotti, Giovanni Bussi, and Michele Parrinello. Langevin equation with colored noise for constant-temperature molecular dynamics simulations. *Phys. Rev. Lett.*, 102(2):020601, 2009.

[104] Chad E. Junkermeier, Dmitry Solenov, and Thomas L. Reinecke. Adsorption of nh2 on graphene in the presence of defects and adsorbates. *J. Phys. Chem. C*, 117(6):2793, Feb 2013.

[105] A. Daniel Boese, Amalendu Chandra, Jan M. L. Martin, and Dominik Marx. From ab initio quantum chemistry to molecular dynamics: The delicate case of hydrogen bonding in ammonia. *J. Chem. Phys.*, 119(12):5965–5980, Sep 2003.

[106] S. Lebègue, M. Klintenberg, O. Eriksson, and M. I. Katsnelson. Accurate electronic band gap of pure and functionalized graphane from gw calculations. *Phys. Rev. B*, 79(24):245117, 2009.

[107] Nicolas Mounet and Nicola Marzari. First-principles determination of the structural, vibrational and thermodynamic properties of diamond, graphite, and derivatives. *Phys. Rev. B*, 71(20):205214, May 2005.

[108] Jakub Ederer, Pavel Janoš, Petra Ecorchard, Jakub Tolasz, and et al. Determination of amino groups on functionalized graphene oxide for polyurethane nanomaterials: Xps quantitation vs. functional speciation. *RSC Adv.*, 7:12464–12473, 2017.

[109] Stefania Sandoval, Nitesh Kumar, Judith Oro-Solé, A. Sundaresan, C.N.R. Rao, Amparo Fuertes, and Gerard Tobias. Tuning the nature of nitrogen atoms in n-containing reduced graphene oxide. *Carbon*, 96:594 – 602, 2016.

[110] Wenbo Zhang, Jianzhong Ma, Dangge Gao, Yongxiang Zhou, Congmin Li, Jiao Zha, and Jing Zhang. Preparation of amino-functionalized graphene oxide by hoffman rearrangement and its performances on polyacrylate coating latex. *Prog. Org. Coat*, 94:9 – 17, 2016.

[111] Tran Van Khai, Han Gil Na, Dong Sub Kwak, Yong Jung Kwon, Heon Ham, Kwang Bo Shim, and Hyoun Woo Kim. Influence of n-doping on the structural and photoluminescence properties of graphene oxide films. *Carbon*, 50(10):3799 – 3806, 2012.

[112] Linfei Lai, Luwei Chen, Da Zhan, Li Sun, Jinping Liu, San Hua Lim, and et al. One-step synthesis of nh_2-graphene from in situ graphene-oxide reduction and its improved electrochemical properties. *Carbon*, 49(10):3250 – 3257, 2011.

[113] Peiying Liu, Hui Wang, Tingting Yan, Jianping Zhang, Liyi Shi, and Dengsong Zhang. Grafting sulfonic and amine functional groups on 3d graphene for improved capacitive deionization. *J. Mater. Chem. A*, 4:5303–5313, 2016.

[114] Beatriz Baselga-Cervera, Camino García-Balboa, Victoria López-Rodas, Marta Fernández Díaz, and Eduardo Costas. Evidence of microalgal isotopic fractionation through enrichment of depleted uranium. *Sci. Rep.*, 9, 2019.

[115] Harold C. Urey, F. G. Brickwedde, and G. M. Murphy. A hydrogen isotope of mass 2 and its concentration. *Phys. Rev.*, 40:1–15, Apr 1932.

[116] Juske Horita and David J. Wesolowski. Liquid-vapor fractionation of oxygen and hydrogen isotopes of water from the freezing to the critical temperature. *Geochim. Cosmochim. Acta*, 58(16):3425–3437, Aug 1994.

[117] Ariel A Chialvo and Juske Horita. Liquid-vapor equilibrium isotopic fractionation of water: how well can classical water models predict it? *J. Chem. Phys.*, 130(9):094509, 2009.

[118] T. E. Markland and B. J. Berne. Unraveling quantum mechanical effects in water using isotopic fractionation. *Proc. Natl. Acad. Sci.*, 109(21):7988–7991, May 2012.

[119] Kara D. Lamb, Benjamin W. Clouser, Maximilien Bolot, Laszlo Sarkozy, Volker Ebert, and et al. Laboratory measurements of hdo/h_2o isotopic fractionation during ice deposition in simulated cirrus clouds. *Proc. Natl. Acad. Sci.*, 114(22):5612–5617, 2017.

[120] M. D. Ellehoj, H. C. Steen-Larsen, S. J. Johnsen, and M. B. Madsen. Ice-vapor equilibrium fractionation factor of hydrogen and oxygen isotopes: Experimental investigations and implications for stable water isotope studies. *Rapid Commun. Mass Spectrom.*, 27(19):2149–2158, 2013.

[121] O. Sepall and S. G. Mason. Vapor/liquid partition of tritium in tritiated water. *Can. J. Chem.*, 38(10):2024–2025, 1960.

[122] Thomas E. Markland and Michele Ceriotti. Nuclear quantum effects enter the mainstream. *Nat. Rev. Chem.*, 2(3), Feb 2018.

[123] Michele Ceriotti, Wei Fang, Peter G. Kusalik, Ross H. McKenzie, Angelos Michaelides, and et al. Nuclear quantum effects in water and aqueous systems: Experiment, theory, and current challenges. *Chem. Rev.*, 116(13):7529–7550, Apr 2016.

[124] Erich Wimmer, Walter Wolf, Jürgen Sticht, Paul Saxe, Clint B. Geller, Reza Najafabadi, and George A. Young. Temperature-dependent diffusion coefficients fromab initiocomputations: Hydrogen, deuterium, and tritium in nickel. *Phys. Rev. B*, 77(13), Apr 2008.

[125] Takehiro Yoshikawa, Toshiyuki Takayanagi, Hajime Kimizuka, and Motoyuki Shiga. Quantum–thermal crossover of hydrogen and tritium diffusion in α-iron. *J. Phys. Chem. C*, 116(43):23113–23119, Oct 2012.

[126] M. V. Persson, J. K. Jørgensen, E. F. van Dishoeck, and D. Harsono. The deuterium fractionation of water on solar-system scales in deeply-embedded low-mass protostars. *Astron. Astrophys.*, 563:A74, Mar 2014.

[127] L. J. Hallis. D/h ratios of the inner solar system. *Philos. Trans. Royal Soc. A: Mathematical, Physical and Engineering Sciences*, 375(2094):20150390, Apr 2017.

[128] Zheng Cao and James U. Bowie. An energetic scale for equilibrium h/d fractionation factors illuminates hydrogen bond free energies in proteins. *Protein Sci.*, 23(5):566–575, Mar 2014.

[129] Hitoshi Sakai and Makoto Tsutsumi. D/h fractionation factors between serpentine and water at 100° to 500°c and 2000 bar water pressure, and the d/h ratios of natural serpentines. *Earth Planet. Sc. Lett.*, 40(2):231–242, Jul 1978.

[130] Bingqing Cheng, Jörg Behler, and Michele Ceriotti. Nuclear quantum effects in water at the triple point: Using theory as a link between experiments. *J. Phys. Chem. Lett.*, 7(12):2210–2215, May 2016.

[131] Xing Wang and Harro A. J. Meijer. Ice–liquid isotope fractionation factors for 18o and 2h deduced from the isotopic correction constants for the triple point of water. *Isot. Environ. Health Stud.*, 54(3):304–311, 2018.

[132] Luis M.Sesé. Feynman-hibbs potentials and path integrals for quantum lennard-jones systems: Theory and monte carlo simulations. *Mol. Phys.*, 85(5):931–947, 1995.

[133] Jiří Vaníček, William H. Miller, Jesús F. Castillo, and F. Javier Aoiz. Quantum-instanton evaluation of the kinetic isotope effects. *J. Chem. Phys.*, 123(5):054108, 2005.

[134] Michele Ceriotti and Thomas E. Markland. Efficient methods and practical guidelines for simulating isotope effects. *J. Chem. Phys.*, 138(1):014112, Jan 2013.

[135] V. Kapil, J. VandeVondele, and M. Ceriotti. Accurate molecular dynamics and nuclear quantum effects at low cost by multiple steps in real and imaginary time: Using density functional theory to accelerate wavefunction methods. *J. Chem. Phys.*, 144(5):054111, 2016.

[136] Konstantin Karandashev and Jiří Vaníček. Accelerating equilibrium isotope effect calculations. i. stochastic thermodynamic integration with respect to mass. *J. Chem. Phys.*, 146(18):184102, 2017.

[137] Bingqing Cheng and Michele Ceriotti. Direct path integral estimators for isotope fractionation ratios. *J. Chem. Phys.*, 141(24):244112, Dec 2014.

[138] Konstantin Karandashev and Jiří Vaníček. Accelerating equilibrium isotope effect calculations. ii. stochastic implementation of direct estimators. *J. Chem. Phys.*, 151(13):134116, 2019.

[139] Tobias Morawietz, Vikas Sharma, and Jörg Behler. A neural network potential-energy surface for the water dimer based on environment-dependent atomic energies and charges. *J. Chem. Phys.*, 136(6):064103, 2012.

[140] Tobias Morawietz and Jörg Behler. A density-functional theory-based neural network potential for water clusters including van der waals corrections. *J. Phys. Chem. A*, 117(32):7356–7366, 2013.

[141] Suresh Kondati Natarajan, Tobias Morawietz, and Jörg Behler. Representing the potential-energy surface of protonated water clusters by high-dimensional neural network potentials. *Phys. Chem. Chem. Phys.*, 17:8356–8371, 2015.

[142] Thuong T. Nguyen, Eszter Székely, Giulio Imbalzano, Jörg Behler, Gábor Csányi, Michele Ceriotti, Andreas W. Götz, and Francesco Paesani. Comparison of permutationally invariant polynomials, neural networks, and gaussian approximation potentials in representing water interactions through many-body expansions. *J. Chem. Phys.*, 148(24):241725, 2018.

[143] Hao Wang and Weitao Yang. Force field for water based on neural network. *J. Phys. Chem. Lett.*, 9(12):3232–3240, May 2018.

[144] Ivan Sukuba, Lei Chen, Michael Probst, and Alexander Kaiser. A neural network interface for dl_poly and its application to liquid water. *Molecular Simulation*, 0(0):1–6, 2018.

[145] Tobias Morawietz, Andreas Singraber, Christoph Dellago, and Jörg Behler. How van der waals interactions determine the unique properties of water. *Proc. Natl. Acad. Sci.*, 113(30):8368–8373, 2016.

[146] Venkat Kapil, Jörg Behler, and Michele Ceriotti. High order path integrals made easy. *J. Chem. Phys.*, 145(23):234103, 2016.

[147] Bingqing Cheng, Edgar A. Engel, Jörg Behler, Christoph Dellago, and Michele Ceriotti. Ab initio thermodynamics of liquid and solid water. *Proc. Natl. Acad. Sci.*, 116(4):1110–1115, Jan 2019.

[148] Hsin-Yu Ko, Linfeng Zhang, Biswajit Santra, Han Wang, Weinan E, Robert A. DiStasio Jr, and Roberto Car. Isotope effects in liquid water via deep potential molecular dynamics. *Mol. Phys.*, page 1–13, Oct 2019.

[149] Steve Plimpton. Fast parallel algorithms for short-range molecular dynamics. *J. Comput. Phys.*, 117(1):1–19, Mar 1995.

[150] Michele Ceriotti, Joshua More, and David E. Manolopoulos. i-pi: A python interface for ab initio path integral molecular dynamics simulations. *Computer Phys. Commun.*, 185(3):1019–1026, Mar 2014.

[151] Venkat Kapil, Mariana Rossi, Ondrej Marsalek, Riccardo Petraglia, Yair Litman, Thomas Spura, Bingqing Cheng, Alice Cuzzocrea, Robert H. Meißner, David M. Wilkins, and et al. i-pi 2.0: A universal force engine for advanced molecular simulations. *Computer Phys. Commun.*, 236:214–223, Mar 2019.

[152] Scott Habershon, Thomas E. Markland, and David E. Manolopoulos. Competing quantum effects in the dynamics of a flexible water model. *J. Chem. Phys.*, 131(2):024501, Jul 2009.

[153] Andreas Singraber, Jörg Behler, and Christoph Dellago. Library-based lammps implementation of high-dimensional neural network potentials. *J. Chem. Theory Comput.*, 15(3):1827–1840, Jan 2019.

[154] Jian Liu, Richard S. Andino, Christina M. Miller, Xin Chen, David M. Wilkins, Michele Ceriotti, and David E. Manolopoulos. A surface-specific isotope effect in mixtures of light and heavy water. *J. Phys. Chem. C*, 117(6):2944–2951, Jan 2013.

[155] Franz Baumgärtner and Maria-Anna Kim. Isotope effects in the equilibrium and non-equilibrium vaporization of tritiated water and ice. *Appl. Radiat. Isot.*, 41(4):395–399, Jan 1990.

[156] Hilton A. Smith and Karl R. Fitch. Determination of the separation factor for the vaporization of mixtures of protium and tritium oxides. *J. Phys. Chem.*, 67(4):920–921, Apr 1963.

[157] Jochen Hoefs. *Stable isotope geochemistry*, volume 285. Springer, 2009.

[158] Joyita Banerjee, Peter Koronaios, Brittni Morganstein, Steven J. Geib, Robert M. Enick, John A. Keith, Eric J. Beckman, and Sachin S. Velankar. Liquids that freeze when mixed: Cocrystallization and liquid–liquid equilibrium in polyoxacyclobutane–water mixtures. *Macromolecules*, 51(8):3176–3183, Apr 2018.

[159] Hiroyuki Tadokoro, Yasuhiro Takahashi, Yôzô Chatani, and Hideto Kakida. Structural studies of polyethers, $[\text{—}(CH2)_m\text{—O—}]_n$. v. polyoxacyclobutane. *Makromol. Chem.*, 109(1):96–111, Nov 1967.

[160] Yasuhiro Takahashi, Yasunari Osaki, and Hiroyuki Tadokoro. Planar zigzag modification of polyoxacyclobutane (modification iv) and its disordered structure. *J. Polym. Sci., Polym. Phys. Ed.*, 19(7):1153–1155, Jul 1981.

[161] Hideto Kakida, Daisuke Makino, Yozo Chatani, Masamichi Kobayashi, and Hiroyuki Tadokoro. Strutural studies of polyethers $[-(CH_2)_mO-]_n$. viii. polyoxacyclobutane hydrate (modification i). *Macromolecules*, 3(5):569–578, Sep 1970.

[162] E Perez, JG Fatou, and A Bello. Study of the melting process in polyoxetanes. *Eur. polym. J.*, 23(6):469–474, 1987.

[163] E Pérez, A Bello, and JG Fatou. Effect of molecular weight and temperature on the isothermal crystallization of poly (oxetane). *Colloid Polym. Sci.*, 262(8):605–610, 1984.

[164] E Pérez, MA Gomez, A Bello, and JG Fatou. Crystallization behaviour of polyoxetanes: poly (oxetane), poly (3, 3-dimethyloxetane) and poly (3, 3-diethyloxetane). *Colloid Polym. Sci.*, 261(7):571–576, 1983.

[165] Mark A Harmer, David C Confer, Christian K Hoffman, Scott C Jackson, Ann Y Liauw, Aaron R Minter, Edward R Murphy, Rupert E Spence, and Hari B Sunkara. Renewably sourced polytrimethylene ether glycol by superacid catalyzed condensation of 1, 3-propanediol. *Green Chem.*, 12(8):1410–1416, 2010.

[166] Wei J Cui, Kimberley B McAuley, Ralph A Whitney, Rupert E Spence, and Tuyu Xie. Mathematical model of polyether production from 1, 3-propanediol. *Macromol. React. Eng.*, 7(6):237–253, 2013.

[167] So Young Bae, Si Hyun Jeong, and Byung Kyu Kim. Waterborne polyurethane elastomer using renewable polyols. *J. Elastomers Plast.*, 48(1):47–57, 2016.

[168] George A. Kaminski, Richard A. Friesner, Julian Tirado-Rives, and William L. Jorgensen. Evaluation and reparametrization of the opls-aa force field for proteins via comparison with accurate quantum chemical calculations on peptides†. *J. Phys. Chem. B*, 105(28):6474–6487, Jul 2001.

[169] Christian Robl and Armin Weiss. Alkaline-earth squarates iii. cac4o4· 2.5 h2o, a novel polymer complex with zeolitic properties (1). *Materials research bulletin*, 22(3):373–380, 1987.

[170] Shuichi Nosé. A unified formulation of the constant temperature molecular dynamics methods. *J. Chem. Phys.*, 81(1):511, 1984.

[171] Kari Laasonen, Alfredo Pasquarello, Roberto Car, Changyol Lee, and David Vanderbilt. Car-parrinello molecular dynamics with vanderbilt ultrasoft pseudopotentials. *Phys. Rev. B*, 47(16):10142–10153, 1993.

[172] John P. Perdew, J. A. Chevary, S. H. Vosko, Koblar A. Jackson, Mark R. Pederson, D. J. Singh, and Carlos Fiolhais. Atoms, molecules, solids, and surfaces: Applications of the generalized gradient approximation for exchange and correlation. *Phys. Rev. B*, 46(11):6671–6687, 1992.

[173] John P. Perdew, J. A. Chevary, S. H. Vosko, Koblar A. Jackson, Mark R. Pederson, D. J. Singh, and Carlos Fiolhais. Erratum: Atoms, molecules, solids, and surfaces:

Applications of the generalized gradient approximation for exchange and correlation. *Phys. Rev. B*, 48(7):4978–4978, 1993.

[174] Peter Vassilev, Christoph Hartnig, Marc T. M. Koper, Fréderic Fréchard, and Rutger A. van Santen. Ab initio molecular dynamics simulation of liquid water and water-vapor interface. *J. Chem. Phys.*, 115(21):9815, 2001.